METHANATION OF CARBON DIOXIDE OVER NI-BASED CARBON NANOTUBES MONOLITH CATALYSTS

By

QISTINA BINTI OMAR

Thesis Submitted to the School of Graduate Studies, Universiti Putra Malaysia, in Fulfilment of the Requirements for the Degree of Doctor of Philosophy

August 2023

FK 2023 38

DEDICATION

This thesis is dedicated to my lovely family and friends:

To my parents, Cikgu Omar & Che Jamilah for their endless love and support.

To my sons, Qais & Qayyum, who give me strength with all their hugs and love.

To my siblings, Nurhanani, Hafizah, Hakimi, Izzati & Nur Bazla, who have been understanding and encouraging.

To all my friends especially Norulnazilah, Nurul Khamsatul, Norlaily, Nurul Filzah, Siti Rudzhiah, Fadiatul, Aminatul, Noorharliza, Suhaimi and Kareem who have supported me on this journey.

To Haslan, who always gives me unwavering support and encouragement during my most challenging moments, I am deeply grateful for your presence in my life.

With love, respect, and a bunch of memories,
this thesis is only possible because of you.

Abstract of thesis presented to the Senate of Universiti Putra Malaysia in fulfilment of the requirement for the degree of Doctor of Philosophy

METHANATION OF CARBON DIOXIDE OVER NI-BASED CARBON NANOTUBES MONOLITH CATALYSTS

By

QISTINA BINTI OMAR

August 2023

Chair : Assoc. Prof. Ts. Salmiaton Binti Ali, PhD
Faculty : Engineering

Nickel based catalyst has been a potential catalyst in CO_2 methanation. However, the challenges of the existing catalyst including carbon deposition and catalyst stability need to be addressed for more efficient performance of CO_2 methanation. The objective of the study is to synthesize the CNT monolith at optimum condition, to fabricate monometallic and bimetallic supported onto CNT monolith, to investigate the performance of the catalysts in CO_2 methanation reaction at optimum condition and to predict the suitable kinetic and model fitted the catalyst behavior. The experimental studies conducted to grow CNT onto cordierite monolith at optimum condition using direct liquid injection chemical vapor deposition after immersion in Ni/citric acid solution. The CNT monolith catalyst was fabricated via impregnation method and the catalytic CO_2 methanation reaction was performed in a fixed bed reactor at optimum condition. The optimization studies were designed by Taguchi method based on $L_9(3^4)$ orthogonal array and characterization analysis was determined using X-ray diffraction (XRD), field emission scanning electron microscopy (FESEM), transmission electron microscopy (TEM) and others. About 96.45% of CNT's growth onto monolith was sized in the range of 32 to 34 nm. The performance of monometallic CNT monolith catalysts achieved about 77-86% of CO_2 conversion, 76-98% of CH_4 selectivity and 1-23% CO selectivity. Meanwhile, bimetallic CNTs monolith catalyst accomplished above 90% for CO_2 conversion and CH_4 selectivity and less than 10% of CO selectivity. The kinetic behaviour of 10 wt.% Ni CNT and 1/10 wt.% Co/Ni CNT monolith catalyst were fitted based on the Langmuir-Hinshelwood (L-H) models that showed only reactant adsorbed with the dual-site mechanisms and all reactants and products were adsorbed through a single-site mechanism, respectively. As the conclusion, the CNT monolith provides a potential as a catalytic support due to its mesoporous active catalytic site. Furthermore, this study shows that bimetallic CNTs monolith catalyst of 1/10 wt.% Co/Ni gave the highest performance compared to the other catalysts.

Keywords: CO_2 methanation, CNT monolith catalyst, Taguchi methods

SDG 13: Take urgent action to combat climate change and its impacts

Abstrak tesis yang dikemukakan kepada Senat Universiti Putra Malaysia sebagai memenuhi keperluan untuk ijazah Doktor Falsafah

PENGHASILAN GAS METANA DARIPADA KARBON DIOKSIDA MENGGUNAKAN KARBON TIUB NANO DENGAN PEMANGKIN NIKEL

Oleh

QISTINA BINTI OMAR

Ogos 2023

Pengerusi : Prof. Madya Ts. Salmiaton Binti Ali, PhD
Fakulti : Kejuruteraan

Mangkin berasaskan Nikel telah menjadi mangkin berpotensi dalam pemetanan CO_2. Walau bagaimanapun, cabaran mangkin yang sedia ada termasuklah pengendapan karbon dan kestabilan mangkin perlu ditangani untuk prestasi lebih berkesan pemetanan CO_2. Objektif kajian ini ialah untuk mensintesis monolit CNT pada keadaan optimum, untuk bikin mangkin logam tunggal dan dwi logam yang disokong pada monolit CNT, untuk menyiasat prestasi mangkin dalam tindak balas pemetanan CO_2 pada keadaan optimum dan untuk meramalkan kinetik dan model yang sesuai dengan kelakuan mangkin. Kajian dijalankan bagi menumbuhkan CNT pada monolit kordierit pada keadaan optimum dengan menggunakan suntikan cecair bahan kimia langsung selepas rendaman dalam larutan Ni/asid sitrik. Mangkin monolit CNT telah terbikin melalui kaedah pengisitepuan dan tindakbalas pemetanan CO_2 bermangkin telah dilakukan dalam reaktor lapisan tetap pada keadaan optimum. Kajian pengoptimuman telah direka bentuk oleh kaedah Taguchi berdasarkan tatasusunan ortogon $L_9(3^4)$ dan analisis pencirian ditentukan menggunakan pembelauan sinar-X (XRD), mikroskopi elektron pengimbasan pancaran medan (FESEM), mikroskopi elektron penghantaran (TEM) dan lain-lain. Kira-kira 96.45% pertumbuhan CNT pada monolit bersaiz dalam julat 32 hingga 34 nm. Prestasi mangkin monolit logam tunggal mencapai kira-kira 77-86% penukaran CO_2, 76-98% kepilihan CH_4 dan 1-23% kepilihan CO. Sementara itu, mangkin monolit CNT dwi logam telah mencapai lebih daripada 90% untuk penukaran CO_2 dan kepilihan CH_4 dan kurang daripada 10% kepilihan CO. Kelakuan kinetik mangkin monolit 10 %berat Ni CNT dan 1/10 %berat Co/Ni CNT telah dipasang berdasarkan model Langmuir-Hinshelwood (L-H) yang menunjukkan hanya bahan tindak balas terjerap dengan mekanisme tapak-duaan dan kesemua bahan tindak balas dan produk terjerap melalui mekanisme tapak-tunggal, masing-masing. Sebagai kesimpulan, monolit CNT memberikan potensi sebagai sokongan mangkin kerana tapak bermangkin aktif mesoliangnya. Selain itu, kajian ini menunjukkan bahawa

mangkin monolit CNT dwilogam 1/10 %berat Co/Ni telah memberikan prestasi yang tertinggi berbanding mangkin yang lain.

Kata kunci: Pemetanan CO_2, pemangkin CNT monolit, kaedah Taguchi

SDG 13: Mengambil tindakan mendesak untuk memerangi perubahan iklim dan kesan-kesannya

ACKNOWLEDGEMENTS

In the name of Allah, the Most Compassionate, the Most Merciful

All praise and thanks to Almighty Allah. With His blessing, I was able to complete my research and compile this manuscript, for which I am eternally grateful.

I would like to thank everyone who has contributed to this project in anyway, whether directly or indirectly, by giving assistance, thought, ideas, skills, and motivation.

I would like to extend my deepest appreciation to my supervisor Assoc. Prof. Ts Dr Salmiaton Binti Ali for accepting me as a PhD student and guiding me along the way. I am grateful for the opportunity to participate in this project with her valuable support and insightful suggestions when I was discouraged by my failures and challenging issues.

To my Co-supervisor, Professor Ir Dr Thomas Choong Shean Yaw, I would like to express my heartfelt gratitude for his advice, support, and assistance in pursuing my interest in the research.

I would like to thank my Co-supervisor, Professor Datuk ChM Ts Dr Taufiq Yap Yun Hin, for his support and the opportunity to complete this project.

I am also grateful to my Co-supervisor, Assoc. Prof. Ir Dr Shamsul Izhar Bin Siajam for his insightful and encouraging thoughts.

Ultimately, this work would not be completed successfully without the support of the staff and researchers at the Faculty of Engineering. My special thanks go to Encik Mohd Adli and other technical staff at the Faculty of Engineering, especially from the Chemical Engineering and Environment Department, for their efforts in manufacturing and maintaining the test equipment.

This thesis was submitted to the Senate of Universiti Putra Malaysia and has been accepted as fulfilment of the requirement for the degree of Doctor of Philosophy. The members of the Supervisory Committee were as follows:

Salmiaton binti Ali, PhD
Associate Professor Ts.
Faculty of Engineering
Universiti Putra Malaysia
(Chairman)

Thomas Choong Shean Yaw, PhD
Professor Ir.
Faculty of Engineering
Universiti Putra Malaysia
(Member)

Taufiq Yap Yun Hin, PhD
Professor Datuk ChM. Ts.
Faculty of Science
Universiti Putra Malaysia
(Member)

Shamsul Izhar bin Siajam, PhD
Associate Professor Ir.
Faculty of Engineering
Universiti Putra Malaysia
(Member)

ZALILAH MOHD SHARIFF, PhD
Professor and Dean
School of Graduate Studies
Universiti Putra Malaysia

Date:

TABLE OF CONTENTS

LIST OF TABLES

LIST OF FIGURES

LIST OF ABBREVIATIONS

AACVD	aerosol-assisted chemical vapor deposition
ANOVA	analysis of variance
BET	Brunauer-Emmett-Teller
BJH	Barrett-Joyner-Halenda
CCS	Carbon Capture and Storage
CCU	Carbon Capture and Utilisation
CNT	carbon nanotube
CVD	chemical vapor deposition
DLICVD	direct liquid injection chemical vapour deposition
DOE	design of experiment
EDX	energy dispersive X-ray spectroscopy
EISA	evaporation-induced self-assembly
FESEM	field emission scanning electron microscopy
FTIR	Fourier-transform infrared
GHGs	greenhouse gases
ICDD	International Centre for Diffraction Data
IUPAC	International Union of Pure and Applied Chemistry
LCVD	laser-assisted chemical vapor deposition
L-H	Langmuir Hinshelwood
MWCNTs	multiwalled carbon nanotubes
MOFs	Metal organic frameworls
NASA	National Aeronautics and Space Administration
PECVD	Plasma Enhanced CVD
P2G	Power-to-gas

RWGS	Reverse Water Gas Shift
SEM	Scanning electron microscopy
sccm	Standard cubic centimeter per minute
SCR	Selective catalytic reduction
SSA	specific surface area
SWCNTs	Single wall carbon nanotubes
TPD-CO_2	Temperature-programmed desorption
TPR-H_2	Temperature-programmed desorption
TGA	Thermogravimetric Analysis
XRD	X-ray diffraction

CHAPTER 1

INTRODUCTION

1.1 Research background

Rapid anthropogenic emissions of greenhouse gases (GHGs) are causing serious global warming due to the infrared radiation trapped in the planetary atmosphere. The gases enclose the heat like glass in a greenhouse. The GHGs absorb infrared radiation from the earth and emit as radiant energy. In planetary solar system, the sun supplies ultraviolet and visible radiation to the earth which warms the earth's surface and atmosphere. The total energy radiated from the earth's surface must equal the energy absorbed from the sun. This causes the average surface temperature of the earth to be approximately -18 °C, which is unfavorable to humans. Thus, the phenomenon of primary greenhouse effect has maintained the earth's temperature at an acceptable level of 15 °C. The primary GHGs such as carbon dioxide (CO_2), ozone (O_3), methane (CH_4) and water (H_2O) trap the infrared radiation from escaping out of the earth's atmosphere and reradiate it back towards the earth, causing an elevation in the temperature, hence maintaining the average temperature (Tuckett, 2018). This phenomenon, however, occurs in opposition to the secondary greenhouse effect. The earth's surface temperature begins to rise because of secondary GHGs trapped in the atmosphere, which likely contributed to severe environmental issues. The major greenhouse gas, CO_2 level has increased by 25% since 1850 because of various anthropogenic activities such as fossil fuel combustion and land use management (deforestation and agriculture) (Schneider, 1989).

At present, the annual CO_2 concentration data collected by the National Aeronautics and Space Administration (NASA) recorded in November 2022 was 420 parts per million (ppm), which was 2.50 ppm higher than that in November 2021 as, depicted in Figure 1.1. This data is measured at the Mauna Loa Observatory in Hawaii with the average seasonal cycle removed and it shows the highest CO_2 levels in the air in 650,000 years. Consequently, the global average surface temperature recorded an increase of 1.02 °C, with 2016 and 2020 being the warmest years on record. This is a consistently similar construction prepared by the Climatic Research Unit and the National Oceanic and Atmospheric Administration.

The great impact of the phenomenon encompasses changes like sea level rise, ice mass loss in Greenland, Antarctica, the Arctic, and mountain glaciers worldwide and a host of other impacts have been seen from more large wildfires, heat waves and extreme rainfall events. This phenomenon has been statistically proven by NASA with the increase of 4.0 inches in sea level since January 1993. The Arctic ice minimum and ice sheet mass in Antarctica have

both decreased by 12.6 percent per decade since 1979 and 151 billion metric tons per year since 2002 respectively (climate.nasa.gov).

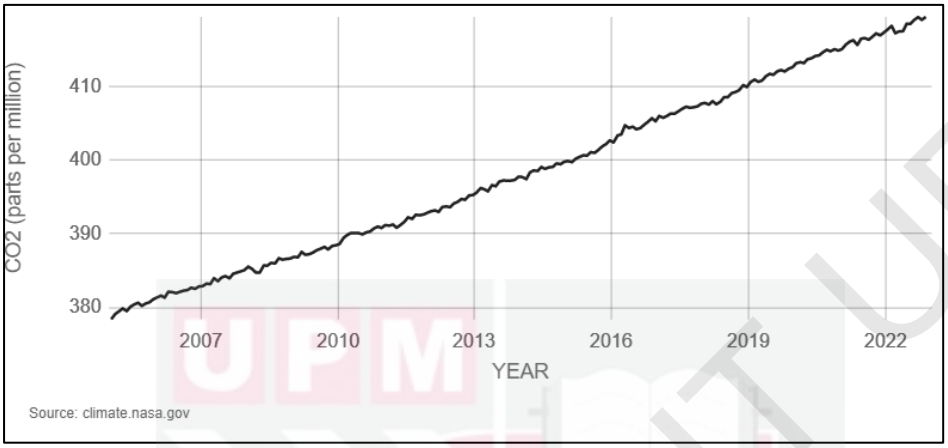

Figure 1.1 : The annual concentration of carbon dioxide (ppm)
(https://climate.nasa.gov/vital-signs/carbon-dioxide)

Numerous efforts are being directed to enhance technological options for reducing CO_2 emissions, which are a major source from the fuel combustion process in power plants. Carbon Capture and Storage (CCS) and Carbon Capture and Utilization (CCU) technologies have been developed in parallel to have an efficient structure for the energy supply chain. CCS plays a crucial role as a standard technology in the global portfolio as a short term solution to attain the reduction of greenhouse gas emissions, whereas the CCU aims to mitigate the effects of CO_2 emissions on global warming by reducing both greenhouse gas emissions and fossil resource depletion (Markewitz et al., 2012). CCS is adopted to capture waste CO_2 produced at stationary sources such as industrial point sources and fossil fuel-based power plants, followed by transport and storage in geological reservoirs or the ocean. However, the geological storage of CO_2 is confronted with the possibility of leakage, long term liability issues, problems with public acceptance of onshore storage locations, and the availability of storage sites. Nevertheless, the application of CCS in the field still leaves a fundamental drawback such as extensive energy consumption for CO_2 desorption, low capture efficiency, and slow sorption kinetics to be addressed. There is a crucial barrier in the implementation of CCS. Therefore, CCU offers an alternative approach strategy (Yang et al., 2012) that includes both industrial capture to obtain concentrated CO_2 and separate functional utilization of CO_2. The industrial capture activity includes scrubbing CO_2 directly from the atmosphere or fossil fueled power plants as CO_2 point sources. On the other hand, the functional utilization of concentrated CO_2 refers to the reuse of CO_2 as a solvent, or the conversion of CO_2 into other products such as fuels (von der Assen et al., 2013).

There are three major approaches being pursued: post-combustion capture, pre-combustion capture, and oxy-fuel process. Among these approaches, post-combustion capture has the potential to provide the most benefits as the existing combustion technologies can still be used without requiring radical changes and is easier to implement as a retrofit option to existing equipment. This promising technology will likely be the first to be implemented, followed by the necessary preparation of flue gas from power plants (Songolzadeh et al., 2012). Flue gases from power plants are a mixture of nitrogen, oxygen, carbon dioxide, SO_2, NO_x and water, plus other contaminants. The removal of NO_x and SO_x from flue gas demonstrates a significant achievement in sustainability and efficiency of the CO_2 capture technology. Moreover, the subtraction of 90% CO_2 from the flue gas results in a 70% depletion of CO_2 emissions to the atmosphere, which consequently reduces the global warming potential by 64% (Singh et al., 2011).

Recently, the transformation of CO_2 into useful chemicals and fuels to reduce the greenhouse effect has garnered a lot of attention. The catalytic methanation of CO_2 process has been developed to establish an efficient process and is quickly becoming the most promising technology for industrial applications. Therefore, it is important to have a good catalyst in the methane conversion process, which accelerates the chemical reactions to produce methane at a fast rate. Various metal catalysts have been intensively studied for the development of catalyst (Takenaka et al., 2004; Zhou et al., 2016), with supported nickel (Ni) catalysts being the most widely chosen due to their high abilities in CO_2 conversion and CH_4 selectivity (Muroyama et al., 2016; Ocampo et al., 2009; Westermann et al., 2015; Zhang et al., 1996). However, most studies reported that these catalysts suffer from several drawbacks, including carbon deactivation, sensitivity to metal site poisoning, sintering, and coke deposition (Nie et al., 2017; Wang et al., 1996).

Consequently, the nanoporous catalysts are an efficient alternative pathway in the reactions because of their unique properties such as highly ordered pore structure, high surface area, and tailored pore size. Number of studies have been proven for the development of highly metal and metal oxides supported catalyst (Muroyama et al., 2016). However, to the best of our knowledge there are no reports relating to the role of metal or metal oxides in methanation of CO_2 using hydrogen in CH_4 selectivity over metal supported on mesoporous carbon coated honeycomb monolith catalysts.

1.2 Problem statement of study

The development of CO_2 methanation catalyst is aimed to achieve a higher CO_2 conversion and CH_4 selectivity. The catalyst is mainly focused on its capability to be active at relatively low temperatures and selective towards methane. The challenges of the catalysts in CO_2 methanation including:

- The high activity of Ni-based catalysts can lead to carbon deposition, which can deactivate the catalyst over time, requiring regeneration or replacement (Tsiotsias et al., 2020).
- The desorption of CO_2 and the formation of carbonate species on the support can be a rate-limiting step, affecting the overall catalytic activity (Mohd Ridzuan et al., 2022).
- The stability of Ni-based catalysts, especially at high temperatures and under varying reaction conditions, is a significant challenge that needs to be addressed for long-term and efficient CO_2 methanation (Al-Fatesh et al., 2023).

Researchers had come up with several attempts to:

- The design of Ni-based catalysts can be optimized and regenerate to reduce carbon deposition, by using bimetallic catalysts, introducing additives, or adjusting the number of alkaline sites on the catalyst (Ren et al., 2023).
- The operating conditions, such as temperature, pressure, and gas composition, can be adjusted to reduce carbon deposition and improve catalyst stability (Zhen et al., 2015).
- The use of a suitable catalyst support, such as carbon nanotubes, can reduce carbon deposition and improve catalyst stability (Lv et al., 2020; Yadav et al., 2023).
- Performing kinetic experiments to measure the reaction rates and determine the kinetic parameters that can provide valuable insights into the reaction mechanism and help develop more efficient and stable catalysts for CO_2 methanation.

Various supports have been investigated in achieving higher catalytic activity of CO_2 methanation including aluminium oxide (Al_2O_3) (Frontera et al., 2017), silicon oxide (SiO_2) (Park & McFarland, 2009), zirconium oxide (ZrO_2) Ren et al. (2015), cerium oxide (CeO_2) Zhou et al. (2016), zeolites, metal-organic frameworks (MOFs) and others. Presently, Ni-based catalysts on supports are most widely explored due to their being cost-effective and highly active. However, Ni catalysts are typically supported on powders, which can create high back pressure and lead to operational inconvenience. Therefore, it is important to investigate an alternative support for making the catalyst more efficient. Carbon nanotube (CNT) monolith catalysts possess a high surface area, high mechanical and thermal strength, better heat transfer, and a low pressure drop that make them suitable for use in the CO_2 methanation reaction. The Ni metal is doped onto a CNT monolith to produce a catalyst with a higher active phase and lower cost. Moreover, the structured catalyst could reduce the carbon deposition that created during the reaction and potentially to be regenerated to be used in catalytic reaction. The kinetic parameters could govern the reaction mechanism and provide information to describe the rate mechanism of the catalyst for CO_2 methanation.

1.3 Objectives of the study

The main objective of this study is to develop a route for CO_2 utilization method using high performance catalyst in a methanation reactor by determining these following objectives:

1. To synthesize CNT monolith using chemical vapor deposition (CVD) at optimum conditions obtained from the design of experiment (DOE) by Taguchi method.

2. To fabricate mono and bimetallic monolith catalyst the CNT monolith via impregnation.

3. To assess the performance of mono and bimetallic CNT monolith catalyst on the CO_2 methanation reaction towards CO_2 conversion and CH_4 selectivity using optimum condition obtained from Taguchi method.

4. To predict the suitable kinetic and model representing the catalyst behavior in the CO_2 methanation reaction.

1.4 Scopes of the research

1. To achieve objective (1), the CNTs monolith was prepared using chemical vapor deposition (CVD) at optimum conditions (4 parameters: mass ratio of Ni to citric acid, injection rate, reaction time in CVD and temperature) via immersion method of Ni that examined by Taguchi method and then characterize the CNT monolith using morphology, structural, chemical, surface, thermal, and crystallinity analyzes.

2. To accomplish objective (2), the mono and bimetallic CNT monolith catalyst is fabricated via impregnation in Ni solution and calcined at 450°C in three hours to produce CNTs monolith catalyst. The morphology, structural, chemical, surface, and thermal properties are analyzed before and after reaction to distinguish the effect of CNTs monolith and CNTs monolith catalyst.

3. To support objective (3), the performances of catalyst were evaluated and analyzed in fixed bed reactor at optimum condition (Ni loading, reaction temperature and flowrate of gas) that designed from Taguchi method for the measurement of CO_2 conversion, CH_4 selectivity, Co selectivity and 210 hours for stability test.

4. To attain objective (4), the kinetic studies was examined by fitting the experimental data into a kinetic model to find the best fit theoretical model that can describe the mechanism of the catalytic reaction process.

1.5 Research contributions

This study contributes to the knowledge on the:

1. Utilization of new nanomaterial supported onto monolith structure to gain high surface area and high strength catalyst.

2. The high metal deposits on metal coated CNT monolith catalysts show better CO_2 methanation performances.

3. The more active phase on the surface of the CNT monolith accomplishes the best catalytic activity for CO_2 conversion and CH_4 selectivity.

4. Kinetics assessment on the catalyst surface in CO_2 methanation reaction.

1.6 Outlines of the thesis

The thesis outlines are described as follows.

Chapter 1: This chapter describes the motivation and overview of the research.

Chapter 2: The big picture of the research background on CO_2 emission and capture is discussed. The existing technologies used, and the applicable approaches of CO_2 conversion are discussed in this chapter. The selection of catalysts used in this research is studied.

Chapter 3: This chapter describes the preparation techniques and synthesis method of CNT monolith and CNT monolith catalyst in detail. The DOE is established using the Taguchi method to provide an optimum condition of synthesis method for CNTs' growth on monolithic supports. Moreover, the optimum condition of CO_2 methanation is applying Taguchi method.

Chapter 4: The Taguchi method analysis of synthesis CNT monolith and the characterization of CNT monolith and CNT monolith catalysts, as well as the significant effect of the catalysts on the catalytic reaction, are fully described in this chapter. Moreover, the Taguchi method analysis for CO_2 methanation is also have been analyzed to get the optimum condition. The stability and reusability study are provided to show the capability of an established catalyst**.**

Chapter 5: The kinetic studies of the catalysts are performed and compared with the model predictions. All the catalysts are characterized in detail to evaluate the behaviors that can affect their catalytic activity.

Chapter 6: The conclusion and recommendations for further studies in the future are listed.

CHAPTER 2

LITERATURE REVIEW

2.1 Introduction

Carbon dioxide concentrations are currently rising drastically and the accumulation of CO_2 in the atmosphere has a significant impact on climate change. Many potential approaches have been identified as a vital strategy for reducing emissions to the atmosphere including the usage of renewable energy sources such as wind, solar and nuclear in the production of electricity. However, the energy sources are an intermittent nature. As a result, the CCS of CO_2 has emerged as an alternative option to prevent emissions from entering the atmosphere. The captured CO_2 is transported via pipeline and stored underground and in ocean storage (Boot-Handford et al., 2014; Szulczewski et al., 2012). The storage system converts CO_2 energy into renewable energy that is integrated with the existing power grid; however, due to heat losses of about 20% for the entire system, and only a maximum efficiency of approximately 63.6% can be achieved. Nevertheless, this approach is severely limited in terms of storage capacity, charge and discharge periods, and safety and efficacy are still in doubt due to a potential leakage problem (Schaaf et al., 2014).

Therefore, the carbon capture and utilization (CCU) via recycling and converting the CO_2 into a useful carbon feedstock for the synthesis of fuels and chemicals are great solution to reduce the emission and valuable to chemical production. This could create a high economic value as CO_2 is abundant, renewable, and safe carbon source. Many researchers are interested in applying the green technology concept in converting CO_2 into high value-added products due to high demand. However, due to the thermodynamic and chemical stability of CO_2 molecules as a single reactant, the conversion of CO_2 into other high value-added products requires a significant amount of energy. Thus, the presence of other substances, such as hydrogen gas (H_2), with a higher Gibbs free energy will facilitate the thermodynamic process.

Various approaches can be utilized in the CO_2 conversion process including catalytic conversion (Ahmad et al., 2017; Aziz et al., 2014; Yuanyuan Liu et al., 2013; Toyir et al., 2001), electrochemical conversion (Ogura, 2013; Ross et al., 2019), enzymatic conversion (Long et al., 2017; Shi et al., 2015), plasma conversion (Krawczyk et al., 2014; Sentek et al., 2010), and bioconversion (T.-T. Zhao et al., 2019). CO_2 is predominantly converted into C_1 compounds (methane, methanol, formic acid, etc.), C_2 compounds (ethane, acetic acid, ethanol, formate, etc.), organic carbonates, salicylic acid, and other chemical products. Among the valuable carbon compounds, methane has received significant attention as a useful fuel that also serves as a hydrogen carrier and a power to gas system (P2G). CO_2 methanation is a beneficial method since it

is faster and simpler than other reactions that create hydrocarbon or alcohol (Wang et al., 2016) and can be directly injected into existing natural pipelines while being conducted at low temperature and atmosphere pressure.

2.2 CO_2 methanation

CO_2 methanation is an exothermic and thermodynamically favourable reaction, as it is considerably faster than other hydrogenation reaction information of hydrocarbons and alcohols. This reaction is discovered by Sabatier and Senderens in 1902 known as the Sabatier reaction, and it could be implemented industrially as the hydrogen feedstock could be generated from renewable sources. Theoretically, CO_2 methanation can achieve high CO_2 conversion and high catalytic selectivity for methane under mild reaction conditions with lower energy consumption. In the reduction of CO_2 (+4) to CH_4 (-4), eight electrons with a high kinetic energy barrier are required. Steps leading to the methanation of CO_2 include chemisorption of CO_2, dissociation of CO_2 into CO and O adsorbed on the surface, and the reaction of the dissociated species with hydrogen to form CH_4. The primary focus of CO_2 methanation is the direct mechanism of the reaction that produces CH_4 and water (Equation 2.1).

$$CO_2 + 4H_2 \leftrightarrow CH_4 + 2H_2O \qquad \Delta H = -165kJ/mol \qquad (2.1)$$

Due to Le Chatelier principle, the equilibrium of a chemical reaction responds to change in temperature, pressure, or concentrations reactant. The manipulation of these factor influences the direction of the equilibrium position as product or reactant favours. The direct CO_2 methanation is exothermic reaction and the heat release is considered as a product. At high temperature, the heat increases on the right side and disturb the equilibrium. Therefore, an efficient heat removal is required to drive the equilibrium toward the product side in achieving high CH_4 production. Moreover, this could ensure the CO_2 conversion occurs without limitation and prevent the deactivation of the catalyst from sintering effects. An inefficient heat removal can cause high selectivity for CO but low selectivity for CH_4 due to the endothermic nature of reverse water-gas shift (RWGS). Initially, carbon dioxide and hydrogen are converted to carbon monoxide and water in Equation 2.2. Then, the reaction proceeds with the reaction of carbon monoxide and hydrogen in Equation 2.3 (Stangeland et al., 2017). Carbon monoxide is considered as a byproduct of the intermediate reaction of methanation.

$$CO_2 + H_2 + heat \leftrightarrow CO + H_2O \qquad \Delta H = 41kJ/mol \qquad (2.2)$$

$$CO + 3H_2 \leftrightarrow CH_4 + H_2O + heat \qquad \Delta H = -206kJ/mol \qquad (2.3)$$

The most stable saturated hydrocarbon (C_2), ethane, can also be formed in Equation 2.4 and it can be eliminated by a catalyst with a high performance.

$$CO_2 + 3.5H_2 \leftrightarrow 0.5C_2H_6 + 2H_2O + heat \qquad \Delta H = -132kJ/mol \tag{2.4}$$

There is also the possibility, under certain conditions, of a reaction leading to the deposition of solid carbon according to the reaction mechanism in Equation (2.5). This carbon deposition may render the active sites of a metal catalyst inactive.

$$CO_2 + 2H_2 \rightarrow C + 2H_2O \qquad \Delta H = -132kJ/mol \tag{2.5}$$

The kinetic limitations of the Sabatier reaction are affected by temperature, pressure, the presence or absence of promoters, and the influence of the catalyst during the methanation process. According to Lechkar et al. (2018), Xu et al. (2018) and Wang et al. (2016), the significant kinetic limitation in the reaction necessitates an efficient catalyst to achieve an acceptable rate and selectivity for CH_4, particularly at low temperature. Thus, many heterogeneous catalysts have been reported to be effective, and carbon materials have been regarded as the most promising adsorbents for CO_2 capture.

2.3 Overview of CO_2 methanation

The efficiency of CO_2 methanation is highly dependent on catalytic performance. A lot of studies have been conducted on both homogeneous and heterogeneous catalysts for CO_2 methanation. The homogeneous catalysts exhibit suitable activity and selectivity but are complicated to regenerate. While, the heterogeneous catalysts are preferred due to their stability, separation, ease of handling, and reusability (Abelló et al., 2013; Centi & Perathoner, 2009).

The investigation of CO_2 methanation showed an excellent performance in presence of catalyst including Ni, Fe, Co, and others which attached to the various metal oxide (Al_2O_3, SiO_2, MgO, CeO_2, ZrO_2 and TiO_2) and porous material supports (metal-organic frameworks (MOFs), zeolites, carbon nanotubes, carbon nanofibers, MCM-41, and SBA-15) as listed in Table 2.1 and Table 2.2. Due to highly exothermic nature of the CO_2 methanation, the reaction is favored at low temperatures as mostly reports conducted at 150 - 450 °C with the ratio of H_2/CO_2 at 4:1. The Ni catalyst is proven an excellent catalyst as both CO_2 conversion and CH_4 selectivity are reached >98% (Bukhari et al., 2019; Guo et al., 2018). Moreover, the active phase on the support prepared by the catalyst deposition method like wet impregnation, co-precipitation, co-decomposition, and reverse micro emulsion are responsible to

activate the CO_2 and H_2 gas in the reaction, increase the surface chemistry for the reaction to occurs and perform in the catalytic conversion of CO_2 to CH_4.

2.4 Catalysts used in CO_2 methanation reaction

Recent developments in CO_2 methanation focussing the role of catalysts to improve the efficiency and stability of catalysts (Tan et al., 2022). In addition, the oxidation state of the surface plays an important role in the CO_2 methanation. The catalytic performance is sensitive to the degree of surface reduction, such that an overly reduced or overly oxidised surface will decrease the activity. Upham et al. (2015) discovered the oxidised surface to CO_2 and then H_2 inhibits the formation of CH_4 while exposing a reduced surface to CO_2 and then H_2 successfully produces CH_4. The results showed that the CH_4 is produced by the reaction of hydrogen with the surface species associated with a variety of surface carbonates. Thus, the CH_4 is not formed through CO or a formate intermediate.

Over the past years, the selection of active metals from transition metals and noble metals have been employed in CO_2 methanation as catalysts. Catalysts such as Ni, Fe, Co, Ru, and Rh have been identified as the most effective for reactions conducted under mild conditions. Among noble metals, Ru is the most precious metal catalyst that boasts an outstanding performance as it is more active and selective towards methanation. The Ru metal shows less carbon deposition due to its high sulphur resistance, resulting in less deactivation of catalyst (Frontera et al., 2017; Ghaib & Ben-Fares, 2018; Porta et al., 2020). Moioli and Züttel (2020) stated that the Ru-based catalysts performed at about 100°C lower than commercial $Ni/Mg/Al_2O_3$ and 10-20°C lower than Ni/Al_2O_3. Moreover, a small amount of Ru-based catalyst applied to the reaction results in an excellent CH_4 yield without CO coproduction at 573 K compared to a Ni-based catalyst (Garbarino et al., 2015). However, the implementation of these Ru-based catalysts in an industrial setting is limited due to their high cost, making them only suitable for small scale applications.

As a result, numerous researchers have conducted extensive research on the development of highly active Ni catalysts for industrial applications. Ni-based catalysts were selected due to their affordability and accessibility. A lot of researchers focused on the laboratory scale of the CO_2 methanation reaction due to its theoretical importance and potential practical applications. The performance of Ni-based catalysts towards CO_2 methanation depends on various parameters, such as the type of support, the amount of Ni loading, the presence of a second metal, and the preparation method (Aziz, Jalil, Triwahyono, & Ahmad, 2015). Zhou et al. (2016) discussed the Ni/CeO_2 in the CO_2 methanation reaction. The catalyst reduced at temperatures higher than 380°C for two hours and exhibited the highest conversion of CO_2 and CH_4 selectivity at 340°C for more than ten hours of reaction progress.

Even though the Ni-based catalyst is the best option for CO_2 methanation, it has a few drawbacks including insufficient low temperature activity, low dispersion, and reducibility, as well as nanoparticle sintering. Thus, the researchers have introduced a bimetallic catalyst via the combination of a Ni-based catalyst with a second transition metal (e.g., Fe and Co) or a noble metal (e.g., Ru, Rh, Pt, Pd, and Re) to overcome the drawbacks and enhance the catalytic activity in CO_2 methanation. Indeed, the development of a Ni-M-based catalyst (where M = Fe, Co, Cu, Ru, Rh, Pt, Pd, and Re) could result in a promising low cost methanation catalyst. Based on the results with the other five criteria (H_2/CO_x, space velocity, process temperature, gas feed rate, and catalyst stability), consideration of CH_4 as the response indicator revealed that Ru-based catalysts were the most preferable based on technical and economic performance factors, while Co-based catalysts were the least efficient. In addition, Kuznecova and Gusca (2017) found that Fe and Ni catalysts were superior to Co, Mo, and Ru catalysts in terms of selectivity, activity, stability, and cost. However, as Fe has a relatively low level of selectivity, Ni could become the preferred option.

Table 2.1 : Overview of several reports on the investigation of catalytic methanation

Catalyst	Deposition method	Reactor	Reactor Conditions	A: CO_2 conversion B: CH_4 selectivity	References
amorphous Co–$Zr_{0.1}$–B–O (Promoter: Zr)	coprecipitation method	stainless-steel autoclave, high-pressure fixed bed	180°C 10.7 mmolCO_2 $gcat^{-1}$ h^{-1}	A: - B: 97.8%	(Tu et al., 2021)
$Fe_{30}Ni_{70}$@Ni NPs	co-decomposition	Fixed bed glass reactor	410 °C H_2/CO_2: 4/1 WHSV: 49 Lh^{-1} $g(Fe+Ni)^{-1}$ Flow rate (H_2/N_2): 25 ml/min $m_{catalyst}$: 400 mg	A: 71% B: 65%	(De Masi et al., 2020)
Ni-Co/CeO_2-ZrO_2 (Promoter: Co and Mn)	wet impregnation	vertical continuous fixed-bed quartz reactor	200 °C–450 °C H_2/CO_2: 4/1 WHSV: 12,000 $mLg^{-1}h^{-1}$ Flow rate (H_2/N_2): 100 ml/min $m_{catalyst}$: 0.25 g	A: 77% (300°C) B: 97% (300°C)	Pastor-Pérez et al. (2020)
Ni-Co/SiO_2 (Promoter: Fe, Co and Zn)	wet impregnation	a tubular quartz reactor	200–400 ◦C $CO_2/H_2/N_2$: 1/4/15 flow rate (H_2/N_2): 100 ml/min $m_{catalyst}$: 0.10 g	A: 73 % (350°C) B: 98.5 % (350°C)	(Dias & Perez-Lopez, 2021)

Table 2.1: **Continued**

Catalyst	Deposition method	Reactor	Reactor Conditions	A: CO_2 conversion B: CH_4 selectivity	References
10 wt.% Ni/F-SBA-15 (1,3.10, 15 wt %)	incipient wetness impregnation (IWI)	fixed-bed reactor	400°C H_2/CO_2 = 4/1 GHSV: 24,900 $mLg^{-1}h^{-1}$ $m_{catalyst}$: 0.20 g	A: 99.7% B: 98.2%	Bukhari et al. (2019)
10 wt.% Ni-ZSM-5, 10 wt.% Ni-SBA-15, 10 wt.% Ni-MCM-41, 10 wt. % Ni-Al_2O_3 10 wt.% Ni-SiO_2	incipient wetness impregnation (IWI)	fixed bed quartz	200-450°C H_2/CO_2=4:1 GHSV: 2400 h^{-1} Flowrate: 40 ml/min 1 ml packed (20-40 mesh)	A: 99% B: 99%	Guo et al. (2018)
11 wt.% Ni/MgO 17 wt.% Ni/MgO	wet impregnation	fixed-bed tubular	352°C 1 atm $H_2:CO_2:N_2$ = 4:1:5 Flowrate: 250 cm^3 $_{STP}$/min	A:70% B:>99%	Baldauf-Sommerbauer et al. (2018)
10 wt.% Ni/Al_2O_3	homogeneous deposition-precipitation	fixed bed	200-450 ◦C 1 atm H_2/CO_2 = 4:1 Flowrate: 600 ml/min GHSV: 26,700 h^{-1} WHSV: 12,000 $mL_{CO2}/g_{cat}.h$ $m_{catalyst}$: 0.15 g	A:69% (400°C) B:95% (400°C)	Mutz et al. (2017)

Table 2.1: Continued

Catalyst	Deposition method	Reactor	Reactor Conditions	A: CO_2 conversion B: CH_4 selectivity	References
5% Ru/TiO_2-Al_2O_3	wet impregnation method	Fixed bed	150-400°C Flowrate: 50 ml/min $CO_2/H_2/N_2$: 18/72/10 (v%)	A: ±85%	Xu et al. (2016)
Ni/CeO_2	Excess impregnation method	Fixed-bed quartz (6mm)	260, 300, 340 ◦C 1 atm H_2/CO_2/Ar: 46:10:44 (v%) Flowrate: 36.67 ml/min WHSV: 22,000 $mLg^{-1}h^{-1}$ $m_{catalyst}$: 0.10 g	A:91.1% (340°C) B: 100%	Zhou et al. (2016)
Ni-Al hydrotalcite catalysts	co-precipitation method	quartz reactor containing the catalyst bed	250- 400 °C 1.013 bar $H_2/CO_2/N_2$: 10:2.5:87.5 (v%) Flowrate: 200 Nml/min GHSV: 20,000 h^{-1} $m_{catalyst}$: 0.60 g	A: 86% (300°C)	Abate et al. (2016)

Table 2.1: Continued

Catalyst	Deposition method	Reactor	Reactor Conditions	A: CO_2 conversion B: CH_4 selectivity	References
Ni/ZrO_2-M (M denoted as 2nd metal)	co-impregnation	stainless-steel, high-pressure fixed bed	190-330°C 0.5MPa H_2/CO_2: 80:20 (v%) Flowrate: 83 ml/min GHSV: 10,000 h^{-1} $m_{catalyst}$: 0.10 g	A: 10% B: 80%	Ren et al. (2015)
$CeO_2/Ni/\gamma\text{-}Al_2O_3$	ultrasonic incipient impregnation	fixed bed (i.d.= 5 mm)	250-400 °C 0.1MPa H_2/CO_2 = 4:1 GHSV: 7,000 h^{-1} $m_{catalyst}$: 0.10 g	A: 32.11 to 72.57%	Zhou et al. (2015)
$Ru/Mn/Ce/Al_2O_3$	incipient wetness impregnation	fixed micro reactor	200°C 1 atm Flowrate: 100 ml/min WHSV: 636 $mLg^{-1}h^{-1}$	A:97.73% (200°C) B:91.31% (200°C)	(Toemen et al., 2014)
6.2%Pd-Mg/SiO_2	reverse micro-emulsion (ME)	Fixed bed	450°C 0.5MPa H_2/CO_2 = 4:1 Flowrate: 10.2 cm^3/min + Ar:2 cm^3/min $m_{catalyst}$: 0.10 g	A: 59% B: 95%	(Park & McFarland, 2009)

2.5 Support of catalyst

The support of catalysts also plays an important role in the methanation reaction mechanism as the support could have an important structural effect on the dispersion and stabilization of the nanoparticles (Baraj et al., 2016; Kim, 2016). Hence, the development of catalysts for CO_2 hydrogenation to CH_4 has been extensively studied on different metal-based catalytic systems in search for high selectivity and low temperature operation. Various supports are explored in the form of powder, metal oxide, pellets and porous materials like foam, carbon, and fiber. Table 2.2 tabulated the overview of carbon support including CNTs, activated carbon and graphene performed in CO_2 methanation.

Moreover, less is known about the catalyst supported on a monolithic structure that can contribute to the higher surface area of catalyst in CO_2 methanation. The conventional packed bed reactor faces difficulties such as pressure drop, intra-particle diffusion limitation, flow channelling, and heat transfer limitation in running the catalytic solid-gas reactions. Therefore, the development of a structured catalyst could be the best solution to overcome the shortcomings of the existing catalyst. Moreover, monolithic structures composed of ceramic or metallic materials are essential in catalytic reactions (Zamaniyan et al., 2010). The better features of monolithic structures provide a uniform flow distribution, low pressure drop and improved mass transfer (Boger et al., 2004; Roy et al., 2004).

The characteristics of a monolith are geometrically defined as cells per square inch (cpsi), which are determined collectively by the number of channels, diameter (d), void fraction (ε), large geometric surface area, high dust tolerance, and large contact area between the structure and reactants (Baharudin & Watson, 2018; Vergunst et al., 2002; Zamaniyan et al., 2010). Generally, the monolith cpsi is in the range of 100-1200, while ε and wall thickness vary from 0.5 to 0.9 and 0.006 to 0.05 cm respectively (Baharudin & Watson, 2018; Roy et al., 2004). The typical monolith is composed of synthetic cordierite with a ratio of $2MgO$, $2Al_2O_3$, $5SiO_2$ and a small portion of other elements. The ceramic monolith element with 25-1600 cpsi cell densities creates an effective catalyst with a large geometrical surface area. Small particles can easily travel through the channels of open structure catalysts, preventing foul and causing minimal pressure loss in the gas stream (Guillén Hurtado et al., 2012; Nijhuis et al., 2001).

Table 2.2 : The overview of carbon-coated catalysts

Carbon types	Catalyst/Promoter	Stability	A: CO_2 conversion B: CH_4 selectivity C: CH_4 yield	References
Carbon nanotubes (CNTs)				
	Ni/Mn	140 hrs	A: 71.6% B: 100%	(Li et al., 2018)
	Ni/Zr-COI (co-impregnation) Ni/Zr-SEQ (sequential impregnation)	50 hrs	B (COI): 100% (225°C) 16% (500°C) B (SEQ): 100% (450°C) 79% (500°C)	(Romero-Sáez et al., 2018)
	Ni/N	~7 hrs	A: 92% B: 98%	(W. Wang et al., 2018)
	Ni/Ce	100 hrs	A: 83.8% B:100%	(Wang et al., 2016)
	Ni (CNTs from ethanol)	~7 hrs	A: ~60% B: ~50%	(Feng et al., 2015)
	Ni/Ca	~7 hrs	C: 85%	(Hu et al., 2014)
Activated carbon (AC)				
	Ni Ni/Ce	100 hrs	A (Ni) : 60.1% (450°C) B (Ni) : >90% (450°C) A (Ni/Ce): 75.2% (350°C) 78.7% (350°C) B (Ni/Ce): 100% (350°C) 100% (400°C)	(Hu et al., 2019)

Table 2.2: Continued

Carbon types	Catalyst/Promoter	Stability	A: CO_2 conversion B: CH_4 selectivity C: CH_4 yield	References
Graphene				
	Ni (Graphene Aerogel)	80 hrs	A (GA): 80.4% (350°C) B (GA): 94.8% (350°C)	(Hu et al., 2021)
	Ni (Graphene Oxide)		A (GO): 68.3% (350°C) B (GO): 93.5% (350°C)	
	Ni	n.a	A: 55.3% (240°C) B: ~100% (240°C)	(Mohd Ridzuan et al., 2020)
	MoS_2	n.a	A: >50% B: >95%	(Primo et al., 2019)
	Ni (rGO)	100 hrs	A (Ni): 78.4% (350°C) B (Ni): 100 % (350°C)	(Hu et al., 2019)
	Ni/Ce (rGO)		A (Ni/Ce): 84.5% (350°C) B (Ni/Ce): 100% (350°C) C (Ni/Ce): 82.3% (350°C)	
	N-doped, defective graphene	20 hrs	A (Ni): 52.3% (500°C) B (Ni): 99.2 % (500°C)	(Jurca et al., 2019)
	Ni	130 hrs	A: 80% (350°C) B: 100% (350°C)	(Fukuhara et al., 2017)

Despite the advantages of monolithic structures, the monolithic catalyst still has its limitations in the sense of less temperature control, lower loading of the active phase, and the costly and complicated nature of manufacturing the monolithic catalysts (Groppi & Tronconi, 2005; Zamaniyan et al., 2010). Furthermore, the low porosity and surface area properties make the cordierite monolith non-ideal for catalytic processes. Hence, researchers have put some efforts in order to improve porosity by varying the precursor composition and acid treatment to increase surface areas. The acid treatment has resulted in the formation of amorphous silica on the surface and a reduction in the material's mechanical strength and thermal stability (Mai et al., 2015). Recently, some researchers improved the surface of a monolith structure by employing carbon that was supported onto the monolith in many parallel channels with varying channel forms in the cross section of the monolith.

Carbon is non-reactive and can be used in a variety of porosities to increase surface area and improve metal catalyst dispersion on the support surface. Carbon coated monoliths have been created to improve thermal and mechanical qualities where the adhesion of the thin layer coating on monoliths is a determining factor in the performance of the entire process and reduce internal mass diffusion. Due to their large accessible surface area per total weight (or volume) of the monoliths, integrated monoliths are most typically used in gas-phase processes rather than liquid phase applications (Hosseini et al., 2020; Moreno-Castilla & Pérez-Cadenas, 2010). The application of a catalyst with a honeycomb structure could result in a more homogeneous gaseous flow than a powder catalyst and better contact between the reactant and catalyst surface, thereby accelerating the overall reaction rate. Sollier et al. (2018) reported that the catalytic behaviour was greatly increased by the reaction with catalytic layer enrichment with Mg and Si, coming from the cordierite structure.

2.6 Carbon nanotubes

There are many outstanding features of carbon, such as low cost, excellent thermal and chemical stability, high surface area, ease of design for pore structure modification, surface functionalization, facile preparation, and low energy consumption for regeneration. Therefore, porous carbons play a significant role in CO_2 adsorption due to their porosity, high stability, excellent availability, and tunable surface chemistry. Graphitic porous carbon is mainly categorised into three pore sizes: micropores (<2 nm), mesopores (2-50 nm), and macroporous (>50 nm). The porous carbon structure commonly takes the form of powders, granules, pellets, fibers, tubes, aerogels, and monoliths.

The discovery of carbon nanotubes CNTs have been the focus of numerous research papers for applications in the future since they were introduced by Iijima (1991). CNTs are a member of the fullerene structural family made up of rolled up graphene sheets with sp_2 hybridization carbon atoms in cylindrical

tubes. The atomic arrangement of carbon atoms making up the nanotube (chirality) exhibits the electronic properties such as being metallic and semiconducting in nature as shown in Figure 2.1. Moreover, the presence of CNTs has been widely used in several applications including conductive films, solar cells, fuel cells, supercapacitors, transistors, memories, displays, separation membranes and filters, purification systems, sensors, and clothing. The applications typically depend on the structure of CNTs such as the number of walls, diameter, length, and chiral angle which impart specific properties (Purohit et al., 2014).

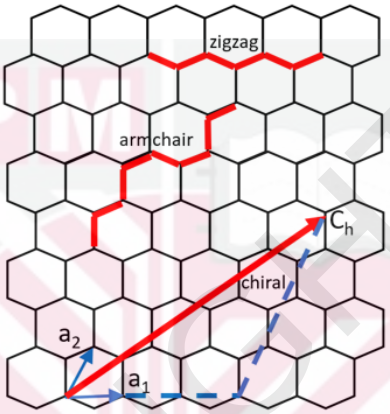

Figure 2.1: Schematic of how graphene can be rolled into various chirality of CNT

The two main basic structures of CNTs are single-walled carbon nanotubes (SWCNTs) and multi-walled carbon nanotubes (MWCNTs). The single-walled carbon nanotubes are made of a single cylinder of graphite sheet held together by van der Waals bonds, while the multi-walled carbon nanotubes are composed of two or more different co-axial tubes or cylinders made of graphene sheets. The SEM image of SWCNTs can be used to describe the type of CNTs, smaller diameter, and highly warped bundle tubes. In the honeycomb crystal lattice of graphite, the wrapped graphene layer is represented by the chiral vector $C_h = n_{a1} + m_{a2}$, with denoted integers m and n as the unit vectors along two directions. Thus, m = 0 is represented by zigzag nanotubes, n = m is represented by armchair nanotubes, and they are chiral nanotubes. The uniqueness of this structure is that it creates different band gaps that indicate the electrical properties of SWCNTs (Neupane, 2014). The other properties of SWCNTs are determined by the diameter and length of the tubes, the atomic arrangement available during the rolling, and the presence of defects.

As compared to SWCNTs, the MWCNTs are larger CNTs that consist of many single-walled tubes stacked one inside the other. The morphology and properties of MWCNTs are quite similar to those of SWCNTs, but their resistance to chemicals is significantly improved. The MWCNTs have their uses, but for semiconducting applications are cheaper to produce, much cheaper compared to SWCNT. Therefore, they can be profitably used to make polymers or other composites, enhancing their mechanical, thermal, and electrical properties. The MWCNTs have shown less of large curve diameter tubes.

The mechanism of catalytic growth of CNTs through microstructural analysis is based on the first law of thermodynamics. This mechanism also explains the relationship between the size of catalyst particles and the initiation of CNT growth. Hydrocarbon vapour initiates contact with the hot metal nanoparticles on the substrate to decompose into carbon and hydrogen species. The hydrogen then dissipates, while the carbon dissolves into the metal. At a certain temperature, the carbon solubility limits in the metal cause as-dissolved carbon to precipitate and crystallise in the form of a cylinder network. The precise thermal gradient inside the metal particles keeps the process going, as hydrocarbon decomposition is an exothermic process that releases heat to the metal's exposed surface and carbon crystallisation is an endothermic process that absorbs heat from the metal's precipitation (Kumar & Ando, 2010).

The CNTs can grow by two primary mechanism which are tip-growth and root-growth. The tip growth model, as depicted in Figure 2.2 (a) occurs when the carbon filament growth in-situ on the surfaces of the metal particles acted as catalyst. The carbon diffused down through the metal and CNTs precipitated out across the metal bottom, thus forcing the metal away from the substrate. The process continuously proceeds if the metal surface allows the carbon to diffuse, making the CNTs grow longer. The catalyst particle deactivated once the surface is covered by excess carbon, the growth of CNTs is stopped growing (Kumar & Ando, 2011; Weissker et al., 2010). The root-growth model (Figure 2.2 (b)) have similar pathways in the tip-growth model but in this case the CNTs fail to push the metal particle up, and thus the CNTs grow up with the catalyst particle rooted on their base. The possible factors that may determine the mode of CNTs' growth are metal support interactions. A weak catalyst substrate interaction results in easier lift up, leading to the tip-growth model, whereas a strong interaction may lead to the root-growth model.

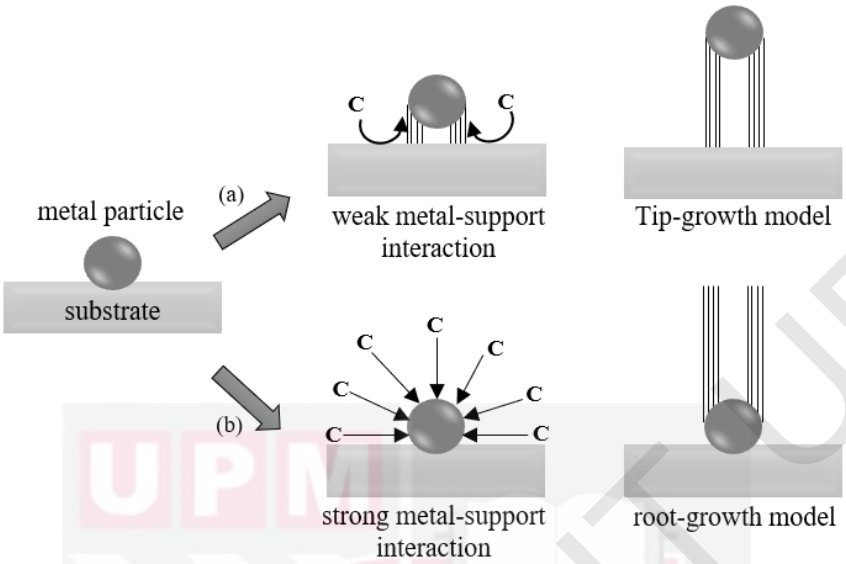

Figure 2.2 : Schematic of (a) tip-growth model and (b) root-growth model

2.7 Synthesis of CNTs

Due to their unique and excellent properties, CNTs have gained popularity in many industrial applications. Large scale production of CNT is crucial and beneficial for cost efficiency as the process can be achieved by low temperature synthesis and less material consumption. In this way, the manufacturing of CNTs could have a positive effect to the environment.

In general, CNTs can be produced by the arc discharge method, laser ablation, plasma torch, hydrothermal, and chemical vapour deposition (CVD). The most popular and widely used technique in synthesizing CNTs is CVD due to its low setup cost, high production yield, high quality, energy efficiency, and ease of scaling up (Baddour & Briens, 2005; Mohamed et al., 2010; Ward et al., 2003). The CVD method is simple and economic due to its performance at low temperature and ambient pressure. Among others, CVD could be the best technique to resolve several issues in the synthesis of CNTs such as, mass production to develop a low cost and large-scale process for synthesizing high-quality nanotubes, selective production to control the structure and its properties, organisation to control the location and orientation of produced nanotubes on a substrate, and mechanisms for nanotube growth. Moreover, the CVD could control the structure or architecture of the CNTs and be versatile in any state (solid, liquid, or gas) of a hydrocarbon. The CVD enables the use of various substrates and allows the growth of CNTs in a variety of forms, such as powder, thin or thick film, aligned and entangled, straight, or coiled nanotubes, and so on. This method also provides greater control over the growth parameters.

2.7.1 Chemical vapor deposition (CVD)

There are several approaches to apply CVD method for CNTs synthesis, including thermal CVD (Baddour et al., 2009; Lee et al., 2002), laser-assisted CVD (LCVD) (Bondi et al., 2006; Park et al., 2009), plasma-enhanced CVD (PECVD) (Jašek et al., 2010; Zhu et al., 2007), aerosol-assisted CVD (AACVD) (Mierczynski et al., 2020; Sagu et al., 2016), and direct liquid injection CVD (DLICVD) (G. L. Esquenazi et al., 2018; Kumar & Yadav, 2019). These methods are distinguished by the energy source used for the decomposition of carbon sources and catalyst particles provided.

The thermal CVD requires a higher temperature to provide the energy for the gas heating process by using a hot filament or hot wall to decompose the gas, which results in the formation of a thin film on the substrate (Dahmen, 2003). The LCVD has replaced the global heat source of the furnace with a localised spot heated by a laser, such as a pyrolytic or photolytic laser. The laser is responsible for the dissociation of the reagent molecules and the deposition process. However, the area of the deposition growth can be limited to that where the laser beam passes (Bondi et al., 2006). The PECVD applies plasma generated from electrical energy and activates the reaction by transferring the energy of its species to the precursors, inducing free radical formation followed by radical polymerization. This technique is applicable to the vapour deposition process for various precursors, including reactive organic, inorganic, and inert materials (Vasudev et al., 2013).

The AACVD and DLICVD are liquid phase variations of the CVD method. In the AACVD process, the aerosol precursor solution is transported into the reaction chamber by using a carrier gas and decomposes onto the substrate as the solvent is evaporated (Marchand et al., 2013). In addition, the DLICVD uses liquid precursors as it is much easier to precisely regulate the flow rate of a liquid than of powders. The DLICVD system makes it possible to apply the vaporization unit to vaporize the liquid precursor, which then decomposes on the substrate in the reaction chamber. In other systems, the precursor is directly injected into the chamber, and the precursors reach the substrate as liquid droplets and are vapourised. As compared to other methods, the DLICVD techniques have proven to be one of the most versatile CVD processes to meet industrial requirements due to their ability to use solid or liquid precursors (Astié et al., 2019).

MWCNTs growth by CVD have low crystallinity when compared to other methods, but SWCNTs grown by CVD method have similar crystallinity to those grown by arc or laser technique. However, this is not a major issue because CVD is superior at synthesizing high yields and purity of CNTs. This method is also viable for structural control or growth parameter control.

2.7.2 CNT growth parameters

The synthesis of CNTs, either SWCNTs or MWCNTs, depends on many parameters. The main parameters involved in the synthesis via CVD method are the carbon source, catalyst, reaction conditions like precursor gas flow rate, process time, and reaction temperature. The implementation of this parameter can control the growth of CNTs that can be distinguished by the structure and chirality of the CNTs.

Carbon sources

The carbon feedstock or carbon source is essential in the synthesis of CNTs via the CVD method. The carbon sources can be in the form of solids, liquids, or gases. The solid hydrocarbon can be stored together in a quartz boat and placed in a tubular reactor. While the liquid carbon source is necessary to become steam in the preheating process before entering the tubular reactor, it is assisted by the carrier gas. As it reacts on the catalyst, the gaseous carbon source can be directly decomposed. Most unsaturated hydrocarbons result in a high yield deposition rate as compared to saturated hydrocarbons (Awasthi et al., 2005). The saturated hydrocarbon is favoured in the production of SWCNTs because it can synthesise the graphitized filaments with fewer walls compared to the unsaturated hydrocarbon. These carbon precursors also affect the types of CNTs that are formed, like bamboo, sheets, yarns, tapes, and others.

A variety of carbon sources are used in CNT growth such as methane, ethylene, acetylene, benzene, xylene, carbon monoxide, acetonitrile, ethanol, toluene, pyridine, and furfuryl alcohol. The linear hydrocarbon source such as methane, ethylene, or acetylene generally decomposes into linear dimers of carbon at high temperatures and can produce straight CNTs. Besides, two cyclic hydrocarbons such as toluene, fullerene and cyclohexane can produce curved CNTs. According to Li et al. (2004), high molecular weight hydrocarbons play a crucial role in the nanotube structure formation as aromatic molecules promote the growth of SWCNTs while aliphatic molecules promote the formation of MWCNTs or non-tubular carbon structures.

Methane as a carbon precursor has a simple composition and is stable in the formation of high-purity SWCNTs (Li et al., 2004). Yahyazadeh and Khoshandam (2017), Ramírez Rodríguez et al. (2018) and Huynh et al. (2021) used methane as the carbon source precursor in CNT synthesis. The synthesis produced SWCNTs and MWCNTs within the temperature range of 750 °C to 950 °C in the presence of a metal catalyst. Bodiba et al. (2018) investigated the precursor of methane and acetylene in producing yarn-type of CNTs at 900 °C assisted by ferrocene as catalyst. Acetylene obtained a higher yield of CNTs compared to methane as the unsaturated hydrocarbon is easier to break the carbon chain. However, the methane produced a better CNT bundle that contains a substantial number of nanotubes with reasonable length and an

excellent spinnable array to produce yarn. Meanwhile, the fabrication of CNT sheets comes directly from the CNT forest that is synthesised by catalytic CVD using acetylene or ethylene. The CNT sheets are made by two approaches: knocking down and drawing (Zhang & Baughman, 2011). The synthesis of high-purity SWCNTs from ethanol on a double-impregnated zeolite matrix at low temperature obtained almost no amorphous carbon (Maruyama et al., 2002).

Futko et al. (2015) and Feng et al. (2017) synthesised CNTs using xylene and ferrocene via injection CVD and studied the growth of vertically oriented CNT arrays that have bamboo-like structures. Furfuryl alcohol (FA) is also a good carbon source that shows a high carbon yield (50 wt.%) for carbon coating of monoliths (Vergunst, 2002) and yields a glassy-porous carbon used in mesoporous absorbent systems (Iroegbu & Hlangothi, 2019). Nanaji et al. (2017) demonstrated the PFA as a carbon source in the synthesis of mesoporous carbon via a modified evaporation-induced self-assembly (EISA). The studies observed that the mesoporous carbon exhibited excellent textural properties with a higher surface area and large pore volume, functionalized mesoporous carbon with superior hydrophilic properties, and more ordered graphitic carbon. The MWCNTs, through decomposition of polyfurfuryl alcohol (PFA) in moderate temperature conditions (500-700 °C), proved the ability of liquid monomer to be polymerized in situ as a thin layer on a solid substrate and grow the CNTs (Ilnicka & Lukaszewicz, 2019). Some literature suggests that the aromatization of PFA to CNTs is based on interchain Diels-Alder addition (Ilnicka & Lukaszewicz, 2019; Tondi et al., 2015).

Catalyst

The metal catalyst is vital in synthesizing CNTs as the presence of the catalyst can reduce the decomposition temperature of the carbon precursor and stimulate the nucleation of CNTs. Different types of CNTs require different types of catalyst. The synthesis of SWCNTs requires a nanosized catalyst, while the MWCNTs can be synthesized with or without a catalyst. MWCNTs have been found to be the most applicable for economical industrial production.

The catalyst acts as the active phase for the decomposition of the carbon precursor and the graphite carbon acts as the deposition centre in the CNT growth process. The preparation of a catalyst is an important factor in achieving effective dispersion of the catalyst and having a specific diameter of CNTs. Commonly, transition metal nanoparticles are used as catalysts, including Fe, Co, Ni, Pd, Pt, Mn, and others. Among the catalysts, Fe, Co, and Ni are most widely used to synthesise the CNTs.

Lin et al. (2020) investigated the growth of CNTs using different catalysts (Ni, Fe, and Co). Results revealed that Ni performances played a significant role in producing larger numbers of CNTs, promoting the densification of TiB_2

ceramics in sintering, providing good reinforcement, and exhibiting a maximum value of flexural strength and toughness. Lee et al. (2002) discovered that the performance of catalysts was reflected in the growth rate and quantity of CNT in the order of Ni > Co > Fe, and the quality of CNTs' growth followed the rank of Fe > Ni > Co. Meanwhile, Dündar-Tekkaya and Karatepe (2015) stated the Fe, Co, and Ni were more active catalysts as the reaction could form metastable carbides, which allow the CNTs' growth and increase carbon efficiency.

Ping et al. (2016) observed the uniform diameter of CNTs on nickel foam via CVD with a Ni/Al molar ratio of 0.1 under calcination and decomposition temperatures of 550 °C and 650 °C, respectively. As a result of increasing the Ni loading, lowering calcination temperature and optimizing the decomposition reaction, carbon production efficiency increased while CNT diameter distribution increased. Furthermore, the techniques of metal catalysts being deposited on the substrate also have an effect on the density, thickness and alignment of CNTs to produce good-quality, vertically aligned nanotubes that can enhance the functionality for the development of high-performance nanotube-based devices (Mohamed Saheed et al., 2014).

Metal support interactions

In catalysis, the support that are usually used are metal oxides, activated carbons or zeolites which are characterized by large, specific areas and the existence of anchoring sites on their surfaces. The metal oxides, including silica, alumina in different allotropic forms, magnesia, and titania, are the most popular among researchers (Serp et al., 2002). The support or substrate plays a role in the mechanism of growth of the CNTs, whereas it could be determined by the interaction of a metal catalyst with the substrate. The interactions between catalyst and support were explored by Allaedini et al. (2015). The studies revealed that the use of MgO and Al_2O_3 as supports showed a weak interaction between support and metal catalyst as the SEM signal observed the tip growth mechanism. On that basis, the different supports have strongly affected the crystallinity of the CNTs, yield, morphology, and microstructure of the catalyst in the synthesis of CNTs. Dündar-Tekkaya and Karatepe (2015) reported the carbon efficiencies of CNTs growth as determined by the chemical bonds formed between the metal catalyst and the substrate, as well as the homogeneous metal dispersion on the surface of substrate.

Reaction conditions

The formation of CNTs does not rely on carbon precursor and catalyst; the synthesis also has strong correlations with reaction condition. The reaction conditions, as well as reaction temperature, reaction time and flow rate of the carbon precursor have a significant effect on the CNTs' formation via CVD. Some literature agrees that the synthesis of CNTs requires higher temperature for the growth of CNTs forest. Mittal and Rhee (2018b) discovered that higher

growth temperatures and longer growth times resulted in a lower I_d/I_g ratio, which means better CNTs growth as analysed via Raman and FESEM. This was also agreed upon by Ming et al. (2016), who found the homogeneous growth of CNTs has been influenced by increasing the reaction temperature on the surface of cooper powder via the CVD method. However, higher temperatures could degrade the structure of CNTs due to the formation of amorphous carbon, which would lower their crystallinity. Kamalakar et al. (2002) observed that higher reaction temperatures (>775 °C) could make the metal particles agglomerate, thus making them less active towards the CNTs growth and leading them to the formation of amorphous carbon. Therefore, the morphology of the tubes should be more stable at a mild or lower temperature (Shukrullah et al., 2019). The consequences of a lower oxidation temperature are attributed to thermal instability that is caused by low crystallinity, defects in the structure, and the smaller diameter of CNTs (Dündar-Tekkaya & Karatepe, 2015). The forest of MWCNTs obtained from cracking ethylene with the assistance of a Fe_2O_3/ Al_2O_3 compound catalyst in a CVD reactor. The catalyst synthesized through co-precipitation is excellent at producing CNTs; the yield varies from 48% to 93% depending on the process temperature and amount of catalyst used. The outer diameter is measured between 40 nm and 100 nm (Shukrullah et al., 2019). Venkatesan et al. (2018) reported the reaction temperature below 700 °C was less effective for growth due to a lesser active site on the surface area of the catalyst, while the temperature greater than 1000 °C was attributed to the deposition of amorphous carbon and disoriented CNTs.

Another reaction factor in CNTs' growth via the CVD method is reaction time. Firdaus et al. (2019) reported the longer reaction time could enhance the CNTs growth due to an increase in carbon and more exposure to a carbon precursor. In the production of MWCNT-coated zeolite Co-beta, Kamalakar et al. (2002) discovered that 90 minutes is the optimum reaction time. However, the longer the reaction time, the lower the growth rate of CNTs due to the deactivation of the catalyst metal particles by the carbon saturation. The longer reaction process also contributed to a smaller diameter of MWCNTs (Navas et al., 2017; Venkatesan et al., 2018), as the higher process time allowed the catalyst activity to occur at an appropriate time (Nagaraju et al., 2002). The reaction process occurring at less than 15 min could defect the outer ring of the CNTs due to insufficient time to complete the growth, whereas the reaction process occurring at more than 35 min created amorphous carbon and defected the structures (Venkatesan et al., 2018). Zhan et al. (2007) observed the trend of the average growth rate declining after 60 min due to loss of catalyst activity with reaction, and Chen et al. (2006) revealed that a short resident time of methane on the catalyst surface is beneficial to synthesising well-graphitized CNTs. Venkatesan et al. (2018) discovered the effect of carbon precursor gas flow rates between 100 and 180 ml/min at constant reaction temperature (900 °C) and reaction time (25 min). They observed that the relationship between carbon precursor flow rate and mean diameter of MWCNTs is directly proportional, as the FESEM morphology showed the diameter distribution ranges from 14 to 22 nm, 25 to 40 nm, and 25 to 52 nm at 100, 140, and 180 ml/min, respectively. This is caused by the diffusion rate of carbon atoms

towards the catalyst, which could affect the dispersion rate of the catalyst. Therefore, the carbon precursor gas flow rate was less than 100 ml/min, and no tubular morphology was observed due to insufficient diffusion of carbon. While at higher flow rates, they exhibited a higher number of tubular CNTs but also attributed the amorphous carbon to be equal to the well-aligned CNTs. Chen et al. (2006), Zhan et al. (2007) and Tee et al. (2009) revealed the carbon yield improved with increasing carbon precursor gas flow rate. Tee et al. (2009) decomposed acetylene with a metal catalyst to produce CNTs with a CVD. They investigated on the role of the carbon precursor flow rate and found that the flow rate varied from 15 to 30 standard cubic centimeters per minute (sccm) and showed an improvement in carbon yield from 63.31 wt.% to 69.28 wt.% over the process temperature and carbon precursor flow rate.

2.7.3 Overview of the parameters used in producing CNT

The overview of the parameters used in producing CNTs is tabulated in Table 2.3.

Table 2.3 : Parameters used in producing CNT

Catalyst	Support substrate	Catalyst deposition method	Carbon source	Reaction conditions	References
Ni, Co, Fe	TiB_2	Precipitation	Ethylene (C_2H_4)	T = 850°C Flowrate (carbon)=100 ml/min time = 120 min	Lin et al. (2020)
Fe	MgO	Impregnation	Acetylene (C_2H_2)	T = 750°C Flowrate (carbon)=300,100 ml/min, time = 30 min	Verma et al. (2020)
Fe/Al	Fe_2O_3/Al_2O_3	-	Liquefied petroleum gas (LPG)	T = 800°C Flowrate (carbon)=100 ml/min time = 2 hrs	Duc Vu Quyen et al. (2019)
Ni/Fe	Basalt fabric	Dip-coating	Methane (CH_4)	T = 950°C Flowrate (carbon)=100 sccm time = 30 min	Mittal and Rhee (2018b)
W and Pt	MgO	Dry impregnation method	Methane (CH_4)	T = 800°C (NH_3 treatment) Flowrate (carbon)=50 sccm time = 30 min	Shah et al. (2018)
Ni	Ni foam	-	Acetylene (C_2H_2)	T = 700°C Flowrate (carbon)=60 sccm time = 30 min	F. Wang et al. (2018)

Table 2.3 : Continued

Catalyst	Support substrate	Catalyst deposition method	Carbon source	Reaction conditions	References
Fe	Al_2O_3	Co-precipitation	Ethylene (C_2H_4)	T = 800°C (NH_3 treatment) Flowrate (carbon)=100 sccm time = 60 min	(Shukrullah et al., 2017)
Ni/Al	Nickel foam	Immersion	Methane (CH_4)	T = 650°C Flowrate (carbon) = 40 ml/min time = 60 min	Ping et al. (2016)
Fe/Cr	Fe/Cr powder	-	Ethanol (C_2H_5OH)	T = 600-650°C time = 60 min	Moonngam et al. (2016)
Ge	Alumina or magnesia	Thermal deposition	Methane (CH_4)	T = 1000°C Flowrate (carbon) = 500 ml/min time = 3 hours	Allaedini et al. (2015)
Fe, Co, Ni, V, and Fe-Co	MgO	-	Acetylene (C_2H_2)	T = 500°C (NH_3 treatment) time = Fe-Co:MgO = 60 min V: MgO = 30 min	Dündar-Tekkaya and Karatepe (2015)
Fe	SiO_2 - alumina	Electron beam evaporation & ferrocene vaporization	Ethylene (C_2H_4)	T = 700°C (NH_3 treatment) Flowrate (carbon) = 700 sccm time = 20 min	Mohamed Saheed et al. (2014)
Fe	Cordierite monolith	Direct injection through CVD	Toluene ($C_6H_5CH_3$)	T = 790°C Flowrate = 10 ml/hr time = 60 min	Minett et al. (2013)
Fe/Al	Silica	Electron beam evaporation method	Acetylene (C_2H_2)	T = 730°C Flowrate (carbon) = 7 sccm time = 20 min	Koji et al. (2013)
Ni, Co, Fe	SiO_2	Thermal deposition	Acetylene (C_2H_2)	T = 950°C (NH_3 treatment) Flowrate (carbon) = 30 sccm time = 10 min	Lee et al. (2002)

2.8 Synthesis method of CNT catalyst

The CNT can serve as a support for catalyst in various application provides numerous benefits. The implementation of this support can demonstrate better stability and resistance to corrosion compared to traditional catalyst supports such as alumina oxide or silica (Akbari & Buntat, 2017). Moreover, the CNT is featured with high specific surface area could facilitate the higher contact between the catalyst and reactant molecules. The CNT is also promote a good thermal conductivity, uniform dispersion of catalyst particles, reduce the strong metal-support interaction which could improve the reducibility of catalyst and increased the dispersion of metal cluster (Esteves et al., 2018). Therefore, research has demonstrated the development of more facile synthesis methods of CNT-supported catalyst that play a prominent role in catalytic reaction process.

The choice of method relies on the specific characteristics required for the CNT-supported catalyst, including particle size, dispersion, and stability. Researchers explore new techniques to enhance the production of CNT-supported catalysts in order to enhance their effectiveness, scalability, and adaptability. Various techniques can be used to attach catalysts onto CNT supports, such as impregnation, CVD, electrodeposition, dip coating, and sol-gel method. The selection of the method is dependent on the catalyst type and desired characteristics of the final CNT-supported catalyst.

The impregnation method is mostly applied in producing CNTs-supported catalyst due to its simplicity, low cost, and versatility. This method can be used to attach a wide range of catalysts onto CNT supports. This method involves immersing CNT into a solution that contains precursor salts of the catalyst desired. The catalyst precursor ions are deposited onto the CNTs surface followed by drying and calcination process to form the catalyst nanoparticles. The impregnation method is widely used (M. Li et al., 2022). Romero-Sáez et al. (2018) also prepared Ni-ZrO_2 catalysts supported on CNT via sequential and co-impregnation that were tested in the CO_2 methanation reaction. The CNT-supported palladium catalyst was loaded by incipient wetness impregnation for the reduction with $NaBH_4$ to shows higher selectivity to hydrocinnamaldehyde (Lamme et al., 2018). The impregnation method can be optimized by manipulating the catalyst precursor concentration, immersion time, drying and calcination conditions. In enhancing the dispersion of the catalyst precursor on the CNT, the method can be modified by using different solvents or surfactants.

Esteves et al. (2018) have reported the CVD is also commonly utilized for both synthesizing CNTs and applying catalysts onto CNTs. The catalyst precursor is introduced into the CVD reactor with the carbon source, resulting in the catalyst being deposited onto the CNTs. Furthermore, the method of electrodeposition method can also be used the CNTs act as substrates for the electrodeposition

of the catalyst, allowing for precise control over the deposition process involves the application of an electrical potential to a solution containing CNTs and the catalyst precursor. Lee et al. (2021) have been synthesized carbon nanotubes grafted on carbon papers as substrates using electrodeposition of $Ni(OH)_2$ catalysts for alkaline oxygen evolution. The benefit of this techniques can tailor the catalyst deposition and achieve high activity and durability, making it a promising method for preparing CNT-supported catalysts. Moreover, Youn et al. (2021) have prepared TiO_2-CNTs as support which prepared via the sol-gel method. The support loaded with Mn and Ce via incipient wetness impregnation method was tested for the low-temperature selective catalytic reduction (SCR) of NO with NH_3. The simplest method and suitable for scaling up the production of CNT supported catalyst are dip coating method which CNTs are immersed into a solution containing the catalyst precursor. The method leads to the formation of a thin, wet film of the catalyst precursor on the CNTs and then dried to convert the catalyst precursor into the final catalyst form.

2.9 Catalyst stability

Catalyst stability refers to the ability of a catalyst to maintain the performance of chemical reaction under a specific operating condition. These factors play a crucial role in various industrial process to determine the sustainability, efficiency, and practical viability of a catalytic process. Hence, the catalyst formulation and process have been developed to optimize the stability, extend the catalyst lifespan, and minimize the impact of deactivation mechanism.

There are some factors affect the stability of catalyst especially Ni based catalyst including support material, ligands, operating conditions and surface modification. Martínez et al. (2018) reported the support material effect the stability of nickel catalyst onto ZrO_2 in CO_2 methanation achieved close to 60% CO_2 conversion and 100% CH_4 selectivity after 250 hours reaction time due to strong Ni-ZrO_2 interaction. Moreover, the Ni catalyst supported on MgO-a-Al_2O_3 were responsible for the lower stability in combined steam and CO_2 reforming of methane compared to those supported on highly ordered structure CeO_2 and SBA-15 due to high NiO dispersion, excellent reducibility and basicity which minimize the inert carbon formation (Hong Phuong et al., 2022).

The nature of ligands also affect the performance of Ni based catalyst in ability to prevent the carbon deposition and sintering of Ni. Shanmugam et al. (2020) found the addition of citric acid (CA) as chelating ligands favored the synergistic effect of Ni and support, which led to high dispersion,. Guilera et al. (2019) evaluated the ability of promoter of La_2O_3 in Ni based catalyst stability of Ni-CeO_2 and Ni-La_2O_3. The promoted catalyst is stable and sustained for a week, while the unpromoted catalyst shows a decline in its activity. Both studies agreed that ligand and promoter assisted in high Ni dispersion,

reducibility, controls the size, stabilizes the Ni nanoparticles and presence of moderate basic sites.

The stability of Ni based catalyst can be influenced by the operating conditions such as temperature, feed composition and reaction time. In high temperature, the catalyst are proned to sintering and suffering from carbon deposition and might initiate deactivation (Meloni et al., 2020; Olivares et al., 2018). Moreover, the surface with presence of oxygenated carbon species can prevent sintering and exert a site blocking that suppresses the side reactions. In several studies, researchers agreed that the sintering is the principal cause of the catalyst deactivation and affect the catalyst stability. Moreover, the findings stated that not only time and temperature influenced the nickel particle sintering but also the H_2O:H_2 ratio. Champon et al. (2020) investigated the sintering study of the Ni/Al_2O_3 commercial catalysts and observed the thermal aging in 200 hours at 450 °C and 100 hours at 600 °C due to loss surface area with time and water product that favor the particle sintering. Steam reforming over nickel catalysts ($Ni/MgAl_2O_4$ and Ni/Al_2O_3) reported the sintering rate of the catalyst increased at 600 °C at 40 bar and approximately 700 °C at 1 bar total pressure (Sehested et al., 2004). Moreover, Ewald et al. (2019) found the several as-prepared Ni catalysts aged at 250, 300 and 350 °C under equilibrium conditions up to 165 hours in CO_2 methanation.

2.10 Kinetic study and model fittings of the CO_2 methanation reaction

Kinetic and modelling studies of the CO_2 methanation reaction over a nickel catalyst can provide an important insight into the reaction mechanism and assist in optimizing the process. Several studies have been conducted to develop kinetic models and understand the reaction dynamics.

2.10.1 Kinetic of the catalytic reaction

CO_2 methanation over a catalyst have been discussed earlier in section 2.2 either direct CO_2 methanation (Equation 2.1) or indirect paths of the CO_2 methanation reaction including, RWGS (Equation 2.2), and CO methanation (Equation 2.3) or combination both direct and indirect path. There are many intermediates and reaction pathways of CH_4 formation however only two widely pathways have been proposed which are formate pathway and CO pathway (L. Li et al., 2022; Schmider et al., 2021).

The formate pathway is also known as CO_2 associative methanation involved the formate species which are the main intermediates product during CO_2 methanation. Initially, the chemisorbed $*CO_2$ species converted to bidentate formate (HCOO*) and proceed to formic acid (HCOOH) and finally to CH_4. While the CO pathway is called as CO_2 dissociative methanation described the

chemisorbed CO_2 species have been dissociated into *CO and *O species. The *CO species further dissociated into *C species which then can be hydrogenated by dissociated H_2 remaining on the metal particle to CH_4 and desorbing from the catalyst surface. Meanwhile, the *O species can combine with hydrogen to produce H_2O. Many studies have reported the both pathways of CO_2 methanation in various Ni-based catalyst as tabulated in Table 2.5.

The reaction mechanism and kinetic description of CO_2 methanation can be explained by several criteria which are (1) different reaction conditions (e.g., temperature, partial pressure), reactor concept, and catalyst used, (2) different assumptions of the governing rate expressions (e.g., Langmuir-Hinshelwood (L-W), Power Law (PL), elementary steps, rate determining step (RDS)) and reaction intermediates (e.g., adsorbed surface species), and (3) different interpretation of the kinetic results (Lalinde et al., 2020). Beforehand, the methanation kinetic approaches applied a simple PL without the assumption of a RDS in describing the reaction. Recently, the kinetic approaches have been employed the complex L-H rate expressions, including adsorption constants for some adsorbed species similar as CO_2, H_2, CO, and H_2O. The model was assumed to adsorb as H_2O or hydroxyl (OH).

The kinetic studies of CO_2 methanation have been applied a simple power rate law (Equation 3.9) which served useful tools for understanding the reaction kinetics. The simple power law of the form Equation 2.6 has been used to initially correlate the rate data (Chiang & Hopper, 1983). Additionally, a power law model in the form of the H_2O partial pressure (Equation 2.7) was included in the rate expression since it influences the rate of reaction, whereas methane is left out because it has no effect on the reaction at all (Hayes et al., 1985).

$$r_{CH_4} = k.p_{H_2}^{x} p_{CO_2}^{y} \tag{2.6}$$

$$r_{CH_4} = k.p_{H_2}^{x} p_{CO_2}^{y} p_{H_2O}^{Z} \tag{2.7}$$

where:

r_{CH_4} = rate of formation of methane (g-mol)/(day)(g of cat)

k = specific reaction rate constant (g-mol)/(day)(g of cat.)

$p_{H_2}, p_{CO_2}, p_{H_2O}$ = partial pressure of hydrogen and carbon dioxide, atm,

x, y = order of reaction parameters for hydrogen and carbon dioxide

Meanwhile, some studies also have been proposed rigorous model of the L-W kinetic to have a better understanding of the reaction kinetics. Therefore, Table 2.4 listed the rate expressions which describes the three different reaction mechanisms (Miguel et al., 2018; Ozdemir & Ark, 2009). Onrubia-Calvo et al. (2022) studied the reaction kinetics of CO_2 methanation over a highly active 8.5% Ni/CeO_2 catalyst in a fixed bed reactor. The mechanistic models of their studies agree with the formate route, in which the hydrogenation of bicarbonate to formate is the rate-determining step. This route on two active sites maintains a high fitting quality of data and provides a higher level of physical activity. The reaction mechanism for the methanation reactions of CO and CO_2 over Ni-based catalysts described by Schmider et al. (2021) provided multiple paths for the conversion of CO and CO_2 into CH_4, including a carbide pathway and direct hydrogenation of CO_2 on the surface. There are different kinetic models for a variety of catalysts proposed by different researchers, as tabulated in Table 2.5.

Model 1: All reactants and products are adsorbed with a single-site mechanism. In this model, two molecules adsorb on neighbouring sites which undergo for bimolecular reaction and desorb as products.

Model 2: All reactants and products are adsorbed with a dual-site mechanism. The dual-site mechanism considering two distinct surface sites are involved in the reaction process which each site can accommodate one species at most. The reactant forms intermediate complexes on these sites before forming product. This model is quite complex due to introducing multiple adsorption sites and interaction during the reaction.

Model 3: Only reactants are adsorbed with a dual-site mechanism. There are two distinct surface sites are involved in the adsorption of reactants which each site can accommodate only one type of adsorbed reactant. The reactant can adsorb independently on different sites before reacting.

2.10.2 Model fittings of the catalytic reaction

The mechanistic aspect of the reaction of CO_2 methanation over Ni CNTs and Co/Ni-CNTs monolith catalyst were studied. The selected model to be fitted with the data to achieve the true rate expression (Equation 2.8 - 2.10) by the model discrimination.

Table 2.4 : Kinetic model for CO_2 methanation reaction

Model	Rate expression	Equation
Model 1	$r_{CH_4} = \frac{kP_{CO_2}P_{H_2}}{(1 + K_{CO_2}P_{CO_2} + K_{H_2}P_{H_2} + K_{CH_4}P_{CH_4} + K_{H_2O}P_{H_2O})}$	2.8
Model 2	$r_{CH_4} = \frac{kP_{CO_2}P_{H_2}}{(1 + K_{CO_2}P_{CO_2} + K_{H_2}P_{H_2} + K_{CH_4}P_{CH_4} + K_{H_2O}P_{H_2O})^2}$	2.9
Model 3	$r_{CH_4} = \frac{k(P_{CO_2}P_{H_2})}{(1 + K_{CO_2}P_{CO_2} + K_{H_2}P_{H_2})}$	2.10

Table 2.5 : Studies on the kinetic models for CO_2 methanation reaction

Catalysts	Main reaction kinetic model	Operating conditions	References
Ni/CeO_2 modified with g-C_3N_4	$r = \frac{k{K_{H_2}}^{0.5} K_{OH} K_{CO_2} {P_{H_2}}^{0.5} P_{CO_2}}{\left(1 + {K_{H_2}}^{0.5} K_{OH} {P_{H_2}}^{-0.5} + K_{CO_2} P_{CO_2}\right)^2}$	T = 210 - 240 °C P = 1 bar	(Yu et al., 2018)
$NiAl(O)_x$	$r = \frac{k\, P_{CO_2}^{1/2} P_{H_2}^{1/2} \left(1 - \frac{P_{CH_4} {P_{H_2O}}^2}{K_{eq} {P_{CH_4}}^4 {}_{H2}\, p_{CO2}}\right)}{\left(1 + {}^2 + {K_{mix}} {P_{CO_2}}^{1/2} + K_{H_2O} P_{H_2O}\right)^2}$	T = 180 - 340 °C P = 1-15 bar	(Koschany et al., 2016)
Ni/CeO_2 nanorods and nanocubes	$r = \frac{k_4 {K_{H_2}}^{0.5} K_{OH} K_{CO_2} {P_{H_2}}^{0.5} P_{CO_2}}{\left(1 + \frac{k {K_{H_2}}^{0.5} K_{OH} K_{CO_2}}{k_6} {P_{H_2}}^{-0.5} {P_{CO_2}}^2\right)^2}$	T = 210 - 240 °C P = 1 bar	(Bian et al., 2020)
Ni/Al hydrotalcite	$r = \frac{k {P_{H_2}}^{0.5} {P_{CO_2}}^{0.5} \left(1 - \frac{P_{CH_4} {P_{H_2O}}^2}{P^4{}_{H_2} P_{CO_2} K_{eq}}\right)}{\left(1 + \sqrt{K_{H_2} P_{H_2} + K_{OH} \left(\frac{P_{H_2O}}{{P_{H_2}}^{0.5}}\right) + K_{mix} {P_{CO_2}}^{0.5}}\right)^2}$	T = 270 - 390 °C P = 1 bar	(Marocco et al., 2018)

Table 2.5 : Continued

Catalysts	Main reaction kinetic model	Operating conditions	References
Ni/Al_2O_3	$r = \frac{k_1 K_{HCOO} P_{CO_2} K_{H_2}{}^{0.5} P_{H_2}{}^{0.5} \left(1 - \frac{P_{CH_4} P_{H_2O}{}^2}{K_{eq} P_{H_2}{}^4 P_{CO_2}}\right)}{\left(1 + K_{H_2}{}^{0.5} P_{H_2}{}^{0.5} K_{HCOO} P_{CO_2} + \sqrt{K_{H_2} P_{H_2}} + K_{OH}\left(\frac{P_{H_2O}}{P_{H_2}{}^{0.5}}\right)\right)^2}$	T = 320 - 420 °C P = 1.2–7.3 bar	(Lalinde et al., 2020)
Ni/CeO_2	$r = \frac{k P_{CO_2} P_{H_2}{}^{0.5} \left(1 - \frac{P_{CH_4} P_{H_2O}{}^2}{K_{eq} P_{H_2}{}^4 P_{CO_2}}\right)}{\left(1 + K_{H_2} P_{H_2}{}^{0.5}\right)\left(1 + K_{CO_2} P_{CO_2}\right) + K_{H_2O} P_{H_2O} + K_{OH}\left(\frac{P_{H_2O}}{P_{H_2}{}^{0.5}}\right)}$	T = 200 - 500 °C P = 1-6 bar	(Onrubia-Calvo et al., 2022)
industrial nickel-based catalyst	$r_{CH_4} = k \frac{P_{H_2}^{0.5} P_{CO_2}}{P_{H_2}^{0.5} + K P_{CO_2}}$	T = 250 - 350 °C P = 1 atm	(Miguel et al., 2018)
Ni/Al_2O_3	$r_{CO_2\ meth} = \frac{k_{CO_2\ meth} K_{H_2} K_{CO_2} P_{H_2} P_{CO_2} \left(1 - \frac{P_{CH_4} P_{H_2O}{}^2}{P_{H_2}{}^4 P_{CO_2} K_{eq\ CO_2\ meth}}\right)}{\left(1 + K_{CO_2} P_{CO_2} + K_{H_2} P_{H_2} + K_{H_2O} + K_{CO} P_{co}\right)^2}$	T = 350 - 450 °C P = 1 bar	(Champon et al., 2019)

2.11 Summary

The literature review showed that the increasing CO_2 concentration in the atmosphere is leading to a great impact on climate change. There are numerous potential approaches that have been proven to be an effective strategy for reducing emissions to the atmosphere. The existing approaches and their limitations have been discussed, including CCS and CCU. Therefore, the realistic approach is discovered by converting the CO_2 into other high value-added products such as C1 compounds (methane, methanol, formic acid, etc.), C2 compounds (ethane, acetic acid, ethanol, formate, etc.), organic carbonates, salicylic acid, and other chemical products. The conversion of CO_2 into methane has drawn a great attention as a useful fuel that also deploys the role of hydrogen carrier, a power-to-gas system (P2G), faster reaction than others, can directly injected into existing natural pipelines and performed under low temperature and atmospheric pressure.

The role of CO_2 methanation as a direct and indirect reaction in producing the products, which involved CO as an intermediate of the reaction, was also discussed in this literature. The limitations of the reaction are affected by temperature, pressure, the presence or absence of promoters, and the catalyst. The catalytic reaction of CO_2 methanation has been discovered using a variety of catalysts that have shown high catalytic performance. In addition, the support of a catalyst has been discussed as it can have an important structural effect, dispersion, and stabilisation of the nanoparticles. There are many supports explored in the form of powder, metal oxide, pellets, and porous materials like foam, carbon, and fiber.

The carbon supported onto monolith could be an attractive support for CO_2 methanation since carbon is unreactive and capable of performing in different porosities to increase the surface area and enhance the dispersion of metal catalyst onto the support surface. Moreover, carbon supported onto monolith can be synthesized using various techniques and methods. CVD processes are the most suitable technique due to the high yield and purity of CNTs, as well as their suitability for structural control or growth parameter control, such as carbon source, catalyst, reaction conditions such as precursor gas flow rate, process time, and reaction temperature. However, to the best of the author's knowledge, little has been said about the catalyst supported on a carbon-supported monolith structure in CO_2 methanation. Therefore, this study focused on the synthesis of catalyst supported CNTs with a monolithic structure, where the catalyst support is expected to contribute to the enhancement of catalyst surface area, catalytic activity, and stability.

CHAPTER 3

RESEARCH METHODOLOGY

3.1 Introduction

This chapter presents the research technique, which is separated into multiple parts. The overall flowchart of the research projects is illustrated in Figure 3.1. The optimization method was designed by Design Expert (DOE) version 7. The physiochemical properties of the CNT monoliths, fresh and spent monolith catalysts were characterized and analyzed using several measurements designed to provide a meaningful assessment of morphological, structural, chemical, surface, thermal, and crystallinity phase determination analysis.

The first part of the study focuses on the production and analysis of a CNT monolith. The Taguchi technique is initially employed to determine the optimum conditions for synthesizing CNTs onto a monolith via CVD. This is accomplished by carrying out two separate sets of studies, with each set comprising nine test runs. Subsequently, the CNT monolith, synthesized under the optimum conditions proposed by Taguchi, is employed as a support for the synthesis of both mono and bimetallic catalysts.

The second part provides the synthesis of both catalysts that are supported on the CNT monolith. The first metal (Ni) loading was determined from the literature to obtain the optimum loading for the monometallic catalyst. Meanwhile, the second metal (Co or Fe) loading was based on the optimum conditions of Ni loading after performing CO_2 methanation reaction designated by Taguchi method. The composition of the second metal to the first metal is only 1 wt.% of the first metal loading. In addition, the CNT monolith was impregnated in each metal (Ni, Co or Fe) catalyst solution as discussed detail in Section 3.3.2.

The third part was the catalytic activity of both catalysts in the CO_2 methanation reaction at the recommended reaction condition by Taguchi method in the second part. The last part of the research was the kinetic studies and applying fitting models to examine the performance of catalysts in CO_2 methanation. This analysis relies on the performance of the most efficient mono and bimetallic catalysts.

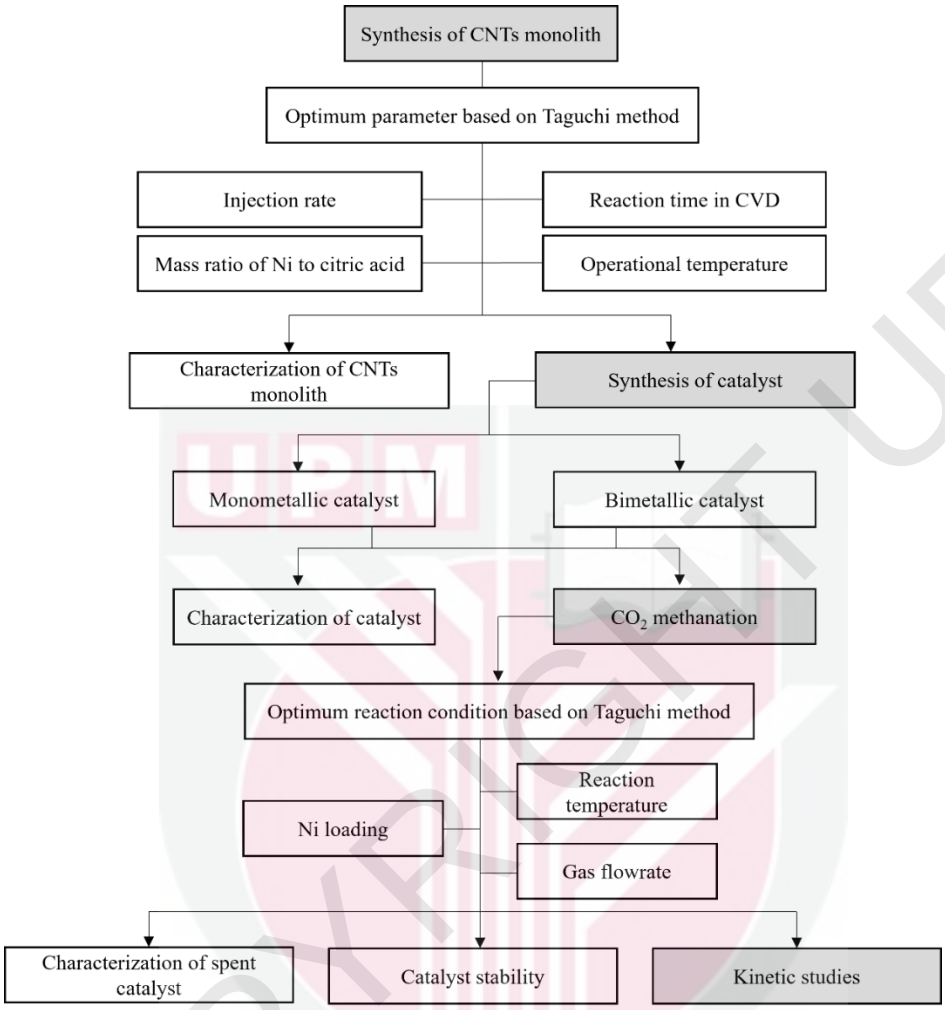

Figure 3.1 : The overall flowchart of the research studies

3.2 Chemicals and equipment

The bare cordierite monolith (Figure 3.2) was used as a support for the CNTs. The cordierite monolith with a cell density of 400 cells per square inch (cpsi) consisting of a cylindrical ceramic type of monolith with an original length of 100 mm and a diameter of 25 mm was purchased from Beihai Huihuang Chemical Packing Co. Ltd., Beihai, Guangxi, China. The chemical compositions of the cordierite monolith were silica (SiO_2) 50.9% ± 1%; alumina (Al_2O_3) 35.2% ± 1%; magnesia (MgO) 13.9% ± 0.5%, and others <1%. As received, the monolith was cut into 10-mm lengths. Nickel nitrate hexahydrates (≥97%), furfuryl alcohol (≥98%), citric acid (≥99%), and ethanol (≥99%) obtained from Systerm, Classic Chemicals Sdn. Bhd., Malaysia were used as

received without further purification. A solution of ethanol was made by combining equal volumes of ethanol and distilled water in a 50:50 ratio. This solution was intended for the cleaning of monoliths. The nickel nitrate salts, and citric acid were combined in distilled water using different solutions of catalyst concentration. The carrier gases utilized in the experiment were industrial nitrogen and pure hydrogen gas, which were provided by Alpha Gas Solution Sdn. Bhd. in Malaysia. The process of calcination in the presence of air was carried out in a furnace, whereas reduction and calcination in carrier gases were performed in a CVD horizontal quartz reactor, as depicted in Figure 3.3. The monolith covered with CNTs was synthesized using the direct liquid injection CVD method.

Figure 3.2 : Bare cordierite monolith.

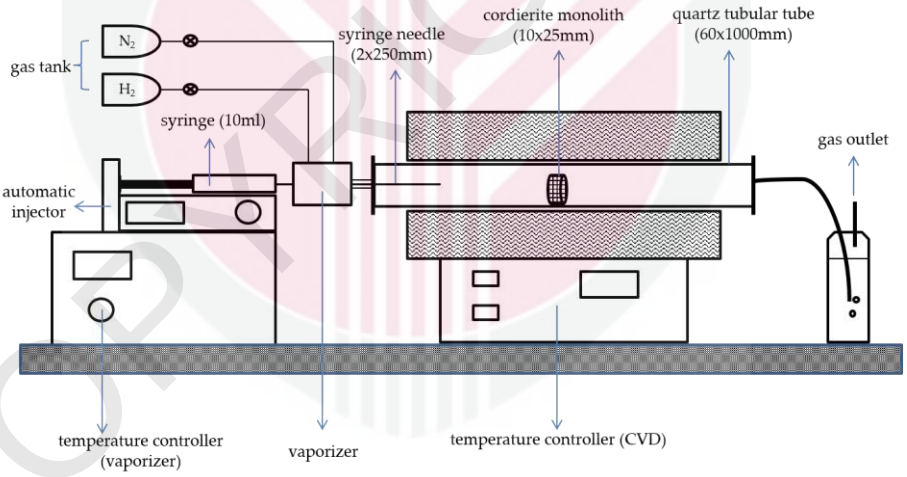

Figure 3.3 : Schematic diagram of CVD horizontal quartz reactor.

The CO_2 methanation activities were conducted in a fixed bed reactor under atmospheric pressure as described in the schematic diagram of the reactor system in Figure 3.4 for the CO_2 methanation reaction. The temperature of the catalyst bed was monitored by a K-type thermocouple in the middle of the catalyst bed. The mixed gases were supplied by Polygas Malaysia Sdn. Bhd. The compositions of outlet gases were analysed by an online gas

chromatography (Agilent Technologies) and the calibration of the gas depicted in Appendix A.

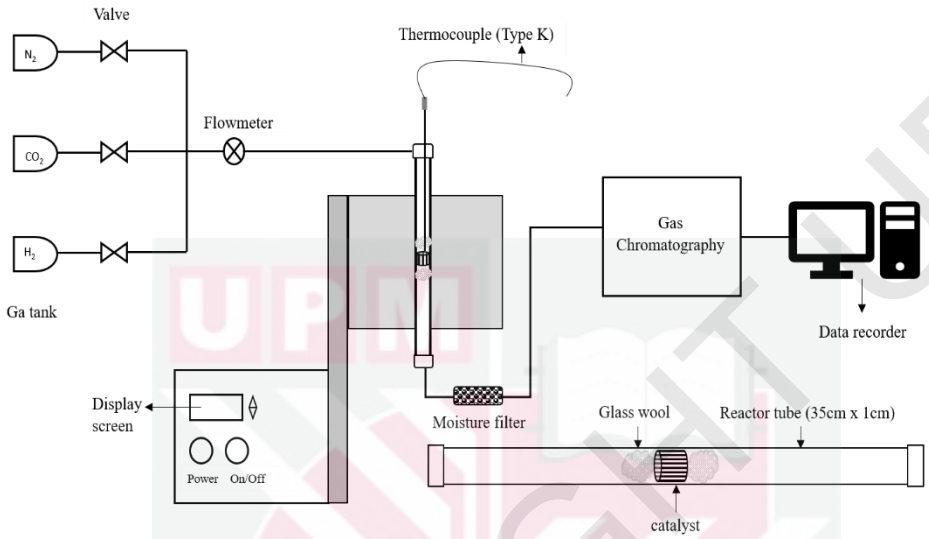

Figure 3.4 : Schematic diagram of reactor system for CO_2 methanation reaction

3.3 Synthesis of CNTs monolith

The synthesis of CNTs was achieved by modifying the method developed by Feng et al. (2015) and Su (2015) via CVD. The process started with the cleaning process, the determination of the optimum condition, and the synthesis of CNTs onto a monolith based on the optimum ones.

As the pretreatment, several cordierite monoliths were immersed in an ethanol solution, which was then placed in a sonicator at a temperature of 80 °C for one hour to eliminate impurities. Afterwards, the clean monolith was dried in an oven at a temperature of 110 °C overnight, and the mass of each monolith was recorded. The metal catalyst, Ni, was fixed at 1 wt.% of the mass of the clean monolith. Therefore, the mole ratio between Ni and citric acid is determined by the mass of the clean monolith. The solution was prepared by dissolving nickel nitrate salts and citric acid in 50 ml of distilled water, using the specific amount determined by the calculations provided in Appendix A1.

Subsequently, the clean monoliths were immersed in a metal/acid solution to evenly disperse the metal across its surface individually in a 50 ml beaker. The

immersion process was conducted for an hour, and the remaining water was blown away using an air gun to remove the slurry excess before drying overnight at 110 °C in the horizontal position and being manually rotated around its axis 3 to 4 times to prevent gravity from causing an uneven distribution. The blowing step was essential in obtaining a homogeneous catalytic layer (Sollier et al., 2018). In addition, the immersed monolith underwent calcination at a temperature of 450 °C in a furnace for a duration of three hours and was weighed to get the mass of Ni coated onto the monolith surface by substracting it from the clean, bare monolith. The process intended to transform $Ni(NO_3)_2$ into NiO, as outlined in Equations (3.1) and (3.2) (Yuvaraj et al., 2003). The immersion and calcination steps were done twice in a full cycle to speed up the growth of CNTs on the monolith support. This was done to increase the dispersion of the active phase.

$$Ni(NO_3)_2 \rightarrow NiO + 2NO_2 + O_2 \quad (3.1)$$

$$NiO + H_2 \rightarrow Ni^{2+} + H_2O \quad (3.2)$$

The Taguchi method, which is explained in Section 3.3.1, was used to growth CNTs on the monolith support using CVD. The chosen parameters, with three levels each for the design, are as indicated in Table 3.1.

Table 3.1 : Parameters and their levels for synthesis of CNT monolith

	Parameters		Level		References
A	Mass ratio of Ni to citric acid	1:1	1:3	1:5	Li et al. (2016)
B	Injection rate (mL/hr)	1	5	10	G. Esquenazi et al. (2018)
C	Reaction time in CVD (minutes)	30	60	90	Mittal and Rhee (2018a); Moonngam et al. (2016); Ping et al. (2016)
D	Operating temperature (°C)	600	700	800	Mittal and Rhee (2018a), Thambiliyagodage et al. (2018), Lin et al. (2018), Tripathi et al. (2014), Pham et al. (2017), G. Esquenazi et al. (2018)

The growth process of CNTs onto monolithic surfaces in CVD was conducted as follows, with the settings listed in Table 3.2:

1. The NiO monolith previously prepared was put into a chamber of the CVD system.
2. The CVD was set at operating temperature and reaction time which designated by the Taguchi method.
3. The flowmeter was set up at 50 atm cm^3/min of N_2 gas. The gas was flowed through the chamber to remove oxygen inside.
4. After the system reached the required temperature, the H_2 gas was slowly flowed at 100 atm cm^3/min into the reaction chamber to combine with the N_2 gas. At this time, the presence of NiO on the surface of the monolith can undergo conversion into Ni^{2+}, which serves as a catalyst for the formation of CNTs.
5. Furfuryl alcohol was injected automatically at a rate using a syringe needle that was 20 inches long. At the same time, H_2 and N_2 gas were kept constant at 100 and 50 atm cm^3/min, respectively, to make sure furfuryl alcohol droplets touched the monolith surface.
6. After injection was completed, the N_2 gas flow speed was adjusted to 500 atm cm^3/min and 50 atm cm^3/min for H_2 gas. The reaction timer was started.
7. When the reaction ended, the H_2 gas was shut off and N_2 was kept flowing at 50 sccm into the setup until it cooled down to room temperature.

Furthermore, the CNT monolith was characterized using FESEM by Thermo Scientific NovaNano 230 at 100k magnification and atomic composition by energy-dispersive X-ray (EDX) by Oxford Instruments, which was attached to the FESEM to evaluate particle size and size of distribution of CNT. Furthermore, the crystallinity of the substrate was analyzed by X-ray diffraction (XRD). The measurement was conducted using a Philips Expert PW3040 XRD operating at 40 kV and 40 mA with a CuKα (λ = 1.5406) radiation source within the 2θ range from 20° to 80° with a 0.033°/min step size. The measurement of disordered carbon was evaluated using Raman spectroscopy by the WITec Raman Microscope model Alpha 300R at a 531.861 nm excitation wavelength within a spectrum range of about 100.36–3736.45.

3.3.1 Optimization study of synthesizing of CNTs monolith based on Taguchi method

The Taguchi method also called as robust design method meant to improve the quality of products and to determine the best levels of control factors. The main focus was to keep the variance in the output very low even in the presence of noise inputs. Therefore, the average and variability of a process performance characteristic, which determines the process's effectiveness, were analyzed in order to ascertain the effect of various parameters. This analysis provided an effective method for designing a product that operates optimally and

consistently across a variety of parameters. The experimental design described by Taguchi utilizes orthogonal arrays to systematically arrange the parameters that impact the process and the varying levels at which they should be manipulated. The development of the design could enhance the experimental results and identify controllable factors. This reduces the variation in response results due to uncontrollable factors.

The Taguchi approach employs pairwise testing of combinations, rather than exhaustive testing of all potential combinations as done in factorial design. This facilitates the gathering of essential data to ascertain the primary parameters that influence product quality, while minimizing the need for extensive experimentation, hence conserving time, and resources. The Taguchi technique is most effective when used to problems with a moderate number of variables (ranging from 3 to 50), few interactions between variables, and when just a small number of variables have a substantial impact. The Taguchi method of CNT growth on monolith was conducted by the Design Expert version 7.0 from Stat-Ease Inc., Minneapolis, Minnesota, USA (2005).

The Taguchi orthogonal array table of $L_9(3^4)$ was used by choosing four parameters that could affect the CNTs growth on the monolith. This type L_9 array was arranged as tabulated on Table 3.2. The letters L and superscript 9 stand for the Latin square and the number of runs was carried out, respectively. The experiments were conducted in two sets of experiments, resulting in a total of 18 runs. After the process, the carbon composition and formation of the CNT structure on the monolith surface were confirmed by chemical and surface analysis. The CNT produced was unpurified, so the carbon yield may be affected by impurities. Then, both sets of experiments were analyzed to determine approximately the percentage of carbon yield on the monolith's surface using Equation (3.3):

$$Carbon\ yield = \left[\left(\frac{M_{total} - M_{cat}}{M_{cat}}\right) x100\right] \tag{3.3}$$

where M_{total} is the total mass of the final catalyst and carbon on the monolith after the CVD reaction process, and M_{cat} is the initial mass of catalyst on the monolith (Taleshi, 2012).

The Taguchi is used S/N ratio as the response in measured the statistical performance. S/N ratio is a performance criterion developed by Taguchi to select the best levels of control variables that minimize the impact of uncontrolled variables. The S/N ratio considers both the average value and the degree of variation. The S/N ratio, expressed in its most basic form, signifies the proportion between the mean (signal) and standard deviation (noise). The response might vary depending on the specific quality features, which can be classified as lower-the better, higher the better, or nominal the best. This

quantitative measurement is employed to determine the optimal conditions (Hamzaçebi et al., 2020).

The S/N proportion takes into consideration the influence of process parameters on the properties of the final product, CNTs yield. The changes in product properties minimized the noise factor and maximized the signal factor (Equation 3.4). The main optimization target S/N ratio of this process utilizes a target that is 'larger is better' (Equation 3.5) to get the maximum yield of CNT growth. The S/N Equations indicate the S/N ratio statistic, where n is the number of experiments, y_i is the output response of the i-th experiment, $\bar{y}$ is the average output response, and σ is the standard deviation (Ross, 1988).

In determining the significant parameters' effect on the production of high carbon yields, the response factor (S/N ratio) of each parameter was ranked according to its delta value. The delta value can be calculated from the difference between the highest and lowest S/N ratio values between the levels of each parameter in the Taguchi method design.

$$S/N\ (dB) = 10\ log\ (Signal\ power/Noise\ power) \tag{3.4}$$

$$\frac{S}{N}_{larger-is-better} = -10\log\left[\frac{1}{n}\sum_{i=1}^{r}\frac{1}{y_i{}^2}\right] \tag{3.5}$$

Table 3.2 : The design of experiment based on the Taguchi orthogonal array table of L_9 (3^4) for CNTs growth onto monolith support

	Mass ratio Ni:CA	**Injection rate of carbon source, C**	**Reaction time**	**Operating temperature**
Run	A	B	C	D
		mL/h	min	°C
1	1:1	1	30	600
2	1:1	5	60	700
3	1:1	10	90	800
4	1:3	1	60	800
5	1:3	5	90	600
6	1:3	10	30	700
7	1:5	1	90	700
8	1:5	5	30	800
9	1:5	10	60	600

3.3.2 Synthesis of CNTs monolith catalyst

In this study, monometallic and bimetallic CNT catalysts were produced to perform in the CO_2 methanation reaction. The monometallic CNT monolith catalysts are prepared at three different Ni concentrations, which were 1, 10, and 25 wt.%, while the bimetallic CNT monolith catalysts are prepared in a mixed metal solution between Ni nitrate and M nitrate (M = Fe or Co) at a 10:1 ratio. The mass of each CNT monolith before and after impregnation was recorded to evaluate the mass of metal catalyst coated onto the CNT surface. All prepared CNT monolith catalysts are evaporated at 80 °C in an oven for 6 to 12 hours. The impregnated CNT monolith is calcined at 450 °C in three hours. All the prepared catalysts are labeled as 1 wt.% Ni-CNTs, 10 wt.% Ni-CNTs, 25 wt.% Ni-CNTs, 1/10 wt.% Ni/Fe-CNTs, and 1/10 wt.% Ni/Co-CNTs.

3.3.3 Catalytic activity

The scope of the experimental work on the catalytic activities of the CO_2 methanation reaction is presented in Figure 3.5. Prior to the evaluation of catalytic activity for the CNTs monolith doped catalysts (monometallic: 1, 10, and 25 wt.% Ni, and bimetallic: 1/10 wt.% Fe/Ni and 1/10 wt.% Co/Ni), the CO_2 methanation reaction was conducted in a fixed-bed reactor under atmospheric pressure. The experiment was conducted using a clean fixed-bed reactor tube having a length of 35 cm and a diameter of 1 cm. In the experiment, about 0.20-0.30 g of CNT monolith catalyst was loaded onto a quartz wool plug in the reactor as described in the schematic diagram of the reactor system for the CO_2 methanation reaction as illustrated Figure 3.4. Initially, the samples were reduced at 400 °C (Müller et al., 2013) as this temperature was selected as stated in the TPR H_2 analysis for 3 h with 5% H_2 gas mixed with Argon at a flow rate of 50 ml/min (L. Wang et al., 2018). The activity was performed at temperature dependence (300 °C, 350 °C, and 400 °C) with reactant mixed gases supplied at 10% CO_2:40% H_2:50% N_2 in the heating process at a flow rate of 30, 50, and 100 ml/min. All the gases were controlled by automatic flowmeter that attached directly to the reactor. The reaction was conducted for three hours to get about 12 data points for the CO_2 conversion and CH_4 selectivity, which were analysed by an online gas chromatography. The CO_2 conversion and CH_4 selectivity were defined using Equations 3.6 to 3.8 as follows (Ge et al., 2019; Vrijburg et al., 2019):

$$CO_2\ conversion \quad = \frac{[CH_4]_{out} + [CO]_{out}}{[CH_4]_{out} + [CO]_{out} + [CO_2]_{out}} \times 100 \tag{3.6}$$

$$CH_4\ selectivity = \frac{[CH_4]_{out}}{[CH_4]_{out} + [CO]_{out}} \times 100 \tag{3.7}$$

$$CO\ selectivity = \frac{[CO]_{out}}{[CH_4]_{out} + [CO]_{out}} \times 100 \quad (3.8)$$

where [X] (X = CO, CO_2 and CH_4) represents the amount (mol/L) of component in the outlet gas. The Equation 3.6 was considered for CO_2 conversion calculation as considering the complete of CO_2 methanation reaction in converting all the reactant into desired products. The conversion of CO_2 based on assumption the sum of inputs equals the sum of outputs. Therefore, the CO_2 conversion was calculated using Equation 3.6 which is based on the product produced and remaining CO_2 compared the common calculation that only based on the measurement of the proportion of CO_2 consumed versus the total feedstock entering the reactor as referred to Vrijburg et al. (2019).

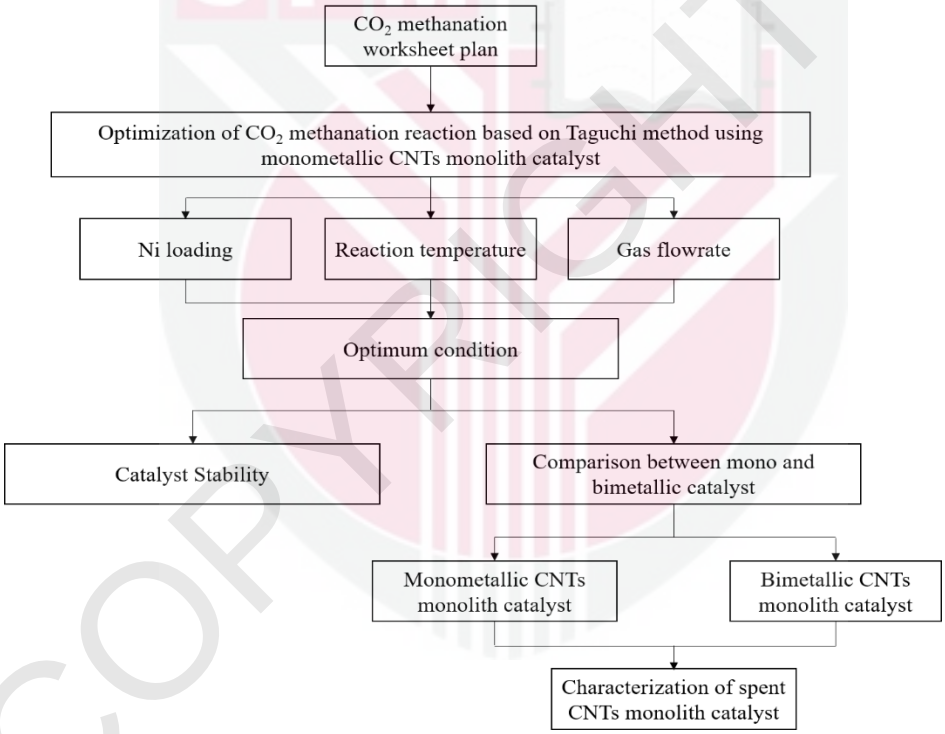

Figure 3.5 : An overview of the scope of the experiment in this section

3.3.4 Optimization of CO_2 methanation reaction based on Taguchi method

The CO_2 methanation reaction catalysed by CNTs monolith catalyst was accessed using Design Expert 7.0 based on the Taguchi method. The experimental design was performed using an orthogonal array of L_9 (3^4) and conducted in a total of 18 runs which considered two replications for each condition. The design of the experiment was designed according to the selected parameters as tabulated in Table 3.3. The Taguchi method design is presented in Table 3.4, and the output response employed the signal-to-noise ratio of 'larger is better' for CO_2 conversion and CH_4 selectivity, while 'smaller-is-better' for CO selectivity. The details of the target responses were discussed in detail in Section 3.3.1.

Table 3.3 : Parameters and their levels for CO_2 methanation reaction

	Parameters	Levels			References
A	Reaction temperature (°C)	300	350	400	(Pan et al., 2014; Tada et al., 2012)
B	Nickel loading (wt.%)	1	10	25	(Aziz, Jalil, Triwahyono, & Saad, 2015; Zhang et al., 2019b)
C	Flowrate (mL/min)	30	50	100	(Vrijburg et al., 2019; L. Wang et al., 2018)

Table 3.4 : The design of experiment based on the Taguchi orthogonal array table of L_9 (3^4) for CO_2 methanation reaction

	Reaction temperature, (°C)	Nickel loading (wt.%)	Flowrate (mL/min)
Run	A	B	C
1	300	1	30
2	300	10	50
3	300	25	100
4	350	1	50
5	350	10	100
6	350	25	30
7	400	1	100
8	400	10	30
9	400	25	50

All the CNT monolith catalysts perform in CO_2 methanation reaction. Both spent monometallic and bimetallic catalysts use for characterisation to analyse the condition of the catalysts after the catalytic activity. The characterisation of spent catalysts focus on chemical analysis (EDX, FTIR), morphology analysis (FESEM), surface analysis (BET), crystallinity, and phase determination (XRD). The details of each analysis discuss in Section 3.4.

3.3.5 Stability of the CNTs monolith catalyst activity

The stability of the best CNTs monolith catalyst activity was evaluated for 210 hours, which is at optimum conditions according to the results from the Taguchi design.

3.3.6 Kinetics and modelling studies

The rate of disappearance for the design equation of a packed-bed reactor has been described by the catalytic reaction kinetics as expressed by Equation 3.9 (Fogler, 2010).

$$r = \frac{FX}{W} \tag{3.9}$$

where:

r = the reaction rate (mol/s.gcat)
F = the molar flow rate (mol/s)
X = the reaction conversion
W = catalyst weight (g)

The equilibrium constant (K_p) of the reaction and the Gibbs free energy of the main reaction (a gas-solid heterogeneous reaction) can be expressed by Equation 3.10 to Equation 3.12 respectively as follows:

$$\Delta G = -RTlnK_p \tag{3.10}$$

$$\Delta G = \sum v_j \Delta H_{fj} - T(\sum v_j S_j) \tag{3.11}$$

By substituting equation 3.9 into Equation 3.11.

$$\sum v_j \Delta H_{fj} - T(\sum v_j S_j) = -RT ln K_p \quad (3.12)$$

where:

ΔG = Gibbs free energy (J/mol)
R = gas constant (J/mol. K)
T = temperature (K)
K_p = equilibrium constant of the reaction
v_j = stoichiometric coefficient
ΔH_{fj} = enthaply of the formation of compound *j* (J/mol)
S_j = entropy of the compound *j* (J/mol. K)

The estimation of K_{p1} theoretical can be described from the Equation 3.13:

$$K_{p_{1\,theoretical}} = \exp\left(\frac{\sum v_j S_j}{R} - \frac{\sum v_j \Delta H_{fj}}{RT}\right) \quad (3.13)$$

The reaction perspective can be expressed by Kp_2 theoretical in Equation 3.14.

$$K_{p_{2\,theoretical}} = \frac{(y_c)(y_d)}{(y_a)(y_b)} \times P_T \quad (3.14)$$

where:

y_{CH_4} = molar fraction of the product c
y_{CO} = molar fraction of product d
y_{CO_2} = molar fraction of reactant a
y_{H_2} = molar fraction of reactant b
P_T = total pressure (1 atm)

The temperature dependence of the kinetic constant (k) in the models described by the Arrhenius equation state in is as expressed in Equation 3.15.

$$k = A \exp(\frac{-E_a}{RT}) \quad (3.15)$$

where:
k = reaction rate constant (mol/atm.g_{cat}.s)
A = frequency factor for reaction (mol/atm.g_{cat}.s)
E_a = activation energy for reaction (kJ/mol)

The CO_2 methanation kinetic measurement data generally supports the Langmuir-Hinshelwood rate models. The mechanistic aspects of the reaction of hydrogenation of CO_2 over Ni-CNTs and Co/Ni-CNTs monolith catalysts were studied.

3.4 Characterization techniques

The focus development of CNT monolith catalysts requires several characterization techniques to evaluate their physicochemical properties. The purpose of catalyst characterization is to understand the relationship between physical, chemical, and catalytic properties.

3.4.1 Morphology analysis

Field emission scanning electron microscopy (FESEM)

FESEM is an advanced analytical tecnique to study the surface morphology at high magnifications. This high-resolution microscopy was liberated electrons from a field emission source to scan small structure according to a zig-zag pattern and observe the small topographic details on the surface or entire of the objects. In this project, Thermo Scientific NovaNano 230 FESEM was used to describe the surface morphology. The particle size of CNTs in FESEM morphology images can be analyzed for generating a size distribution image using Image-J software (Ahsan et al., 2019; Wang et al., 2007)

Transmission electron microscopy (TEM)

TEM provides an important analysis due to its high resolution for studying the quality, shape, size, and density of quantum wells, wires, and dots. TEM image of CNT monolith can observe the atomic resolution and reveal the position atom in the CNT monolith sample. The beam of electrons was transmitted through a specimen to obtain an image. The analysis of the morphology features of the samples was conducted using the Hitachi H-7100 TEM. Prior to the TEM analysis, the samples were prepared by ultrasonic dispersion in absolute ethanol before being placed on the copper grid for 30 minutes and letting them dry in the air.

3.4.2 Structural analysis

Raman spectroscopy

Raman spectroscopy was used to analyse the carbon structural changes (disorder and order) of the samples corresponding to the D and G bands. The D band to a breathing k-point phonon with Al g symmetry and is related to disorders and local defects. Meanwhile, the G band was related to the E_2g phonon of the C sp^2 atoms. Therefore, the measurements of the samples were obtained using the WITec's Raman microscope alpha300 R imaging system with a laser at 532 nm excitation wavelength. The spectra were recorded in the wavenumber range of 100.36**–**3736 cm^{-1}. During the analysis, at least three tests were performed on different sections of each individual sample.

3.4.3 Chemical analysis

Fourier-transform infrared (FTIR)

FTIR is an analytical technique used to determined organic, polymeric and some cases in inorganic material. About 0.05**–**0.1 wt% of the samples were mixed with KBr powder and compressed. The spectra of the samples were measured using the microdie method and PerkinElmer Spectrum 100 at 400**–**4000 cm^{-1} and analyzed the data by comparing the spectra of the sample to reference spectra in libraries or databases to identify the sample's chemical.

Energy dispersive x-ray spectroscopy (EDX)

The analyses of the elemental composition of the CNT monolith catalysts and their atomic composition were conducted using the energy-dispersive X-ray spectroscopy (EDX) by Oxford Instruments, which was attached to the FESEM. These analytical techniques generated data consisting of spectra showing peaks corresponding to the elements of the materials and making up the true elemental composition.

Temperature-programmed desorption (TPD-CO_2)

The interaction between the gaseous reactants and solid substances was investigated using the Thermo Scientific TPDRO 1100 Series by performing the temperature-programmed oxidation of CO_2 (TPD-CO_2). In the pre-treatment, 0.05g of monometallic and bimetallic CNT monolith catalyst were prepared in the flow of Helium gas at 50 °C at 30 ml/min flow rate, prior to the analysis. In the analysis, 5% of CO_2 gas was flowed into argon at a heating rate of 10 °C/min from room temperature up to 950 °C. For the measurement of the oxidation samples via the consumption of CO_2 gas, the thermal conductivity detector (TCD) was employed.

3.4.4 Surface analysis

Surface area and porosity analysis: Brunauer-Emmett Teller (BET)

The pore volume and the specific surface area of the catalyst samples were indicated the N_2 adsorption-desorption isotherm using Micromeritics 3Flex 1.02 (BET surface area measurement). All prepared CNT monolith catalyst samples were degassed automatically at 120 °C for 3 hrs. In determination of the amount gas adsorbed, the desorption and adsorption isotherm were measured using liquid N_2 at 77 K removing across the relative pressure range 0.1 - 1.0 and reduced the pressure. The pore volume and the specific surface area of the catalyst which obtained from adsorption-desorption isotherm were calculated using Brunauer-Emmett Teller (BET) and Berreth-Joyner-Halenda (BJH) method. Pore size distributions were estimated using the DFT equation. The standard classification of adsorption isotherms and hysteresis shapes that released by the International Union of Pure and Applied Chemistry (IUPAC) were used for analysis.

Temperature-programmed desorption (TPR-H_2)

The interaction between the gaseous reactants and solid substances were investigated using Thermo Scientific TPDRO 1100 Series by performing the temperature programmed reduction in H_2 (H_2-TPR). In the pretreatment, 0.05g of catalyst was prepared in the flow of N_2 gas at 50 °C at 25 ml/min flowrate, prior to the analysis. In the analysis, a 5% of H_2 gas was flowed in argon at heating rate of 10 °C/min heating rate from room temperature up to 900 °C. The measurement of the reduction samples via the consumption of the H_2 gas, the thermal conductivity detector (TCD) was employed.

3.4.5 Thermal analysis

Thermogravimetric Analysis (TGA)

Thermogravimetric analysis (TGA) represents the composition of the sample to understand the thermal stability as well as other related properties to the thermal stability measurement. The weight change of the sample was carried out by TA instrument Q50. In this protocol, 10 mg sample in the TGA was kept at room temperature for about 30 min, and then it was heated up to 900°C with a heating rate of 10°C/min in the air for CNTs monolith, while CNTs monolith catalyst were conducted in N_2 gas.

3.4.6 Crystallinity and phase determination

X-ray Diffraction (XRD)

X-ray diffraction is a non-destructive tool that relies on dual waves that contribute patterns after being passed over the material. These patterns were analysed to obtain the phase identification of crystalline materials in the CNT monolith catalysts and can provide the dimensions of unit cells in the crystal structure. The measurement was performed using a Philips Expert PW3040 XRD operating at 40kV and 40mA with CuKα (λ= 0.15418) radiation source within 2θ range from 20 to 80° with a 0.033°/min step size. The average crystal size (d) of CNTs and Ni can be calculated from the Scherrer equation as shown in Equation 3.16 (Abate et al., 2016). The degree crystallinity of the CNT phase pattern was reflected at 2θ = 26.46° and 44.60°, NiO particles at 37.30°, 43.30°, 62.70° and Ni particle reflected at 44.50°, 51.80° and 76.50°.

$$D = k\lambda/\beta\cos\theta \tag{3.16}$$

where:

β = full width at half maximum (FWHM)

θ = diffraction angle

λ = X-ray wavelength (1.54 Å)

D = particle (crystallite) size

k = the Scherer constant (0.91)

3.5 Summary

As the conclusion of this chapter, the overall methodology of the experiments has been discussed. The CNT monoliths have been successfully synthesised based on an optimisation study using the Taguchi method of an orthogonal array table of L_9 (3^4). The optimum condition of CNT monolith was used in producing mono- and bimetallic CNT monolith catalysts. The performance of monometallic CNT monolith catalysts on CO_2 methanation has been investigated under various operating conditions, which were designed using the Taguchi method to achieve the optimum condition of the reaction and evaluate the catalyst stability. In addition, the CO_2 methanation reaction was also applied to the bimetallic CNT monolith catalysts. Furthermore, the kinetic studies and model fittings of CO_2 methanation catalyst activity was conducted for both types of catalysts. The characteristics of CNT monolith, CNT monolith catalysts and spent CNT monolith catalysts were determined to evaluate their abilities before and after the CO_2 methanation reaction.

CHAPTER 4

SYNTHESIS OF CARBON NANOTUBES MONOLITH CATALYST AND APPLICATION IN CO_2 METHANATION

4.1 Introduction

This chapter presents an extensive discussion of the synthesis of CNT monoliths and their catalysts, as well as catalytic activity and kinetic studies. At first, the discussion was focused on the pretreatment of monolith and the synthesis of CNT monolith. The appropriate monolith preparation process must be carried out before the CVD process in order to retain the wall strength of the cordierite monolith after the growth of CNTs. Then, the optimum conditions for CNTs' growth on monolith via direct liquid injection CVD were determined by applying the Taguchi method. The CNT monolith was then characterized and applied to synthesize the CNT monolith catalysts. The discussion was also focused on the catalyst activity of CO_2 methanation in a fixed-bed reactor. Likewise, the Taguchi approach was employed to determine the optimal conditions for catalytic activity. The spent catalyst with the best catalytic performance was characterized, and its stability test was performed. Furthermore, the catalysts, both spent and fresh, were characterized.

4.2 Synthesis of CNT monolith

4.2.1 Pretreatment of monolith

Pretreatment involved preparing the monolith before the CVD process. The treatment aimed to determine the most suitable method for bonding the metal catalyst to a monolith surface: either through immersion or impregnation techniques. In addition to maintain the strength and stability of the monolith structure, the pretreatment aimed to ensure uniform dispersion of the metal catalyst on the monolith surface, leading to a high yield of CNT. The study revealed that the CNT monolith structure created through the impregnation method exhibited brittleness in comparison to the CNT monolith structure produced through the immersion method, as depicted in Figure 4.1. These results were similar to those of Nijhuis et al. (2001), who found that the doping of the metal catalyst via the immersion technique was the best for cordierite monolith, as the structure strength was retained even after the synthesis of CNTs via CVD at 700 °C. Nijhuis et al. (2001) stated that repetitive immersion increased the carbon yield on the surface by enhancing the deposition of more metal on the monolith's surface. The rise in carbon content leads to a reduction in the presence of other elements (Mg, Al, Si, and O) in the cordierite monolith, mainly because of being covered up by the carbon. The results are consistent with the EDX spectrum analysis depicted in Figure 4.2.

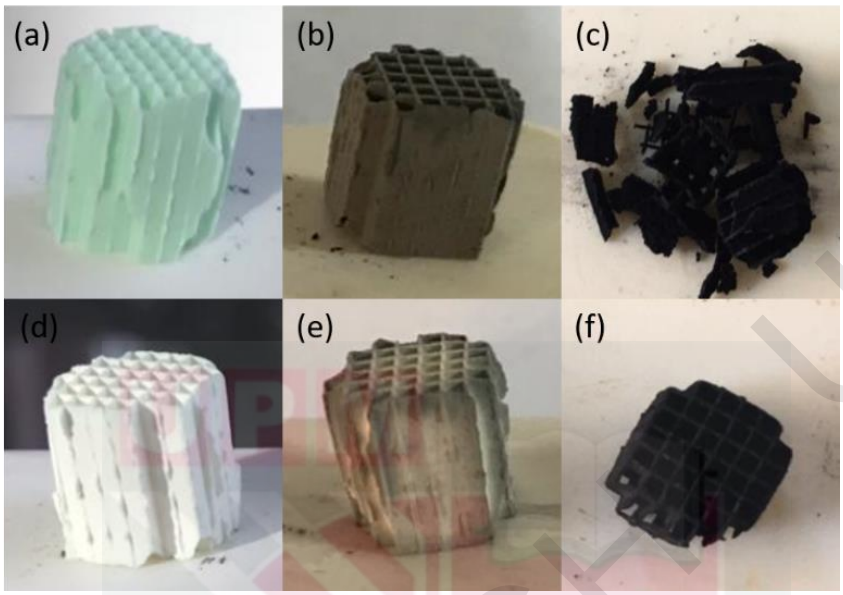

Figure 4.1 : (a) The monolith after impregnation in Ni and citric acid solution, (b) the impregnated monolith was calcined at 450 °C, (c) the CNT monolith produced via impregnation; (d) the monolith after immersion in Ni and citric acid solution, (b) the immersed monolith was calcined at 450 °C, (c) the CNT monolith produced via immersion.

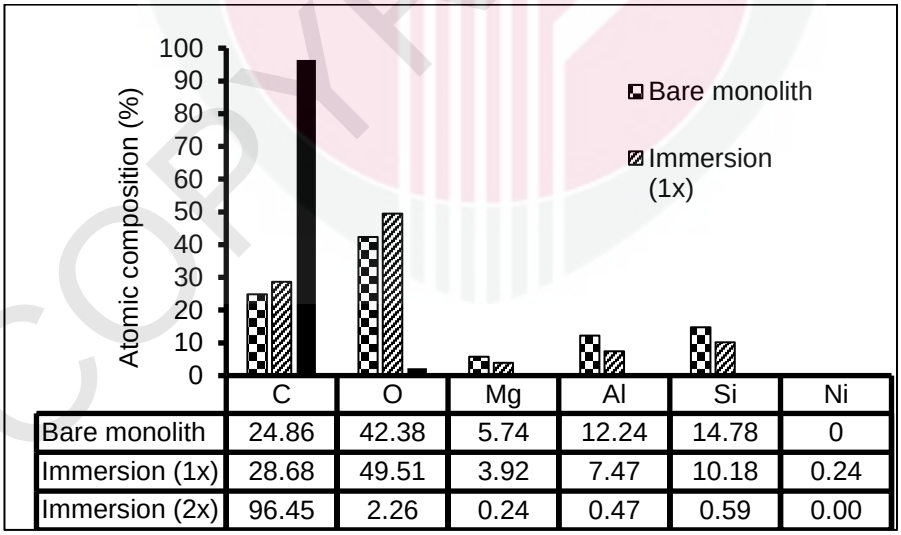

	C	O	Mg	Al	Si	Ni
Bare monolith	24.86	42.38	5.74	12.24	14.78	0
Immersion (1x)	28.68	49.51	3.92	7.47	10.18	0.24
Immersion (2x)	96.45	2.26	0.24	0.47	0.59	0.00

Figure 4.2 : The EDX analysis for the doping method via immersion method

4.2.2 Optimizing study of the CNTs monolith based on Taguchi method

The studies aimed to obtain the optimum conditions for producing a high yield of CNTs via direct liquid injection CVD based on the Taguchi method. Figure 4.3 displays the average percentage yield and standard deviation of the carbon nanotubes' growth under different conditions, as listed in Table 4.1. The importance of the top five average percentage growth rates of the CNTs is shown by the experimental runs of 2, 6, 5, 9, and 7, respectively. The top five runs were clearly conducted at operating temperatures of 600 and 700 °C. Runs 2 and 6 had the highest average percentage growths, occurring at 700 °C with reaction times of 60 min and 30 min, respectively. CNT growth at 600 °C takes more than 60 minutes for the third and fourth places. Thus, the first interpretation from the data analysis in Table 4.1 explained that significant CNT growth could be achieved at 700 °C of operating temperature within 60 min. Furthermore, the other parameters, such as the mass ratio of Ni to CA and the injection rate of the carbon source, showed the highest average CNT growth at a 1:1 Ni to citric acid mass ratio and a 5 mL/h injection rate. The standard errors of carbon yield for all runs were in the range of 0.038–0.743%.

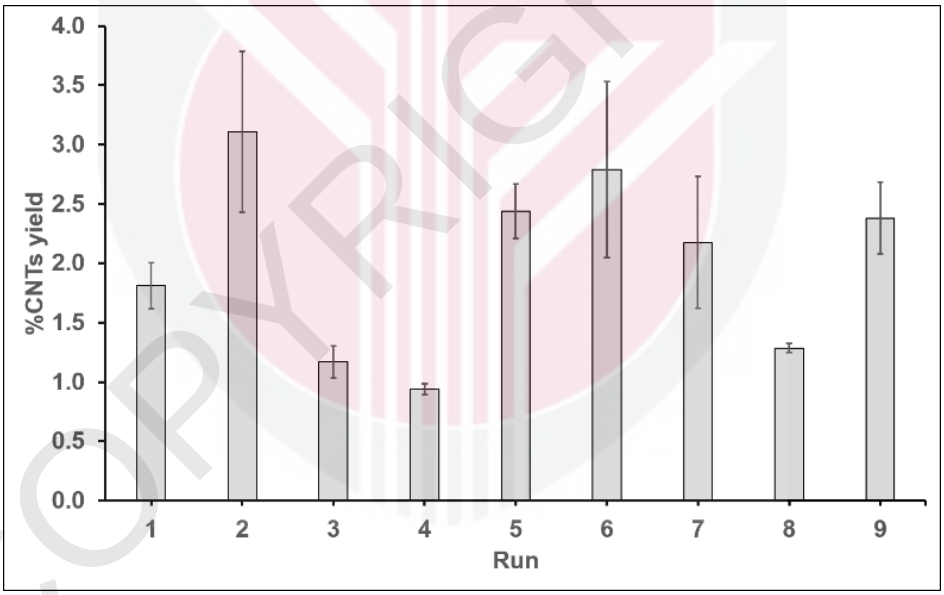

Figure 4.3 : Carbon nanotube yield and standard error for each run of experiments

Table 4.1: Experimentally measured values for CNTs growth and standard error of CNT monolith and signal to noise ratio

	Parameters				*Carbon Yield (CNTs Growth)				Response
Run	A	B	C	D	Yield 1	Yield 2	Average Yield	Standard error	** S/N ratio
		mL/h	min	°C	%	%	%	%	dB
1	1:1	1	30	600	2.005	1.617	1.811	0.194	5.158
2	1:1	5	60	700	3.785	2.433	3.109	0.676	9.852
3	1:1	10	90	800	1.304	1.036	1.170	0.134	1.360
4	1:3	1	60	800	0.986	0.894	0.940	0.046	−0.538
5	1:3	5	90	600	2.670	2.211	2.440	0.229	7.749
6	1:3	10	30	700	2.046	3.533	2.789	0.743	8.910
7	1:5	1	90	700	1.620	2.732	2.176	0.556	6.753
8	1:5	5	30	800	1.325	1.248	1.287	0.038	2.189
9	1:5	10	60	600	2.079	2.684	2.381	0.303	7.536

A: mass ratio Ni:CA, B: injection rate of carbon source, C: reaction time, D: operating temperature.
* The percentage of carbon yield calculated by Equation (3.3).
** The target signal-to-noise ratio is 'larger-is-better' : Equation (3.4).

4.2.3 Response and variance analysis

In this experiment, the Taguchi method applied the S/N ratio and Pareto ANOVA analysis to evaluate the results of experiment which was the output target value (carbon yield). Figure 4.4 described the main effect graph of S/N ratios that states the optimal level of the significant factors in producing high carbon yields through the liquid injection CVD process and the effect significant with S/N ratios ranking in Table 4.2. The optimum level for a factor is the level that contributes to the highest S/N ratio in the experiment. Table 4.2 tabulated the ranking of process parameters for the synthesis of CNTs according to the delta, which is the difference in the response of the S/N ratio between the highest and lowest levels of that ratio within various levels of each parameter. Therefore, the results from Table 4.2 and Figure 4.4 indicate that the optimum conditions for the mass ratio of Ni:CA, the injection rate of carbon, the reaction time, and the operating temperature are A_1, B_2, C_1, and D_2, which are expected to give the highest S/N ratio or the highest carbon yields.

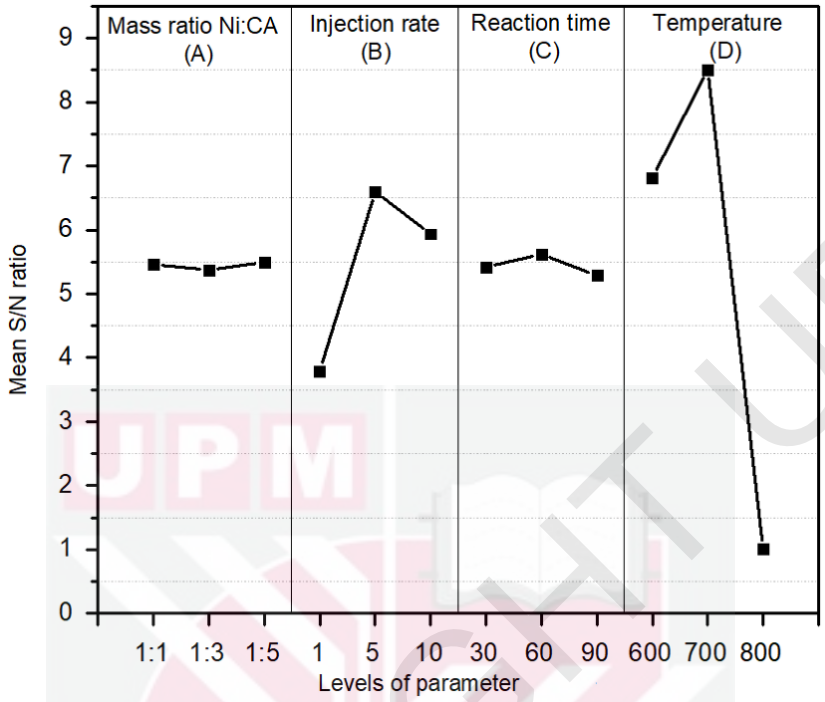

Figure 4.4 : The main effect plots for S/N ratios of process parameters

An analysis of variance (ANOVA) was used to determine the relative effect of the different factors via the decomposition of variance. The analysis of variance was obtained first by computing the sum of squares (SS), followed by the adjusted mean squares (sum of squares divided by degree of freedom). All these values are tabulated in Table 4.3. The percentage contribution of each parameter can be calculated using Equation 4.1 (Xiao et al., 2014). Therefore, the larger the contribution of a factor to the total sum of squares, the greater the ability of that factor to influence the S/N ratio and become a more significant factor. Moreover, the larger the "F-value", the larger will be the factor effect in comparison to the error mean square or the error variance. Referring to the sum of squares in Table 4.3, the factor D makes the largest contribution to the total sum of squares (46.450/52.993 × 100 = 87.65%). The factor B shows the second largest contribution (12.17%) to the total sum of squares, whereas the other two parameters A and C together made only less than 0.2%.

$$\text{Contribution (\%)} = \frac{SS_{adj}}{SS_{Tadj}} \times 100 \qquad (4.1)$$

Table 4.2 : The rank of process parameters for the synthesis of CNTs

	Mass Ratio of Ni:CA	Injection Rate of Carbon	Reaction Time	Operating Temperature
Level	A	B	C	D
1	5.457	3.791	5.419	6.814
2	5.374	6.597	5.617	8.505
3	5.493	5.935	5.287	1.004
Delta	0.119	2.806	0.329	7.501
Rank	4	2	3	1

From Table 4.3, the selected factorial model of the design of the experiment has an “F-value” of 565.79, which implies the model is significant with an “R-squared” of 0.9982. There is only a 0.01% chance that a "model F-Value" this large could occur due to noise. Moreover, the values of "Prob > F" less than 0.0500 indicate that the model terms are significant. Meanwhile, the values greater than 0.1000 indicate that the model terms are not significant. If there are many insignificant model terms, the model reduction may improve the design model. Therefore, from this design, the injection rate of the carbon source (B) and operating temperature (D) are significant model terms, as both parameters serve the largest percentage contribution with a standard deviation of 0.22. The model shows a “Pred-R-Squared” of 0.9911 which is in reasonable agreement with the “Adj R-Squared” of 0.9965. Likewise, “Adeq Precision” as a measurement of the signal-to-noise ratio gives a ratio greater than 4, which is desirable. The ratio of 63.957 indicates an adequate signal and proves this model can be used to navigate the design space.

The factorial model graph was plotted according to selected factors which were the injection rate of the carbon source and the operating temperature as depicted in Figure 4.5. As can be seen, the vertical I-beam-shaped bars have the least significant difference (LSD) at a 95% confidence level (by default). This statistical plot further reinforces that the injection rate of the carbon source (B) and the operating temperature (D) influenced the CNT growth significantly, as proven from the ANOVA analysis. The advantage of the Taguchi orthogonal array design is that it provides the evaluation feature for examining aliases. In other words, it is good to proceed with a follow-up experiment to confirm and validate the effects of temperature and volume of carbon sources.

Table 4.3 : Summary of ANOVA for selected factorial model

	Degree of Freedom (DF)	Sum of Squares (SS)	Adjusted Mean Square (Adj. SS)	Percentage Contribution (%)	F-Value	p-Value Prob > F
A	2	0.022	0.011	0.020		
B	2	12.910	6.450	12.170	138.060	0.0002
C	2	0.160	0.082	0.160		
D	2	92.900	46.450	87.650	993.520	<0.0001
Model B & D	4	105.810	26.450		565.790	<0.0001
Total A,B,C, D	8	105.640	52.993	100.00		
R-Squared		0.9982 (significant)				
Adj. R-Squared		0.9965				
Pred-R-Squared		0.9911				
Adeq Precision		63.957				
Std. Dev.		0.22				

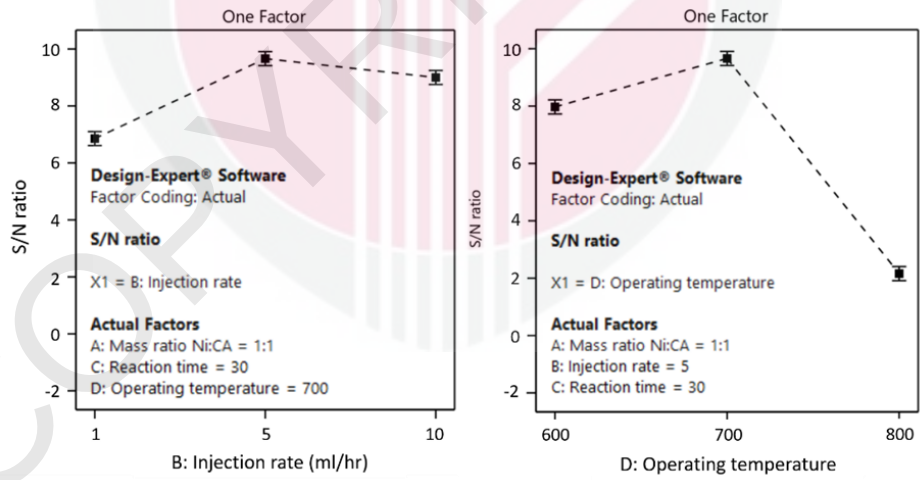

Figure 4.5 : One plot factor of the main effect: (a) injection rate; (b) operating temperature

4.2.4 Confirmation test at optimum condition

Finally, based on the S/N ratio diagrams (Figure 4.5) with an optimum yield of CNT growth, a verification experiment was conducted according to the selected suggestions as tabulated in Table 4.4. The experiment was performed to investigate through a prediction the performance of CNT growth yield at optimal process conditions, and the confirmation experiment to verify the consistency of the optimisation results via the suggested conditions of the Taguchi method was carried out. The validation test was conducted with duplicates. Therefore, the acquired results exhibit a good agreement based on the actual S/N ratio of 9.5349 dB compared to the predicted result of the Taguchi method, which was 9.6609 dB, as the actual values of the average percentage carbon yield deviated only 1.4% from the predicted ones.

Table 4.4 : The optimal configuration with predicted and actual S/N ratio value

		Optimization Prediction					Optimization Results	
		Parameter			S/N Ratio Predicted	Yield CNTs Growth	S/N Ratio Actual	Yield CNTs Growth
Run	A	B	C	D	dB	%	dB	%
1	1:1	5	30	700	9.6609	3.0415	9.7502	3.0726
2	1:1	5	30	700	9.6609	3.0415	9.3195	2.9240
Average					9.6609	3.0415	9.5349	2.9983
Standard error							0.1758	0.0607

4.2.5 Characterization of CNTs monolith

The CNTs were synthesized by the CVD method onto a monolith's structure and acted as an alternative support for a catalyst. The CNTs' presence on the monolith surface was crucial for increasing the surface area to which catalysts could adhere. Moreover, the advantages the structured CNTs enhanced mass and heat transfer, helping to limit hot-spot formation, avoid catalyst deactivation, control process selectivity, and provide an alternative to standard powder catalysts that can improve the catalytic activity and selectivity of CO_2 to CH_4 (Cepollaro et al., 2022; Chagas et al., 2023). The characterization of the CNTs was evaluated using morphology, structural, chemical, surface, thermal, and crystallinity analyses.

The morphology and microstructure of CNT monolith are illustrated by FESEM and TEM. The Figure 4.6 depicted the morphology analysis of the bare cordierite monolith and CNT monolith at optimum condition. In determining the CNT diameter size distribution, 60 points have been selected, and all points are

displayed in Figure 4.6 (d). The FESEM micrograph showed the biggest size distribution of CNTs was about 30–35 nm in range, which are mesoporous nanotubes. The diameter of the nanotubes grown affected by the size of the catalyst use in the synthesis of CNTs as the larger particles nucleating CNTs with similar diameters while smaller particles nucleate narrower CNTs. Consequently, the size of CNTs also has a significant impact on the catalyst activity. The large size of nanotubes plays a crucial role in determining in catalytic activity and structure of the catalyst (Harutyunyan et al., 2006). Meanwhile, smaller diameter CNTs have higher catalytic activity for catalysts supported on carbon nanotubes (CNTs) due to a larger specific surface area and more oxygen-containing groups, which facilitate the dispersion of the catalyst particles (Tang et al., 2007; Wang et al., 2015).

Moreover, the CNT growth at optimum conditions showed more uniform tubes by diameter due to fewer tube defects and the formation of less amorphous carbon, as observed in the FESEM image. He et al. (2008) reported that the production of CNTs with a narrow distribution of diameter was contributed by more uniform and small Ni nanoparticles dispersed onto the surface. Using high-resolution TEM images, a further detail of the CNTs' microstructure with the formation at various sizes. As can be seen in Figure 4.7 and supported morphology of CNTs in Figure 4.6, the observed the CNTs with yarn-type CNT growth were obviously showed the Ni catalyst particles were encapsulated at the tips of tubes and covered by graphitic caps. This analysis described the tip-growth mechanism which also similar to Chen et al. (2004); Ming et al. (2016).

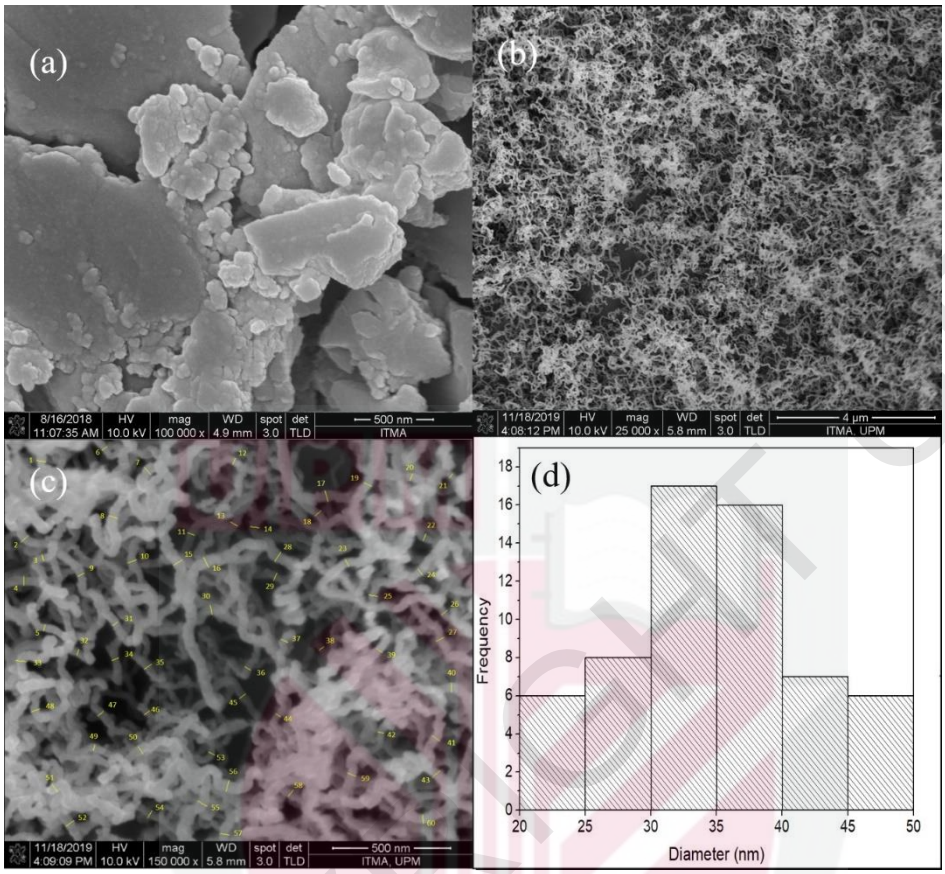

Figure 4.6 : (a) Micrograph image of bare cordierite monolith; (b) CNT monolith at optimum condition using FESEM at 25 000 magnification; (c) CNT monolith at optimum condition using FESEM at 150 000 magnification and (d) size distribution of CNTs growth at optimum condition.

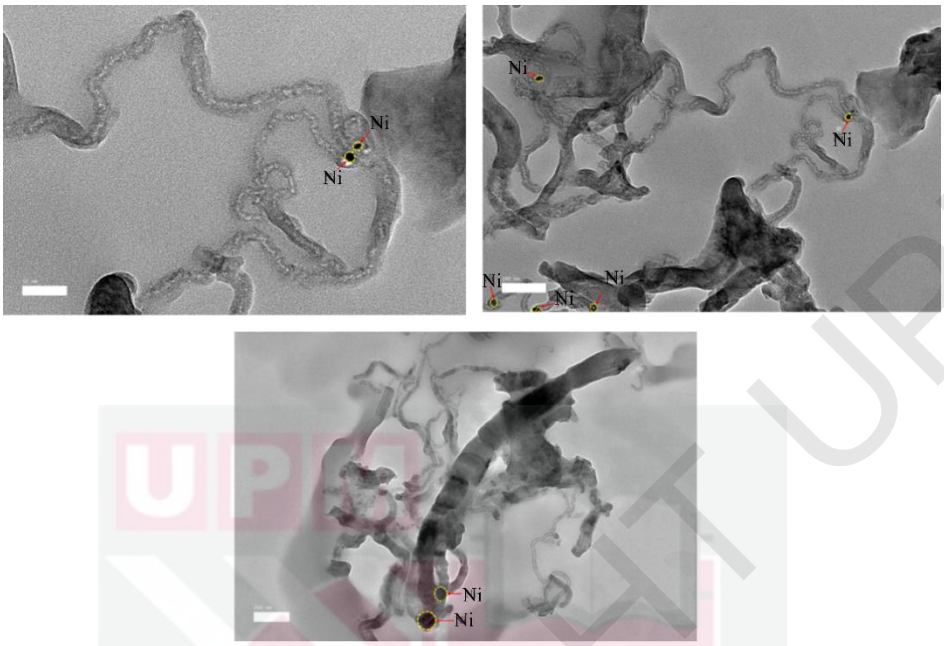

Figure 4.7 : Microstructure observation of CNTs monolith

Raman spectroscopy was used to characterise the carbonaceous materials to distinguish disordered and ordered crystal structures of carbon by illustrating the characteristics of the D and G bands of the samples. In this case, the D band represents the impurities and lattice disorder in the nanotubes. Meanwhile, the G band corresponds to the degree of graphitisation of CNTs, such as their purity and quality resulting from the bond stretching of the sp^2 carbon pairs (Shahriary & Athawale, 2014). Moreover, the G band indicates the graphene layer as s single, double, or triple layer of the sample. Figure 4.8 shows the Raman spectra of the CNT growth onto the monolith produced at optimum conditions. The CNT monolith indicates a higher G band of about 7.84 in intensity compared to the D band. The degree of disorder in the CNT monolith was 0.9921, expressed by the intensity ratio of the D band to the G band (I_D/I_G), which is also an indicator of the sp^3/sp^2 carbon ratio. Therefore, the higher ratio indicates the presence of amorphous carbon and structural defects in the sample, while the lower I_D/I_G ratios show better graphitisation of CNT structures.

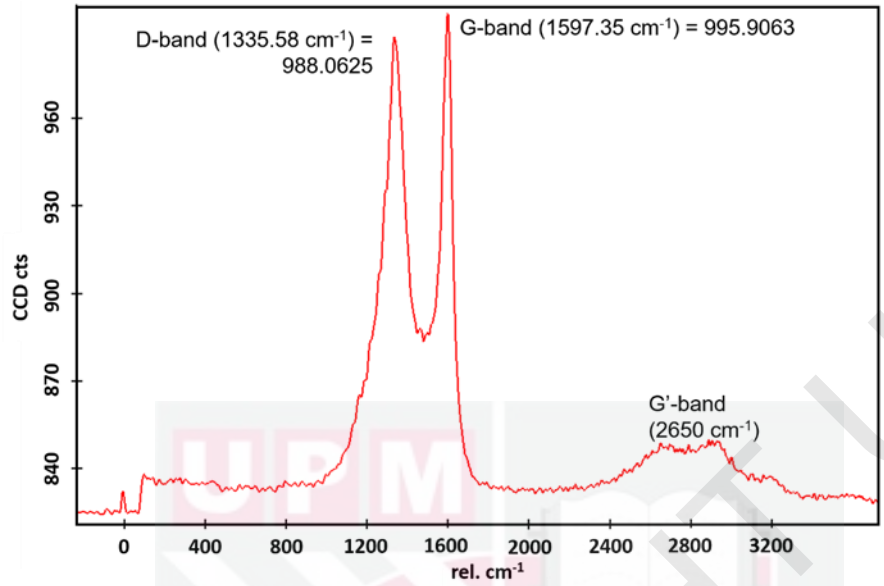

Figure 4.8 : Raman spectra of CNT monolith

The FTIR spectra displayed frequencies of absorbed radiation that were unique to each molecule due to bond strength, atom number, condition of material (such as the state, interference or contamination, concentration, and temperature), and the multiplicity of bending and stretching vibration modes. Figure 4.9 shows the FTIR analysis of bare cordierite monolith, Ni coated onto bare monolith, furfuryl alcohol (carbon source), and CNT formation on monolith that were recorded in the region of 4000 to 650 cm $^{-1}$. The FTIR spectrum of a bare cordierite monolith exhibited a strong peak, as illustrated in Figure 4.9 (a). After immersion in Ni solution, the spectrum became weak, as shown in Figure 4.9 (b). The intense peaks of furfuryl alcohol (Figure 4.9 (c)) have been observed very weak after CNTs growth onto the monolith (Figure 4.9 (d)) and look similar with MWCNTs reported by Haniyeh et al. (2013) due to poor infrared transmittance of CNTs. The main spectra presents the absorbance peaks at wavelength 3600 to 3200 cm^{-1} (stretching of O-H functional group), 3000 to 2700 cm^{-1} (stretching of C-H functional group), and wavenumbers 1500 to 900 cm^{-1} (C-O functional group) as general (Munajad & Subroto, 2018). Metal oxide nanoparticles have a spectrum of <1000 cm^{-1}, with peaks appearing around 400 and 700 cm^{-1}depending on the type of metal oxide (Gupta & Saleh, 2011). The water molecules with n=3 have three peaks of vibrations which are stretching vibrations at peaks between 3450–3200 cm^{-1} (O-H), 1640–1630 cm^{-1} (H-H), and one scissors-bending vibration 2130–2110 cm^{-1} (H-O-H) (Rakić et al., 2003).

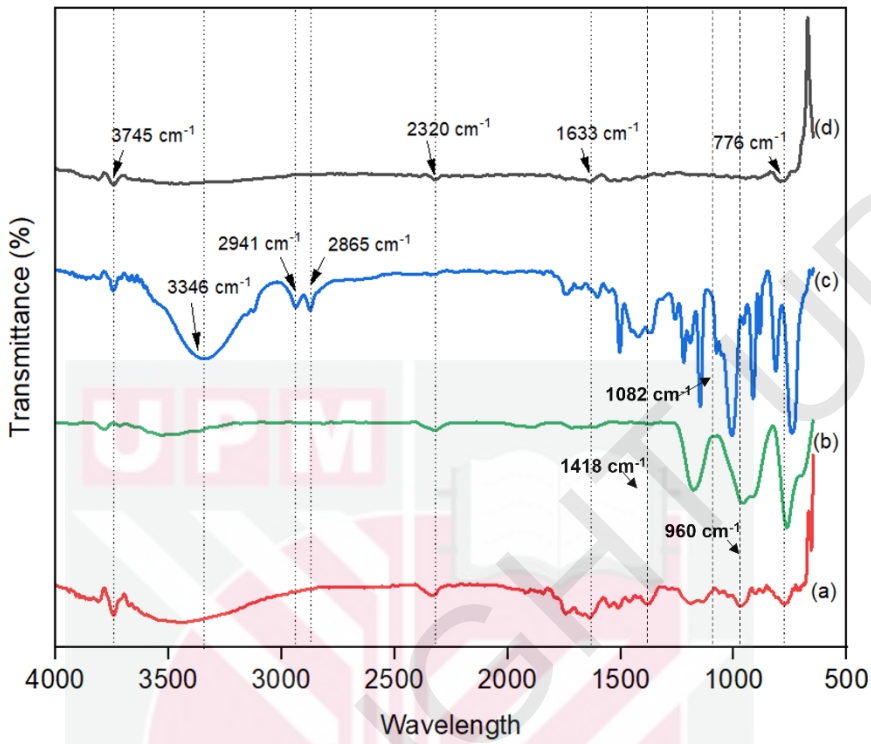

Figure 4.9 : FTIR profile of (a) bare cordierite monolith, (b) Ni coated cordierite monolith, (c) furfuryl alcohol (carbon source) and (d) CNTs monolith

The hexagonal structure of CNTs is confirmed by peaks at 3745 cm^{-1} assigned to free hydroxyl groups (Atieh et al., 2010; Mansor et al., 2012). A broad peaks at about 3346 and 3500 cm^{-1} corresponded to O-H stretching of hydroxyl groups from carboxyl groups (O=C-OH and C-OH) which refers to intermolecular hydrogen bonded OH:OH, adsorbed water or surface carboxylic (Barrios et al., 2012; Dubey et al., 2005). The presence of carboxyl groups on the surface of CNTs may be due to the partial oxidation that occurs during their synthesis (Azri et al., 2017). The peaks at 2865 cm^{-1} and 2941 cm^{-1} only appear for furfuryl alcohol and describe the symmetric and asymmetric vibrations of methylene bonding from -CH_2OH groups in furfuryl alcohol (Liang et al., 2017). Moreover, the peak at 2320 cm^{-1} can be associated with the O-H stretch from strongly hydrogen-bonded -COOH (Atieh et al., 2010). While peaks at 1633 cm^{-1} are attributed to the aromatic like C=C stretching mode of the CNTs' graphitic layers or carbonyl groups (Osman et al., 2020). The peak at 776 cm^{-1} is assigned as Ni oxide nanoparticles which acts as catalyst in the synthesizing CNTs monolith (Gupta & Saleh, 2011). Meanwhile, Al oxide, Mg oxide and Si oxide particles that origin from cordierite monolith are assigned at 1082 cm^{-1} , 960 cm^{-1} (Avotina et al., 2023) and 1418 cm^{-1} (Zahir et al., 2019)

respectively. Thus, all the peaks are reduced significantly as the decomposition of furfuryl alcohol into CNTs onto cordierite monolith surface.

The EDX spectrum of the CNT monolith is shown in Figure 4.10. From the analysis, the EDX spectrum presents 96.45% of the carbon composition in the sample, representing CNT growth on the surface of the monolith. The carbon composition is very high due to the dispersion of the metal catalyst onto the surface, which enhanced the CNTs' growth. However, the Ni composition disappeared onto the CNT monolith due to high CNT growth, which led to a possible covering of all Ni on the surface with the carbon. Therefore, the results from the repetition of the immersion technique for dispersing more Ni catalyst onto the monolith, as explained in section 4.2, were in parallel with the results from Lee et al. (2015) which observed that the thickness of the catalyst has a linear relationship between nanoparticles and the diameter of the nanotubes. Therefore, the thickness strongly affects the CNT nanotubes' diameter and the morphology of the nanoparticles formed during the process without influencing the quality of the CNTs (Lee et al., 2015).

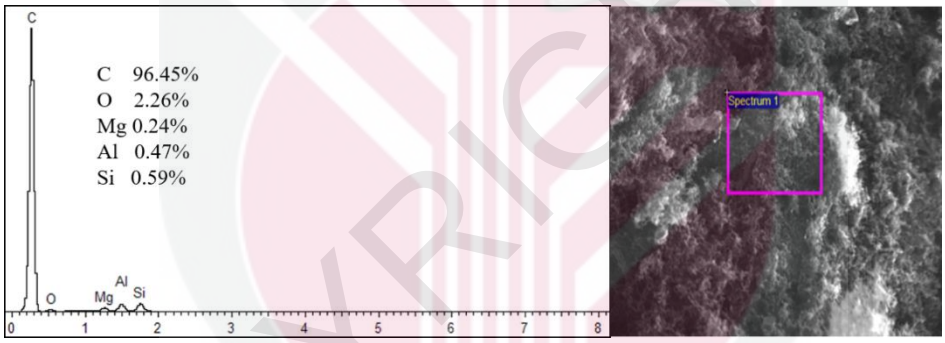

Figure 4.10 : EDX spectrum of CNTs monolith

The surface analysis plays a key role in adsorption which has a significant impact on the catalyst performances. The CNTs' properties result in different surface areas, which are influenced by the number of walls, tube diameter, surface functionalisation, and metal and amorphous carbon impurities (Birch et al., 2013). The BET-specific surface area, pore size, and pore volume distribution of bare monolith and CNT monolith samples were analysed using the N_2 adsorption/desorption isotherm. The isotherm of all classified samples, in which two branches are parallel over a wide range of the P/P_o due to the IUPAC standard classification, is shown in Figure 4.11. The isotherm of a bare monolith and CNTs exhibits type IV isotherm, accompanied by hysteresis H3, indicating the presence of mesoporous structure. Thommes et al. (2015) addressed that the type IV isotherm showed the samples remain nearly horizontal over the higher relative pressure range if a mesoporous adsorbent contains no macropores. This type of isotherm explains the adsorption behaviour in mesopores, which is determined by the adsorbent-adsorptive

interaction and the interaction between molecules in the condensate. The initial monolayer-multilayer adsorption on the mesoporous wall has the same path as Type II. The isotherm of the CNT monolith synthesised via immersion and CVD technique observed the relative pressure range at $P/P_o > 0.4$, which is consistent with the findings of Malekbala et al. (2019) and Di et al. (2018). Moreover, the isotherm of each type of CNT monolith has a low adsorption compared to the study by Tian et al. (2015) which reported the specific surface area (SSA) of more than 200 m^2/g of CNTs prepared hydrothermally using ammonia, hydrogen peroxide, and a metal catalyst. The BET value reveals an SSA value of 15.1178 m^2/g, which is similar to that reported by Kang and Moon (2013) where the CNTs possess a relatively small specific area compared to activated carbon. The main reason is that activated carbon has mainly micropores which make a higher contribution to the surface area while the CNTs has mesopores distributed from 2 to 50 nm (Freitas et al., 2021). The CNTs' growth on the monolith's surface increased the surface area by about 35% of the clean, bare monolith. The low surface area of MWCNTs was attributed to a large amount of impurities such as amorphous carbon particle, multilayer polygonal particles and large graphite platelet. All the BET surface area, pore area, and pore volume were determined from the pore size distribution curves in the desorption curves of isotherm via the BJH method, as tabulated in Table 4.5.

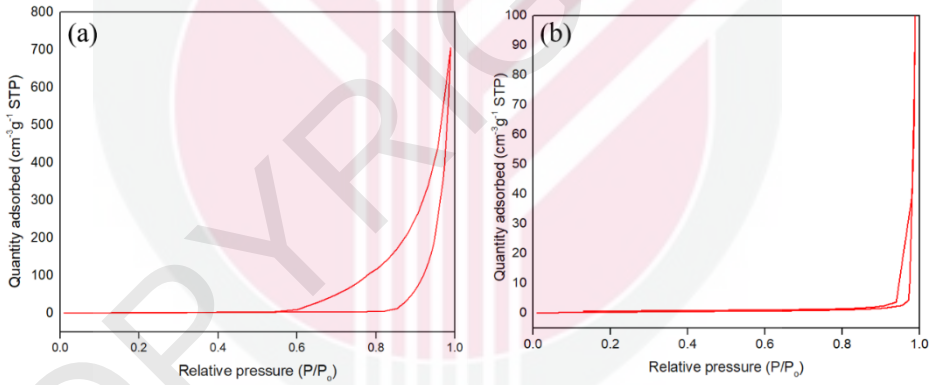

Figure 4.11 : Nitrogen adsorption-desorption isotherms of (a) bare cordierite monolith and (b) CNTs monolith

Table 4.5 : The surface analysis of bare monolith and CNTs monolith

Types	[a]BET surface area (m^2/g)	[b]Pore volume (cm^3/g)	Pore size (nm)
clean bare monolith	11.140	1.0887	39.092
CNTs monolith	15.118	0.1064	50.294

a calculated by BET equation
b BJH desorption pore volume

The thermogravimetric analysis of the CNT monolith is depicted in Figure 4.12. The analysis provided the information of the vaporization and oxidation as the material sample is heated and subjected to thermal decomposition in a controlled atmosphere up to 900 °C to record the mass change. As a results, the first observed temperature around 105 °C showed of 0.12% weight loss at the start of the TGA curve due to evaporation and dehydration of adsorbed and surface water from the material. The second weigh loss is about 2.85% mass loss is observed at 400 °C and a complete weight loss was observed at a temperature of around 680°C. This is due to the oxidation of CNT by oxygen that also reported by Yuefeng Liu et al. (2013).

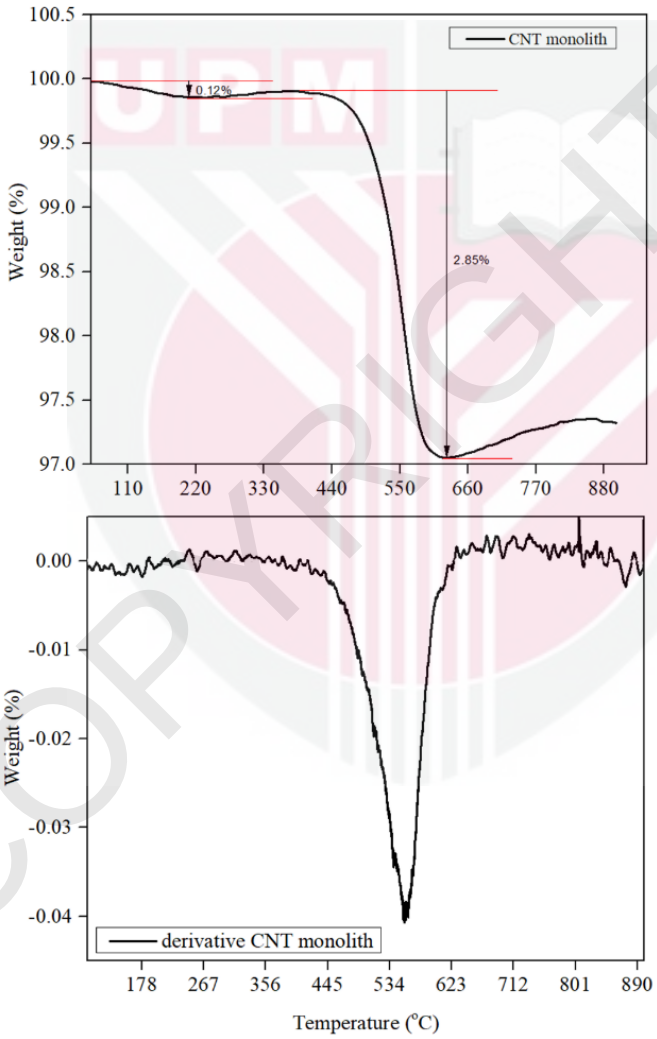

Figure 4.12 : TGA analysis of CNTs

Figure 4.13 represents the X-ray diffraction (XRD) patterns of cordierite monolithic support and the CNT growth under optimum conditions. The strong XRD patterns shown mostly correspond to the cordierite phase (International Centre for Diffraction Data (ICDD) file No. 00-012-0303). The patterns show not much difference between the CNT phase patterns of reflection at 2θ = 26.46°(002) and 44.60°(004) according to ICDD file No.00-001-0646 with a hexagonal crystal system (Anjalin, 2014). The crystallite sizes of CNTs at both 2θ are 44.83 nm determined using Scherrer equation (Equation 3.18). This could be because no acid was treated on the cordierite monolith surface as citric acid is a weak acid. Therefore, Al, Si, and Mg would not be leached when the material was immersed in an acidic condition. The Al and Mg would be leached easily in strong acid rather than Si as both have basic characters (García-Bordejé et al., 2002; Soghrati et al., 2014). Furthermore, a weak reflection at 2θ = 37.30°, 43.30°, and 62.70° indicates NiO (ICDD file No. 00-002-1216) while 2θ = 44.50°, 51.80° and 76.50° indicates Ni (ICDD file No. 00-004-0850).

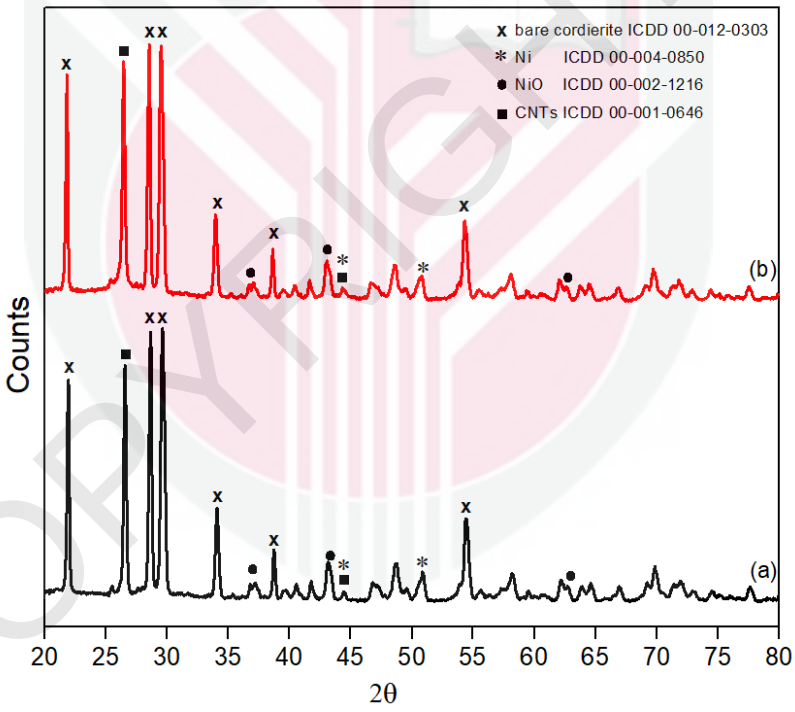

Figure 4.13 : XRD pattern of (a) bare monolith and (b) CNT monolith

4.3 CNTs monolith catalyst

In the CO_2 methanation reaction, Ni is a standard catalyst due to its high activity and low cost. One of the challenges of this catalyst was that Ni tends to agglomerate and cause carbon deposition during high-temperature reactions (Mohd Ridzuan et al., 2022). Additionally, the type of support used can influence the degree of promotion of Ni as a catalyst. Therefore, the Ni-structured catalyst as illustrated in Figure 4.14 was synthesized to be used in the CO_2 methanation reaction. In these studies, the catalytic activities were performed using CNTs monolith catalyst. The CNT monolith was used as support and Ni as a single metal catalyst was initially used at different loadings to study the capability of a single metal structured catalyst. The intent of having CNTs on the surface of cordierite monoliths is to enhance the catalytic performance, improve thermal stability which can lead to better overall properties and performance of the composite material. The catalyst is prepared in two categories: monometallic and bimetallic. The monometallic CNT monolith catalyst was studied at three different Ni loadings: 1 wt.%, 10 wt.%, and 25 wt.%.

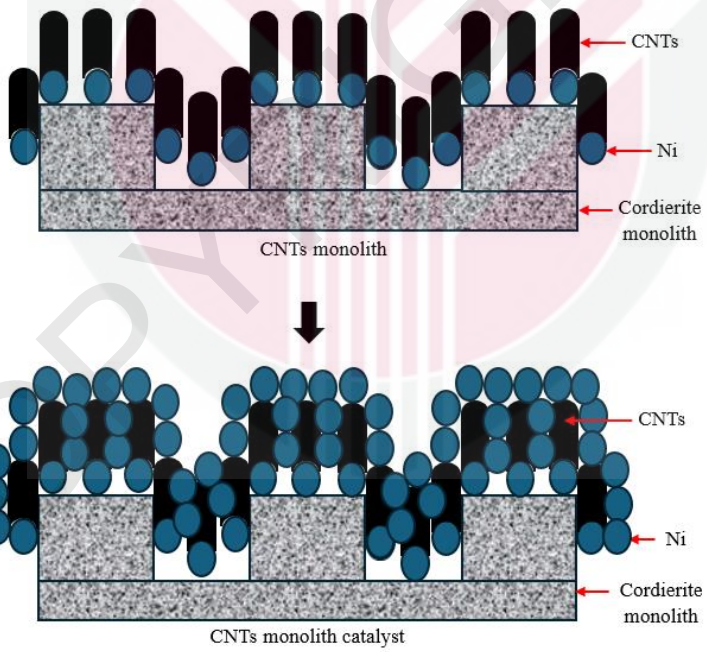

Figure 4.14 : The illustration of CNTs monolith and CNTs monolith catalyst

However, the Ni catalyst suffered from insufficient low-temperature activity and degradation over time due to oxidation. Thus, the combination of Ni with the second metal (Fe or Co) catalyst can enhance the performance and durability of the catalyst (Frontera et al., 2017; Huynh et al., 2020). This can be achieved by the complex interaction between the two metals, leading to a new high-performing and cost effective catalyst. Tsiotsias et al. (2020) reported that the Fe/(Ni + Fe) ratio of 0.1 was found to successfully provide high metal dispersion, small nanoparticle sizes, and an optimum amount of surface basic sites. The molar ratio between Ni and Fe seems to be the most important factor in determining whether Fe can significantly promote CO_2 methanation performance.

Based on these studies, only the best monometallic performance analyzed by Taguchi method design was selected to produce bimetallic catalyst. This bimetallic was applying two types of metal: Ni (as the first metal) and Fe or Co (as the second metal catalyst). The bimetallic catalyst was investigated at 1 wt.% of M (M= Fe or Co) with 10 wt.% Ni on the CNT monolith surface. Moreover, the reason of not chosen the higher Ni loading (25 wt.%) due to the formation of larger Ni particles at higher loadings, which can lead to a decrease in the number of active sites for catalytic reactions (Wang et al., 2021). Additionally, higher Ni loadings can lead to sintering of the Ni particles, reducing the surface area and catalytic activity of the catalyst (Zhao et al., 2023).

The characterization of CNT monolith catalysts is conducted to describe their catalytic performances. The characterization measurements are evaluated to analyze the morphology, chemistry, surface, and crystallinity. Figure 4.15 (a), (b), and (c) illustrate the morphology images of all three Ni CNT monoliths included, with a size distribution at 60 points for each catalyst, as shown in Figure 4.15 (d). According to the image illustrated in Figure 4.15 (a) and the size distribution, a 1 wt.% Ni CNT monolith catalyst still shows the presence of CNT shapes coated with Ni metals, which contributes to the average size of 35.889 nm. The average size is not too different from the CNT monolith. The maximum size range of a 1 wt.% Ni CNT monolith catalyst is quite similar to that of a CNT monolith, which is between 30 and 35 nm. Moreover, the 10 wt.% Ni CNT monolith catalyst exhibits the smallest size distribution, with an average size of about 23.965 nm within the range of 22 to 24 nm compared to 1 wt.% and 25 wt.% Ni CNT monolith catalysts, as shown in Figure 4.15 (b). The 25 wt.% Ni CNT monolith micrograph images in Figure 4.15 (c) presents the highest size distribution, with an average of 87.041 nm within the highest range between 60 and 80 nm. For an overview, the size distribution of 1 wt.%, 10 wt.%, and 25 wt.% Ni CNT monolith catalysts starts from 20 to 63 nm, 14 to 40 nm, and 40 to 180 nm, respectively.

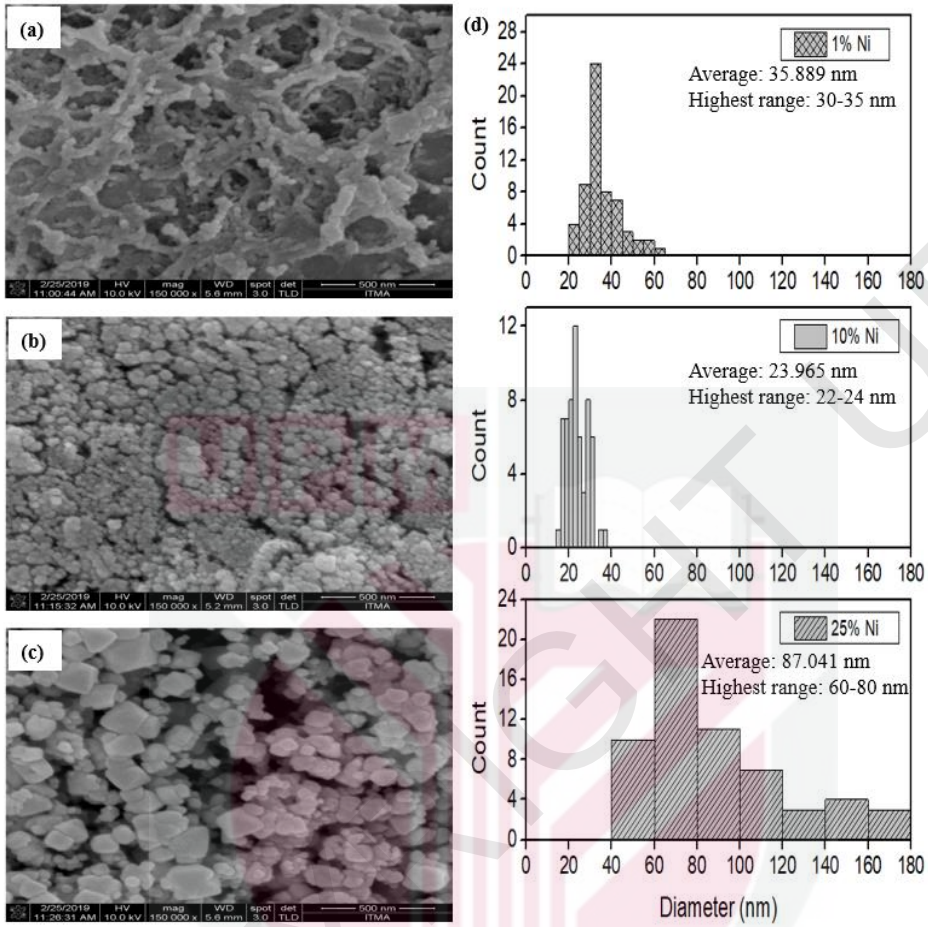

Figure 4.15 : Micrograph image and size distribution of single metallic CNT monolith catalyst with (a) 1 wt.% Ni; (b) 10 wt.%; (c) 25 wt.% using FESEM at 150 000 magnifications; and size distribution of 1wt.%, 10 wt.% and 25 wt.%

The agglomeration of Ni particles was attributed to the varying loadings of Ni onto the support surface, as determined by Zhang et al. (2019a). As illustrated in Figure 4.15, the agglomeration and loading of Ni particles increased significantly, leading to the production of large Ni particles because of the restricted strength of contacts with the support. Thus, the excess Ni particles stacked upon one another, resulting in the formation of large particles, as seen in Figure 4.15 (c) by the 25 wt.% Ni loading onto the CNT monolith. However, when 10 wt.% Ni is loaded onto a CNT monolith, the Ni particles are smaller than at the other two Ni loadings, as the interaction between the Ni and CNT supports is favorable, allowing the Ni particles to agglomerate efficiently onto the CNT support. The Ni loading of less than 20 percent led to an increase in the catalyst's mean pore radius. This suggests that the Ni particles not only

filled the pores but also collected in the peripheries, causing the pores to enlarge and potentially form new pores (Zhang et al., 2019a).

The role of metal catalyst loading is an important factor in initiating a strong interaction with the support and demonstrating better metal catalyst dispersion on the support. Therefore, bimetallic CNT monolith catalysts are particularly attractive due to their unusual catalytic properties compared to other components, such as being highly dispersed and having increased stability (Guczi et al., 2010; Z. Zhao et al., 2019). The bimetallic was prepared based on a ratio of 1:10 wt.% between the second metal (Co or Fe) and Ni metal, labelled as 1 wt.% Co/10 wt.% Ni (1Co/10Ni) or 1 wt.% Fe/10 wt.% Ni (1Fe/10Ni) CNT monolith catalysts. Figure 4.16 described the micrograph image of the Ni dispersion onto CNT monolith surface and proceed to monometallic and bimetallic catalyst.

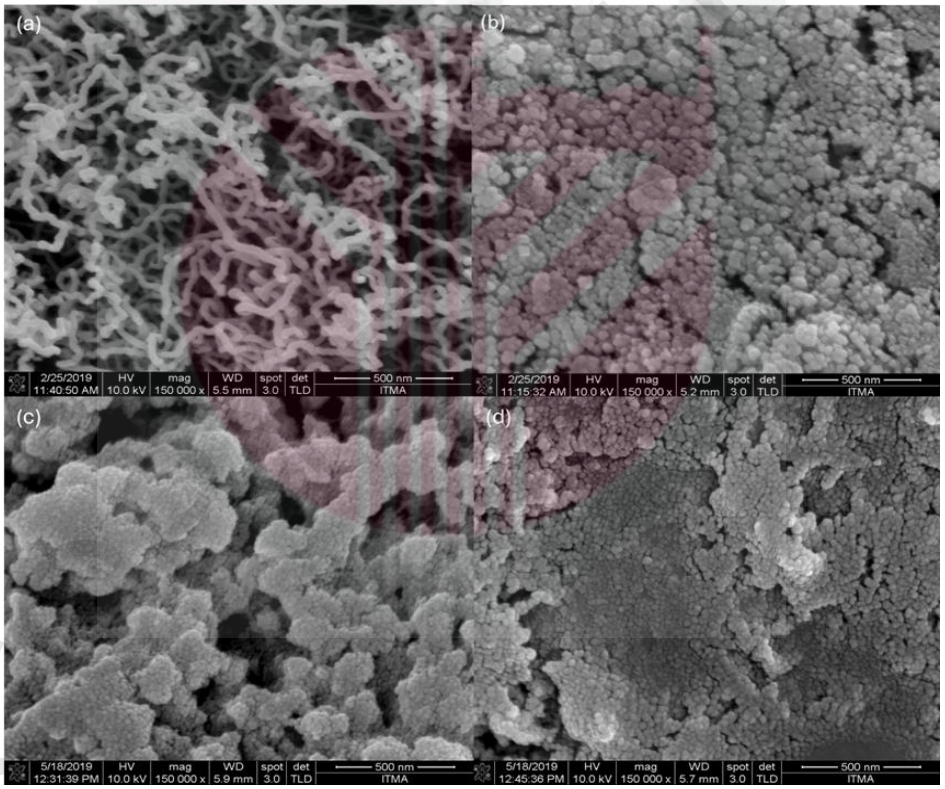

Figure 4.16 : Micrograph image of CNT monolith catalyst from various run which (a) CNT monolith, (b) 10 wt.% Ni CNT monolith, (c) 1/10 wt.% Fe/Ni monolith and (d) 1/10 wt.% Co/Ni monolith

The chemical analysis of mono and bimetallic CNT monolith catalysts is conducted using the FTIR and EDX spectra. The FTIR spectrum of mono- and bimetallic CNTs monolith catalysts are demonstrated within 4000–650 cm^{-1} regions shown in Figure 4.17. All the CNT monolith catalysts exhibited an intense peak compared to the CNT monolith. A broad band from the spectrum illustrated in the region of 3537–3450 cm^{-1} for monometallic and bimetallic CNT catalysts refers to the hydroxyl group (O-H) from intermolecular hydrogen-bonded stretching that is ascribed to the oscillation of a water molecule and bound on the surface of the CNT monolith (Saravanakkumar et al., 2018). The decrease in peak intensity indicates a decrease in the hydrophilicity of CNT monolith catalysts (Ouhaddouch et al., 2019). The region wavelength at 3000–2840 cm^{-1} refers to C-H stretching which is assigned to sp^3 carbon hybridization (alkane; -C-H) observed the strong, intense peaks at 2921 cm^{-1} and 2852 cm^{-1} in 10 wt.% Ni and 1/10 wt.% of Fe/Ni CNTs monolith catalyst spectrum.

The peak at 2315 cm^{-1} corresponds to the alcohol feature attributes of O-H stretching from the H-bond of carboxyl. The observed peak in the range of 1800 to 1700 cm^{-1} denotes the formation of the C=O bond stretching vibration mode with C=C overlapped due to carbon oxidation. This suggests the carboxylation on the CNTs' surfaces and consequently, the peak intensity increases the number of carboxyl groups. Thus, it showed a confirmation of the CNT functionalisation of the surface due to the COOH-COOH material (Ţucureanu et al., 2016). The hexagonal structure of CNTs is presented by 1580–1530 cm^{-1} (originating from the sp^2 hybridised carbon) and 1200–1100 cm^{-1} (originating from CNTs' disordered regions consisting of the disordered sp^3 carbon, which served as nucleation sites for hydrogen), which are assigned to the C=C bond from CNTs' skeletal vibration mode. The O-O vibration mode of the carboxyl group is observed in the range of 1400–1000 cm^{-1}, demonstrating bicarbonate (HCO_3) stretching on CNTs. The peak observed at <1100 cm^{-1} denotes the formation of metal oxide (Hussain et al., 2017). The peak intensity of combination Ni-Co can be distinguished at 680 cm^{-1} (Vidhya et al., 2020) while Ni-Fe at 720 cm-1 (Nguyen et al., 2018). These combination Ni-Co and Ni-Fe can describe the interaction between the atoms. The peaks showed a significant interaction between Ni and Co which related to metal-oxygen bonds that might be experience shifting due to the change in the coordination environmental of the metal atoms. An overview of the FTIR spectrum for mono and bimetallic CNTs monolith catalysts is tabulated in Table 4.6.

Table 4.6 : Different functional groups for the fresh CNTs monolith catalyst

Functional group	CNTs	1 wt.% Ni	10 wt.% Ni	25 wt.% Ni	1/10 wt.% Fe/Ni	1/10 wt.% Co/Ni	References
free hydroxyl groups	3744	-	-	-	-	-	(Atieh et al., 2010; Azri et al., 2017)
O-H stretch from O=C-OH & C-OH	3419	3472	3472	3537	3450	3521	(Saravanakkumar et al., 2018)
C-H	-	3015	2926	-	2920	-	(Ţucureanu et al., 2016)
O-H stretch from -COOH	2321	2308	2317	2316	2306	2317	(Atieh et al., 2010)
C=O-O-H	1637						(Ma et al., 2016)
C=O carboxyl group		1742	1742	1742	1754	1750	(Ţucureanu et al., 2016)
C=C	1543	1571	1574	1574	-	1573	(Baykal et al., 2013)
C=C aromatic	-	1368	1368	1369	1368	1369	(Osman et al., 2020)
C-C	-	-	1189	1181	1180	1182	(Baykal et al., 2013)
Ni-O-Ni	-	957	957	956	957	956	(Gupta & Saleh, 2011; Hussain et al., 2017)
C-H stretching	893	-	-	-	-	-	(Mansor et al., 2012)
metal oxide bond stretching	793	772	772	772	680	682	(Gupta & Saleh, 2011; Hussain et al., 2017)

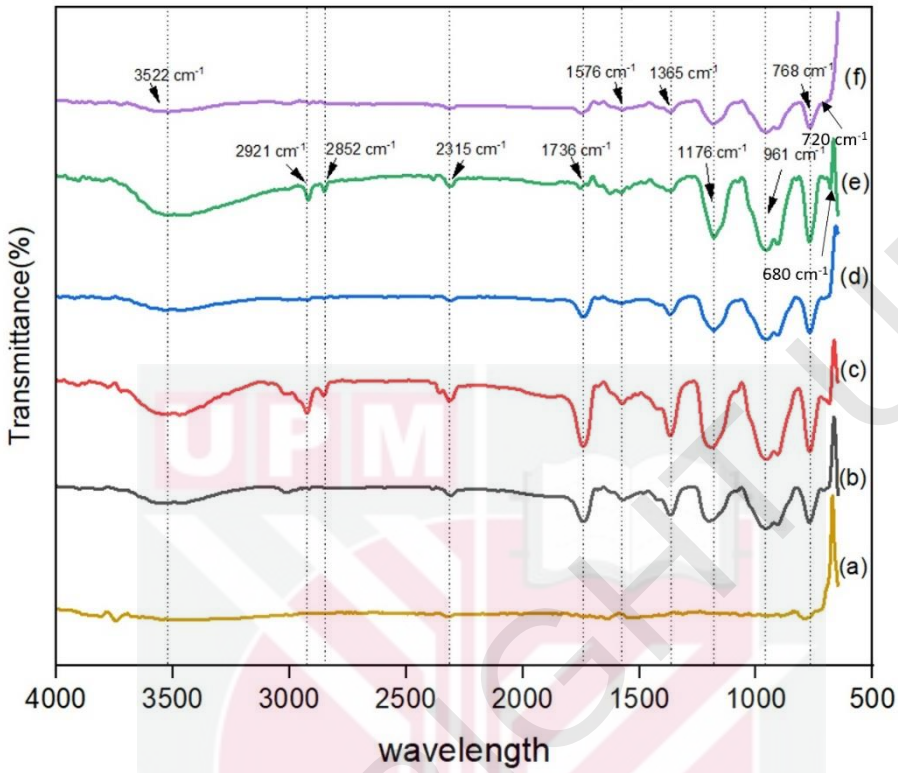

Figure 4.17 : FTIR analysis of (a) CNTs monolith, monometallic CNTs monolith catalyst (b) 1 wt.% Ni, (c) 10 wt.% Ni, (d) 25 wt.% Ni; bimetallic CNTs monolith catalyst (e) 1/10 wt.% Fe/Ni, (f) 1/10 wt.% Co/Ni

Table 4.7 describes the EDX spectrum for monometallic and bimetallic CNT monolith catalysts. As described by the atomic composition of monometallic CNT monolith catalysts, the composition of Ni in 1 wt.%, 10 wt.%, and 25 wt.% Ni CNT monolith catalysts deviated only ~5% increment from the prepared composition, while 1 wt.% CNT monolith catalyst had a small deviation of almost ~0.29% decrement. Both types of catalyst undergo for calcination showed the percentage of oxygen higher as the reaction producing nickel oxide, NiO. Moreover, the atomic composition of bimetallic showed quite different behaviour between the two types of the second metal, which were Co and Fe. The 1/10 wt.% Co/Ni CNT monolith catalyst evaluates quite close to the prepared composition of the catalyst. Meanwhile, the composition of the Mg, Al and Si were the composition of the originally from cordierite monolith. The preparation and calculation are shown in Appendix A1.

Table 4.7 : Atomic composition of monometallic and bimetallic CNTs monolith catalyst from the EDX spectrum.

Catalyst	Ni* (%)	Fe/ Co	C (%)	O (%)	Mg (%)	Al (%)	Si (%)	Ni (%)	Co (%)	Fe (%)
monolith	-	-	24.9	42.4	5.7	12.2	14.8	-	-	-
CNTs	-	-	96.5	2.3	0.2	0.5	0.6	0.00	0.00	0.00
1Ni	1	-	2.9	63	6.0	11.7	15.7	0.71	0.00	0.00
10Ni	10	-	2.9	54.5	5.3	10.2	13.0	14.1	0.00	0.00
25Ni	25	-	3.3	50.0	3.5	6.6	8.2	28.4	0.00	0.00
Co/Ni	10	1	0	48.8	6.7	13.2	19.3	9.3	2.7	0.00
Fe/Ni	10	1	0	53.9	1.2	2.7	3.8	11.3	0.00	2.2

*Theoritical

The TPD-CO_2 profile showed the strength and amount of the basic surface sites on the CNT monolith catalysts based on the CO_2 absorption desorption process as shown in Figure 4.18. The profiles correspond to different surface oxygen groups, and the amount of CO_2 desorbed can be correlated with the total number of surface oxygen groups. In general, CO_2 results from carboxylic acids at low temperatures, or lactones at higher temperatures. The carboxylic acids decompose as CO_2 below 400 °C and the carboxylic anhydrides which consists of two carbonyl groups connected by a single oxygen atom decompose between 350 and 600 °C by releasing one CO and one CO_2 molecule (Calo et al., 1997; Rocha et al., 2023).

Additionally, the presence of cyclic esters is called lactones revealed by the release of CO_2 above 600 °C while phenol groups observed by the release of CO in a middle temperature range (500–750 °C). The results described the surface is functionalized with carboxylic acid groups as also provided in FTIR analysis and the adsorbed water molecules released at a lower temperature compared to a surface without these groups due to carboxylic acid groups form stronger hydrogen bonds with water molecules than functionalized surfaces. The 1 wt.% Ni, 25 wt.% Ni and 1/10 Fe/Ni wt.% catalyst showed a significant increase compared to CNT monolith which described the carboxylic anhydride decomposed between 350 and 500 °C except for 10 wt.% Ni and 1/10 Co/Ni wt.% catalyst. Moreover, the increment that showed the presence of carbonyl groups decomposed between 500 and 750 °C for all types of catalyst.

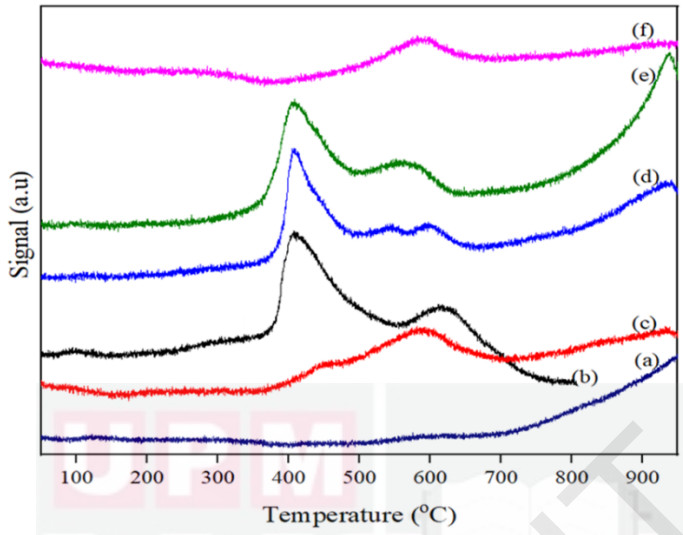

Figure 4.18 : TPD-CO_2 profile of fresh catalysts (a) CNTs, (b) 1 wt.% Ni, (c) 10 wt.% Ni, (d) 25 wt.% Ni, (e) 1/10 wt. % Fe/Ni and (f) 1/10 wt.% Co/Ni CNTs monolith catalyst.

The basic sites over the catalyst are shown by the number of exposed active sites per unit mass for CO_2 absorption analyzed from Figure 4.18 and listed in Table 4.8. The temperature of desorption exposes the strength (weak, medium, and strong basic strength), and the maximum desorbed CO_2 determines the number of basic site records. The CNTs monolith obviously showed a broad peak at high temperature while the peak area of medium sites becomes smaller and shift towards higher temperature ranges. All the catalyst showed two desorption peaks of medium basic sites and strong basic sites except for 10 wt.% Ni and 1/10 Co/Ni wt.% catalyst that only have one peak.

Table 4.8 : The number of active sites of the catalyst

Catalysts	Medium sites (mmol/g)	Strong sites (mmol/g)	Total basic sites (mmol/g)
CNTs	0	0	0
1 wt.% Ni	0.0825	0.0475	0.1300
10 wt.% Ni	0.1198	0.0608	0.1806
25 wt.% Ni	0.0770	0.0952	0.1723
1/10 wt. % Co/Ni	0.0687	0	0.0687
1/10 wt.% Fe/Ni	0.0435	0.0950	0.1385

The TPR-H_2 has been applied to provide information about the reduction behavior of the catalyst, particularly the reduction of metal oxide species. Typically, the profiles showed the extend of H_2 consumption TPR runs of all catalysts exposed indicate the amount of H_2 consumption, as a function of temperature, correspond the redox properties of the catalyst as shown in Figure 4.19. The temperature of maximum reduction is carried out between 300 and 450 °C and the H_2 consumption is reproducible within 49.20 to 59.05 µmol/g. This peak was assigned to the reduction of surface oxygen in CNTs and NiO, which have weak interactions with CNT monolith supports (Frontera et al., 2017; Wang et al., 2016). In establishing the calibration curve, both mono and bimetallic CNTs catalyst was assumed that the metal catalyst (Ni, Co, and Fe) completely reduced.

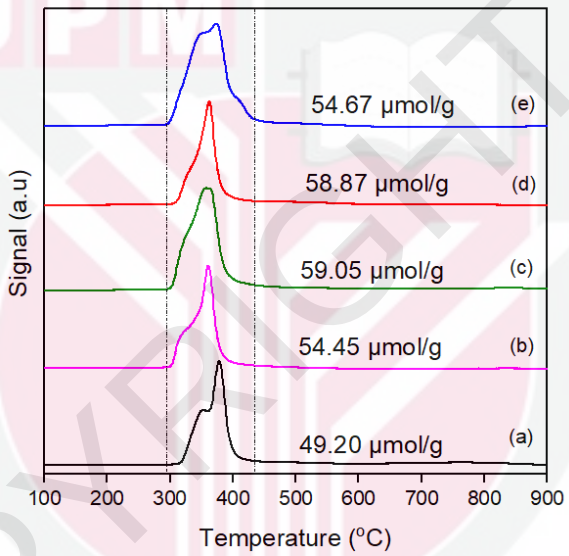

Figure 4.19 : TPR-H_2 profiles of (a) 1 wt.% Ni, (b) 10 wt.% Ni, (c) 25 wt.% Ni, (d) 1/10 wt. % Co/Ni and (e) 1/10 wt.% Fe/Ni CNTs monolith catalyst.

The surface area of a catalyst is related to adsorption, which significantly affects the catalytic activity. The nitrogen adsorption/desorption isotherm branch in Figure 4.20 presents the mono and bimetallic CNT monolith catalyst samples. Like the CNT monolith, the catalyst also exhibits type III isotherm accompanied by hysteresis H3, indicating the presence of mesoporous structure. The relative pressure range of all catalysts display is $0.8 < P/P_o < 1$. As tabulated in Table 4.9, the BET surface areas of 1 wt.% Ni CNTs, 10 wt.% Ni CNTs, 25 wt.% Ni CNTs, 1/10 wt.% Fe/Ni-CNTs, and 1/10 wt.% Co/Ni-CNT were reduced by 80.5%, 93.0%, 80.3%, 79.0%, and 99.0% respectively. This is due to the impregnation process in which the metal catalyst (Ni or M) is dispersed onto the CNT monolith's surface area.

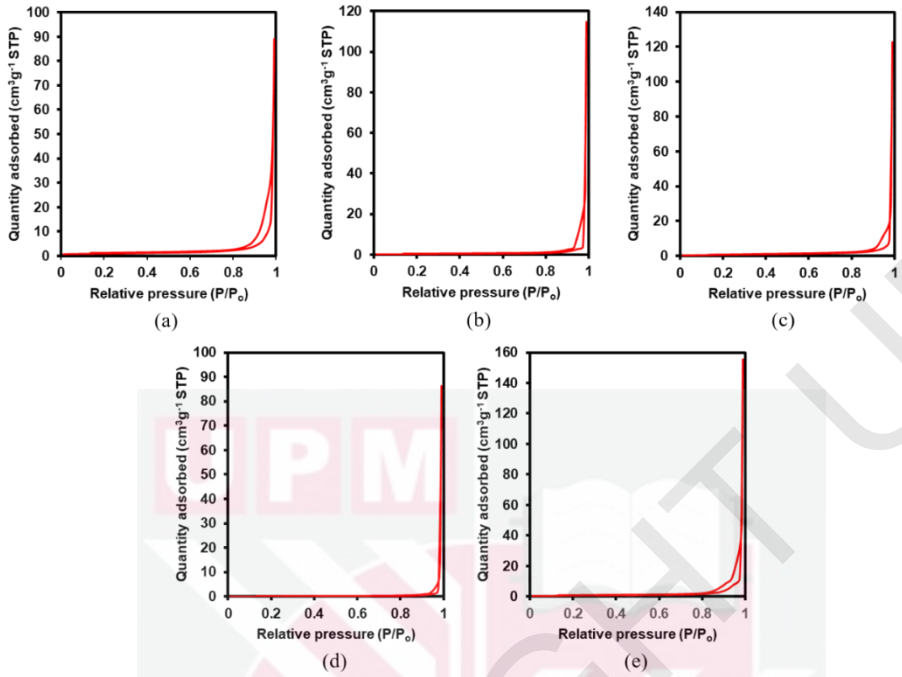

Figure 4.20 : Nitrogen adsorption-desorption isotherms of single metallic CNTs monolith catalyst (a) 1 wt.% Ni CNTs; (b) 10 wt.% Ni CNTs; (c) 25 wt.% Ni CNTs; and bimetallic CNTs monolith catalyst (d) 1/10 wt.% Fe/Ni-CNT; (e) 1/10 wt.% Co/Ni-CNT

Table 4.9 : The surface analysis of mono and bimetallic CNTs monolith catalysts

Types	[a]BET surface area (m^2/g)	[b]Pore volume (cm^3/g)	Pore size (nm)
1% Ni-CNT	2.9485	0.1289	17.489
10% Ni-CNT	1.0298	0.1523	29.578
25% Ni-CNT	2.9777	0.1660	11.150
1/10 wt.% Fe/Ni-CNT	3.1716	0.2057	12.973
1/10 wt.% Co/Ni-CNT	0.1387	0.1228	17.710

a calculated by BET equation
b BJH desorption pore volume

Figure 4.21 represents the X-ray diffraction (XRD) patterns of mono and bimetallic CNT monolith catalysts. The peak of NiO patterns reflected at 2θ = 37.24°, 43.30°, and 62.70° shows a significant increment of reflected peaks due to the addition of Ni loading. Furthermore, these peaks became weaker in the bimetallic catalysts than those observed in monometallic catalysts. This

could be due to the higher dispersion of Ni in the bimetallic catalyst (Rahmani et al., 2019). The peak patterns of Co/Ni CNT monolith catalysts show the peak at 2θ = 32.29° according to cobalt oxide (ICDD file No. 00-001-1020), while the Fe/Ni CNTs monolith catalyst reflected at 2θ = 35.74° indicates Fe_2O_3 (ICDD file No. 00-001-1053).

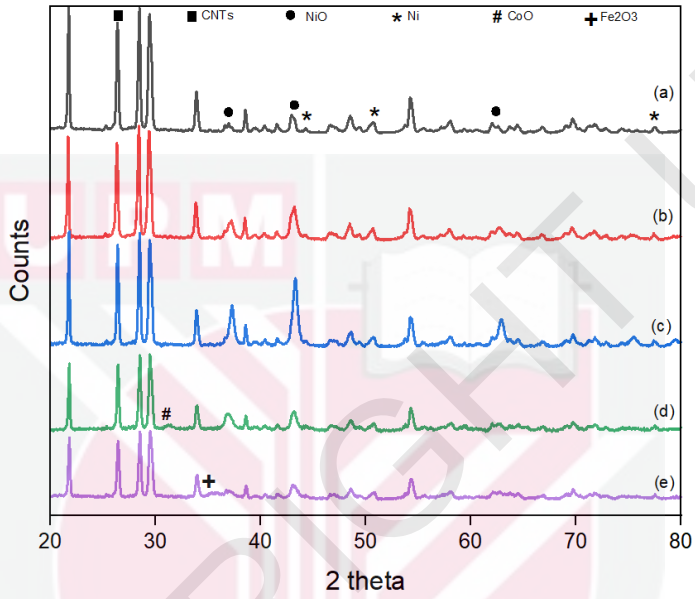

Figure 4.21 : XRD pattern of mono (a) 1 wt.% Ni CNTs; (b) 10 wt.% Ni CNTs; (c) 25 wt.% Ni CNTs; and bimetallic CNTs monolith catalyst (d) 1/10 wt.% Co/Ni-CNT; (e) 1/10 wt.% Fe/Ni-CNT

4.4 Carbon dioxide methanation

The catalytic activity of CO_2 methanation has employed CNT monolith catalysts. The investigation focuses on the catalyst's reaction performance in terms of its highest CH_4 selectivity and lowest CO selectivity. The performances of the CO_2 methanation have been measured using Equations 3.6 - 3.8. As the data was collected from the GC, the amount of gases produced from the reaction was converted based on the calibration factor from the calibration curves. The correct calibration curves were supposed to be plotted from at least three different points of concentration to get the perfect factor for measurement. However, one-data calibration curves were given which possibly affected the measurement of the catalytic activity. The calibration curves for CO_2, H_2, CH_4 and CO can be found in Appendix B1. The optimum condition for the reaction was determined based on the Taguchi method design. The CO_2 conversion was obtained based on Equation 3.6 as

reported by Vrijburg et al. (2019) CO_2 conversion based on moles of CO_2 consumed over moles of CO_2 inlet was unable to use. However, a sample calculation is presented in Appendix B2 using the gas composition obtained from the mix gas containing CO_2 and H_2 operated at room temperature with no catalyst being added. The gas composition could be considered as the inlet reactant since no reaction occurred based on no additional gas composition being observed.

4.4.1 Analysis of optimization of CO_2 methanation based on Taguchi method

The ANOVA of the CO_2 methanation by monometallic CNTs monolith catalysts based on the Taguchi optimisation method was designed by Design Expert 7. The targets of the design are CO_2 conversion, CH_4 selectivity and CO selectivity as tabulated in Figure 4.22. In the design all the targets are responded to via the S/N ratio as tabulated in Table 4.10. The 'larger-is-better' S/N ratio is expressed for CO_2 conversion and CH_4 selectivity, considering the highest conversion of CO_2 and the highest selectivity of CH_4. Meanwhile, the 'smaller-is-better' S/N ratio is expressed as the selectivity of CO due to the lower concentration of CO.

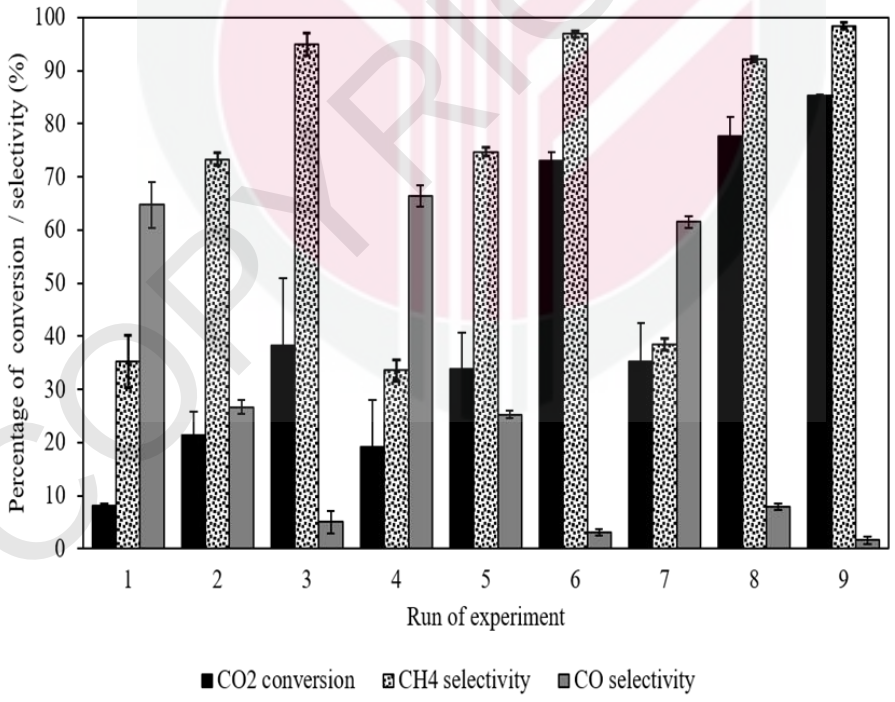

Figure 4.22 : The CO_2 conversion, CH_4 selectivity and CO selectivity with their standard error for each run of experiment.

Table 4.10 : Experimentally measured values for CO_2 conversion, CH_4 selectivity and CO selectivity from methanation reaction and signal-to-noise (S/N) ratio (Taguchi orthogonal array table of L_9 (3^4)).

	Reaction temperature (°C)	Nickel loading (wt.%)	Flowrate (mL/min)	CO_2 conversion			CH_4 selectivity			CO selectivity		
Run	A	B	C	Average (%)	Standard error	*S/N ratio (dB)	Average (%)	Standard error	*S/N ratio (dB)	Average (%)	Standard error	**S/N ratio (dB)
1	300	1	30	8.18	0.25	1.877	35.27	4.93	3.095	64.72	4.29	-38.221
2	300	10	50	21.40	4.33	2.661	73.34	1.30	3.731	26.66	1.30	-28.519
3	300	25	100	38.22	12.78	3.164	94.96	2.14	3.955	5.04	2.14	-14.057
4	350	1	50	19.14	8.82	2.564	33.59	2.00	3.052	66.41	2.00	-36.445
5	350	10	100	33.88	6.79	3.060	74.72	0.78	3.747	25.28	0.78	-28.054
6	350	25	30	73.03	1.67	3.727	96.93	0.63	3.973	3.07	0.63	-9.750
7	400	1	100	35.27	7.25	3.095	38.47	1.08	3.170	61.53	1.08	-35.781
8	400	10	30	77.70	3.67	3.781	92.14	0.57	3.929	7.86	0.57	-17.913
9	400	25	50	85.36	0.25	3.863	98.42	0.64	3.986	1.58	0.64	-3.990

*Larger is better
**Smaller is better

The significance of the top five average percentages of CO_2 conversion is exhibited by the experimental runs of 9, 8, 6, 3 and 7, respectively. Runs 9 and 8 which operated at 400 °C reaction temperature are the two highest of the top five runs. Runs 6 and 3 which were conducted at 350 °C and 300 °C respectively using 25 wt.% Ni loading came in the third and fourth places. Thus, the first analysis indicates that the CO_2 methanation reaction at 400 °C with higher Ni loading could reach a higher conversion of CO_2. Otherwise, the highest CH_4 selectivity and the lowest CO selectivity are demonstrated in a similar top-five sequence as runs 9, 6, 3, 8 and 5 in decreasing order. The analysis of this response shows that Ni loading is a significant parameter as runs 9, 6 and 3 presented the highest CH_4 selectivity and the lowest CO selectivity by 25 wt.% Ni loading, which were conducted at 400 °C, 350 °C and 300 °C respectively. Both runs 8 and 5 are presented as the fourth and fifth places and are contributed by 10 wt.% of Ni loading. The mixed gas flow rates of 30 and 50 mL/min, on the other hand, produced the top two highest results in CO_2 conversion, CH_4 selectivity, and the two lowest CO selectivity.

4.4.2 Response and Variance Analysis

The Taguchi method for optimisation studies of CO_2 methanation reaction is intended to assist in data analysis and predict the optimum conditions based on three responses. As shown in Table 4.11, the analysis of parameter ranking represents the importance of each parameter to the CO_2 methanation reaction. The ranking is determined by the delta value, which is calculated from the difference between the highest and lowest average S/N ratios for each parameter level as shown in Appendix A. The ranking showed that the Ni loading is the most important parameter, followed by reaction temperature, and mixed gas flowrate, as all of the experiment's responses rank similarly. The increase in Ni loading contributes to higher CO_2 conversion, CH_4 selectivity and CO selectivity (Daroughegi et al., 2017; Jaffar et al., 2019; Rahmani et al., 2014; Zhen et al., 2015). The increase in Ni loading could increase the Ni size particle, which would reduce the uniform dispersion of NiO particles and increase the nonuniform dispersion of Ni particles on the support. Moreover, the increased Ni content shows that the crystalline structure of the Ni catalyst is strongly dependent on the Ni on the support. However, Zhen et al. (2015) discovered that increasing catalytic activity was only associated with increasing the Ni loading by 5-10 wt.%. While the higher >10 wt.% exhibit the segregation of metallic nickel particle, resulting in diminished catalytic activity. Therefore, the reaction conditions which are expected to give the highest CO_2 conversion, the highest CH_4 selectivity and the lowest CO selectivity are $A_3B_3C_3$, $A_3B_3C_3$ and $A_1B_1C_1$ respectively. The one plot factor in Figure 4.23 illustrates the B model in all three responses, while Figure 4.24 presents the A model only for two responses, CO_2 conversion and CO selectivity. The red circle in the diagram showed the design point for each model to achieve required responses.

Table 4.11 : The response table of S/N ratios at different factor levels

Level of parameter		1	2	3	*Delta	*Rank
Average S/N ratio at each level						
Response 1: CO_2 conversion						
Reaction temperature °C	A	2.5674	3.1171	3.5794	1.0120	2
Nickel loading (wt.%)	B	3.5935	3.5907	3.6951	0.1044	1
Flowrate (mL/min)	C	-26.932	-24.750	-19.228	7.7041	3
Response 2: CH_4 selectivity						
Reaction temperature °C	A	2.5120	3.1672	3.5848	1.0728	2
Nickel loading (wt.%)	B	3.1059	3.8021	3.9713	0.8655	1
Flowrate (mL/min)	C	-36.816	-24.828	-9.2655	27.5500	3
Response 3: CO selectivity						
Reaction temperature °C	A	3.1282	3.0292	3.1065	0.0990	2
Nickel loading (wt.%)	B	3.6656	3.5897	3.6241	0.0759	1
Flowrate (mL/min)	C	-21.961	-22.984	-25.964	1.0029	3

*All the values are calculated as shown in Appendix

As mentioned in the Section 4.3.2, the variance analysis for the CO_2 methanation reaction can be evaluated by the sum of squares (SS) and adjusted mean squares as tabulated in Table 4.12. All the responses are considered in determining the optimum conditions for the CO_2 methanation reaction using Ni CNT monolith catalysts. The larger percentage contribution to the total sum of squares calculated by Equation 3.8 in Section 3.7 could influence the S/N ratio of each parameter.

The model F-value of 26.50 implies the model is significant for response 1. The model F-values of responses 2 and 3 are 118.97 and 26.64 respectively, indicating that both models are significant. The model F-value of response 1 shows only 0.39%, while both responses 2 and 3 present 0.01% that could occur due to noise. The P-values of all responses less than 0.0500 indicate model terms are significant. In this case, A and B are significant model terms. The values greater than 0.1000 indicate the model terms are not significant. The Predicted R^2 for response 1 of 0.8159 is in reasonable agreement with the Adjusted R^2 of 0.9273. The Predicted R^2 of response 2 is 0.9447, which is reasonable with the Adjusted R^2 of 0.9672. The response 3 exhibits that the Predicted R^2 of 0.8302 agrees with the Adjusted R^2 0.9329. Adeq Precision

measures the signal-to-noise ratio. A ratio greater than 4 is desirable. The ratios of 15.866, 20.850 and 14.251 indicate an adequate signal for each model from all the responses. This model can be used to navigate the design space.

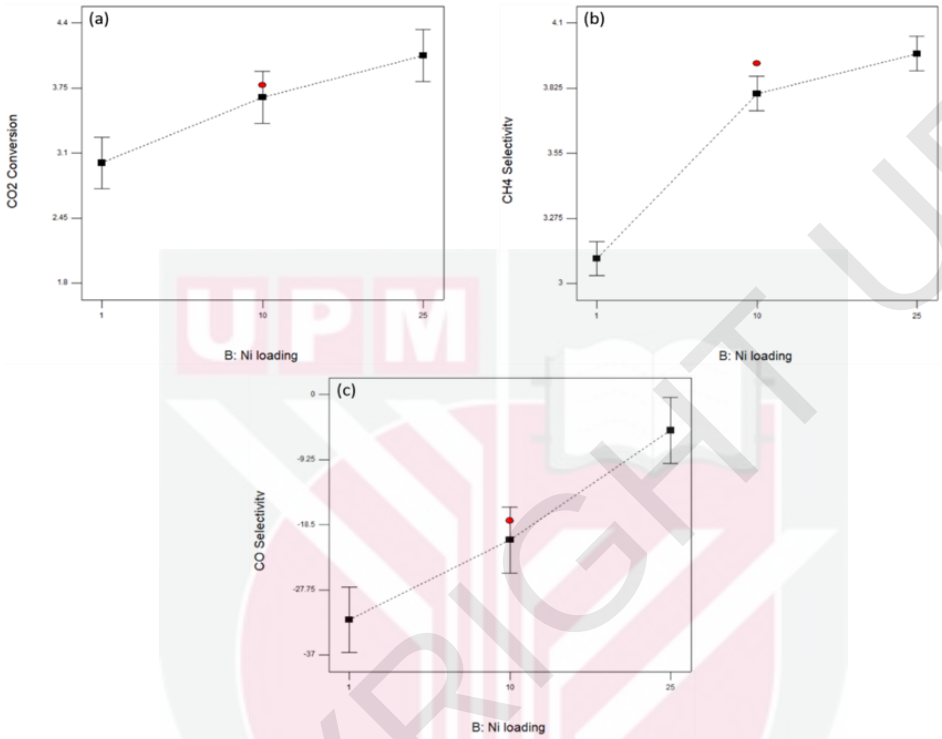

Figure 4.23 : One plot factor of the main effect Ni loading for (a) CO_2 conversion; (b) CH_4 selectivity and (c) CO selectivity.

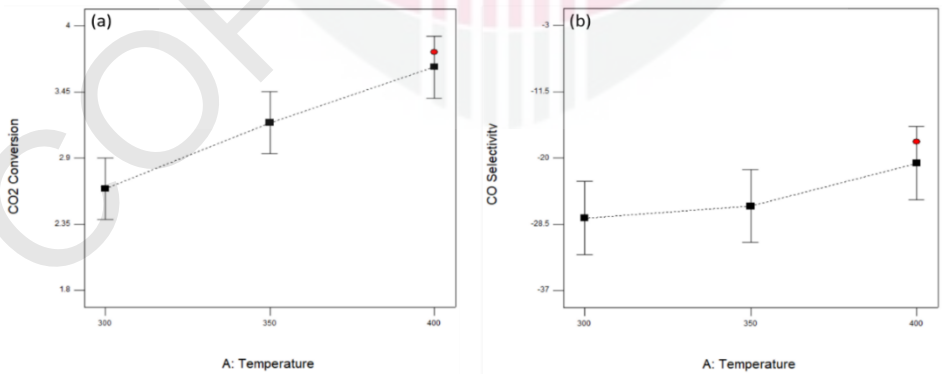

Figure 4.24 : One plot factor of the main effect temperature for (a) CO_2 conversion and (b) CO selectivity

Table 4.12 : Summary of ANOVA for selected factorial model of all responses.

	Degree of Freedom (DF)	Sum of Squares (SS)	Adjusted Mean Square (Adj. SS)	Percentage Contribution (%)	F-Value	p-Value Prob > F
Response 1: CO_2 conversion						
A	2	1.54	0.77	46.44	24.78	0.0056
B	2	1.75	0.88	53.07	28.23	0.0044
C	2	0.02	0.00812	0.49		
Model (A & B)	4	3.29	0.82		26.50	0.0039
Total (A,B,C)	6			100.00		
R-Squared		0.9636 (significant)				
Adj. R-Squared		0.9273				
Pred-R-Squared		0.8159				
Adeq Precision		15.8661				
Std. Dev.		0.1763				
Response 2: CH_4 selectivity						
A	2	0.021	0.011	1.7046		
B	2	1.26	0.63	97.6257	118.97	<0.0001
C	2	0.864	0.00432	0.6697		
Model (B)	4	1.26	0.63		118.97	<0.0001
Total (A,B,C)	6			100.00		
R-Squared		0.9754 (significant)				
Adj. R-Squared		0.9672				
Pred-R-Squared		0.9447				
Adeq Precision		20.5800				
Std. Dev.		0.073				
Response 3: CO selectivity						
A	2	82.31	41.15	6.8077	4.04	0.1098
B	2	1093.07	546.54	90.4179	53.59	0.0013
C	2	33.54	16.77	2.7744		
Model (A & B)	4	1175.38	293.85		28.81	0.0033
Total (A,B,C)	6			100.00		
R-Squared		0.9665 (significant)				
Adj. R-Squared		0.9329				
Pred-R-Squared		0.8302				
Adeq Precision		14.251				
Std. Dev.		3.19				

4.4.3 Confirmation Test at Optimum Conditions

Based on the Taguchi study, the optimum condition suggested for CO_2 methanation is $A_3B_2C_1$. Therefore, the experiment was conducted under optimum conditions and repeated three times to achieve consistency. The expected results of the predicted optimum condition should be 67.50%, 79.63%, and 10.77% compared to the actual results of 76.09%, 93.43% and 6.31% of CO_2 conversion, CH_4 and CO selectivity respectively, as tabulated in Table 4.13. The actual results showed the increments of CO_2 conversion and CH_4 selectivity by 8.59% and 13.8% respectively. The CO conversion could decrease by 4.46% at the suggested optimum conditions.

Table 4.13 : The optimal configuration with predicted and actual S/N ratio value

Run	Parameter			Optimization Prediction			Optimization Results		
				S/N Ratio Predicted			S/N Ratio Actual		
				CO_2	CH_4	CO	CO_2	CH_4	CO
	A	B	C	dB	dB	dB	dB	dB	dB
1	400	10	30	3.66	3.80	-20.64	3.76	3.96	-12.61
2	400	10	30	3.66	3.80	-20.64	3.79	3.94	-16.86
3	400	10	30	3.66	3.80	-20.64	3.74	3.92	-18.52
Average				3.66	3.80	-20.64	3.76	3.94	-16.00
Standard error							0.02	0.01	1.76

4.4.4 Characterization of spent CNTs monolith catalyst

All the CNTs monolith catalysts were tested in the CO_2 methanation reaction and showed excellent performance in CO_2 conversion and CH_4 selectivity. Both spent monometallic and bimetallic were conducted for characterisation to analyse the condition of the catalyst after the catalytic activity. The characterisation of spent catalysts is focused on chemical and physical properties.

The atomic composition of spent catalyst tabulates in Table 4.14. The findings indicate that the deposition trend of elementary carbons on the surface of mono and bimetallic catalyst is significantly very low (less than 7.00 %) but shows a higher amount on the catalyst surface of 1/10 wt.% Co-Ni CNTs due to an excellent performance in the methanation reaction. This is supported by the spent 1/10 wt.% Fe-Ni/CNT monolith, the spent 25 wt.% Ni/CNT monolith, and the spent 1/10 wt.% Co-Ni CNT monolith. As reported by Feng et al. (2019), this is due to the efficiency of catalysts in the conversion of CO_2 to methane and the production of carbon. The amount of carbon deposited on the surface of the catalyst increased significantly following the catalytic methanation

reaction for all catalyst types except for the monolith composed of 1 wt.% Ni CNTs. The carbon composition of the CNT monolith exhibits a reduction of over 50% in comparison to its initial state.

Table 4.14 : The atomic composition of spent catalyst

Sample Spent catalyst	Atomic composition (% wt)							
	C	O	Mg	Al	Si	Ni	Co	Fe
Bare monolith	2.46	65.11	6.11	11.33	14.99	0	0	0
CNTs monolith	39.27	41.27	3.59	6.88	8.99	0	0	0
1wt% Ni/CNTs monolith	2.6	64.41	6.03	11.39	14.98	0.58	0	0
10wt% Ni/CNTs monolith	3.37	58.95	5.87	11.3	14.68	5.82	0	0
25wt% Ni/CNTs monolith	4.83	23.17	3.36	5.69	6.68	56.27	0	0
1/10wt% Co-Ni CNTs monolith	6.77	31.2	3.89	7.24	9.14	24.27	17.49	0
1/10wt% Fe-Ni/ CNTs monolith	4.24	57.09	2.96	11.16	6.45	3.45	0	14.65
After stability	3.08	62.61	5.66	10.35	13.52	4.78	0	0
Carbon by-product	93.04	6.96	0	0	0	0	0	0

Experimentally, the CNT monolith strongly exhibits the ability to adsorb and activate CO_2 under the reaction conditions. Kwak et al. (2013) reported that a support or a promoter and its interaction with a transition metal are essential for tuning the activity and selectivity of RWGS reactions. This finding is supported by Zhu et al. (2020) who examined the Sabatier reaction mechanism and discovered that it is competed by the RWGS reaction, resulting in a decrease in CH_4 selectivity. The key factor in the development of highly active and selective RWGS depends on the C-O dissociation and hydrogenation abilities provided by the catalyst and CO_2 adsorption in the presence of support or a promoter. Furthermore, Kattel et al. (2016) stated that kinetic Monte Carlo simulations revealed that strong CO_2 adsorption affects CO production, whereas strong CO adsorption produces more CH_4 yields.

However, the metal catalyst of Ni and Co composition exhibits an increasing trend for the spent 25 wt.% Ni/CNT monolith and the spent 1/10 wt.% Co-Ni/CNT monolith, but not for the spent 1 wt.% Ni/CNT monolith. The spent 1/10 wt.% Fe-Ni/CNT shows a vice-versa composition where the composition Ni is decreasing, and Fe is increasing. When compared to their monometallic counterparts, multimetallic nanomaterials can improve catalytic performance. The compositional variations in multimetallic nanomaterials have a direct impact on the electronic state of their constituents. Consequently, the multimetallic catalyst influenced the reactivity, adsorption energies, and geometries of substrate molecules and catalytic behavior. However, the compositional variations can also impact the spatial arrangement and atomic ordering, which leads to significant changes in the properties as a consequence of surface segregation, faceting, diffusion, and others (Rodrigues et al., 2019; Slater et al., 2014).

The FTIR spectra of the spent CNT monolith catalyst (Figure 4.25) were performed in the region 2000–600 cm^{-1} to observe the adsorption species formed on the catalyst surface during CO_2 methanation. The dashed line represents the fresh ones. According to the hypothesis, the heterolytic catalyst activity should depend on the basic sites of the surface. The CO_2 complexes with the oxide surface showed that CO_2 reacts predominantly with O^{2-} and OH^- sites by producing carbonates and bicarbonates, respectively (Davydov, 1995).

The FTIR spectrum at 3743 cm^{-1} can be observed on spent monometallic catalyst to represent the information of O-H groups of bicarbonate stretching on the surface. However, the wide peaks of O-H stretching at 3740–3450 cm^{-1} of 10 wt.% Ni and 1/10 wt.% Fe/Ni fresh catalysts are weakened due to CO_2 desorption (Xie et al., 2021). The typical CO_2 absorption species on the catalyst surface were mainly in the forms of bicarbonates, monodentates, bidentates, and bridged carbonates. The CNT monolith catalyst showed only the signals for the peaks of monodentates (1360–1400 cm^{-1}), bidentates (1560–1640 cm^{-1}), and bridged carbonates (1170–1200 cm^{-1}). According to the literature, the hydrogen carbonates showed signals at 1614, 1405 and 1214 cm^{-1} (Atzori et al., 2021; Daturi et al., 2000). However, the absorption signals for these carbonates contribute weaker hidden signals due to the appearance of bidentate (1640 cm^{-1}) and monodentate carbonates (1543 cm^{-1} and 1369 cm^{-1}) due to the interaction of CO_2 with the basic surface O^{2-} species. The formation of monodentate and bidentate carbonates strictly depended on the basicity of the surface oxygen atoms (Davydov, 1995), as was similar with the TPD-CO_2 results that showed a decreasing amount of weak basic sites and an increase in the amount of medium and strong basic sites. As combined with the TPD-CO_2 results, the strength of basic sites as weak, medium, and strong can be considered as the appearance of bicarbonate, bidentate carbonate, and monodentate carbonate respectively. The existence of monodentate carbonate species becomes more intense in the presence of Ni, as expected from an increase in the concentration of stronger basic sites. The amount of medium and stronger basic sites increased with the increment of Ni content as agreed with TPD-CO_2 results.

The appearance peaks at 2900 cm^{-1} and 3016 cm^{-1} corresponding to C-H bands of formate and C-H stretching of CH_4, respectively. Xie et al. (2021) suggested that H cracked by Ni spilled over onto the C atom, creating an unstable condition that led to the stretching vibration of C-H in monodentate and bridged formate. The disappearance of the peak Ni carbonyl hydride at 1917 cm^{-1} indicated that the formate did not transfer to the surface of metal Ni and that hydrogenation occurred on the surface of the support. The existence of a second metal interacts more with Ni and promotes high dispersion, which enhanced the ability of Ni to crack H and cause it to overflow. Thereby, the acceleration process of H spilling over from Ni to attack the C atom of formate is initiated. Hence, the process increased the activity of CO_2 methanation.

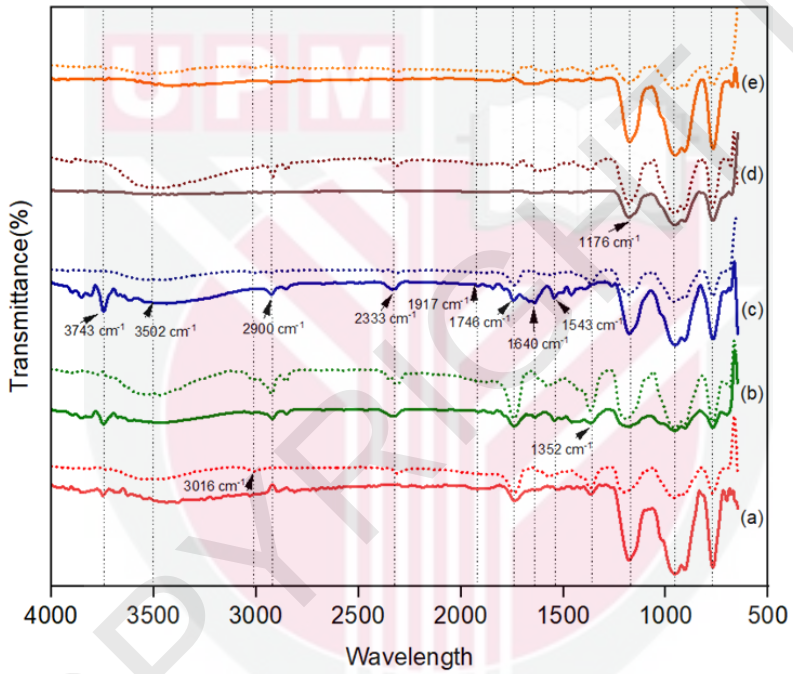

Figure 4.25 : The FTIR spectrum of spent catalyst of CO_2 methanation reaction with (a) 1 wt.% Ni, (b) 10 wt.% Ni, (c) 25 wt.% Ni, (d) 1/10 wt.% Fe/Ni, (e) 1/10 wt.% Co/Ni

Figure 4.26 presents morphological images of every spent CNT monolith catalyst. As the reaction progresses, the amount of catalyst coated onto the surface of the CNT monolith influences the image's depiction of the catalyst's minor morphological changes. As elaborated upon in Section 4.5.6, the surface morphology of the spent monometallic CNT catalyst illustrated in Figure 4.26 (a), (b), and (c) exhibited a correlation with its catalytic activity, such that an increased quantity of catalyst generated a more pronounced selectivity towards CH_4. As demonstrated in Figure 4.26 (d) and (c), the reaction could be enhanced more significantly by the morphology of the second metal catalyst

compared to a monometallic catalyst. Figure 4.26 (f) illustrates the morphology of the spent catalyst utilized in the stability test. This morphology demonstrates the catalyst's capacity to sustainably facilitate the CO_2 methanation reaction for an extended duration of time.

The XRD analyses of the spent mono and bimetallic catalysts after the CO_2 methanation reaction are shown in Figure 4.27 and Figure 4.28 respectively. The diffraction peaks of NiO were observed at 2θ values of 37.3°, 43.3°, and 62.9°, while those at 44.55°, 51.85°, and 76.3° were associated with Ni metal. The intensities of the peaks in the spent monometallic CNT catalysts were found to vary considerably with nickel loading in relation to the amount of nickel in the catalysts. As shown in Figure 4.28 (a) and (b), the diffraction peaks of spent 10 wt.% Ni CNT monoliths were maintained even though the reaction was running for 210 hours. Interestingly, over the 10 wt.% Ni CNT monolith catalyst, more intense peaks of Ni were found in the presence of the Co, but not for Fe. This indicates that Co stabilises the phase of Ni.

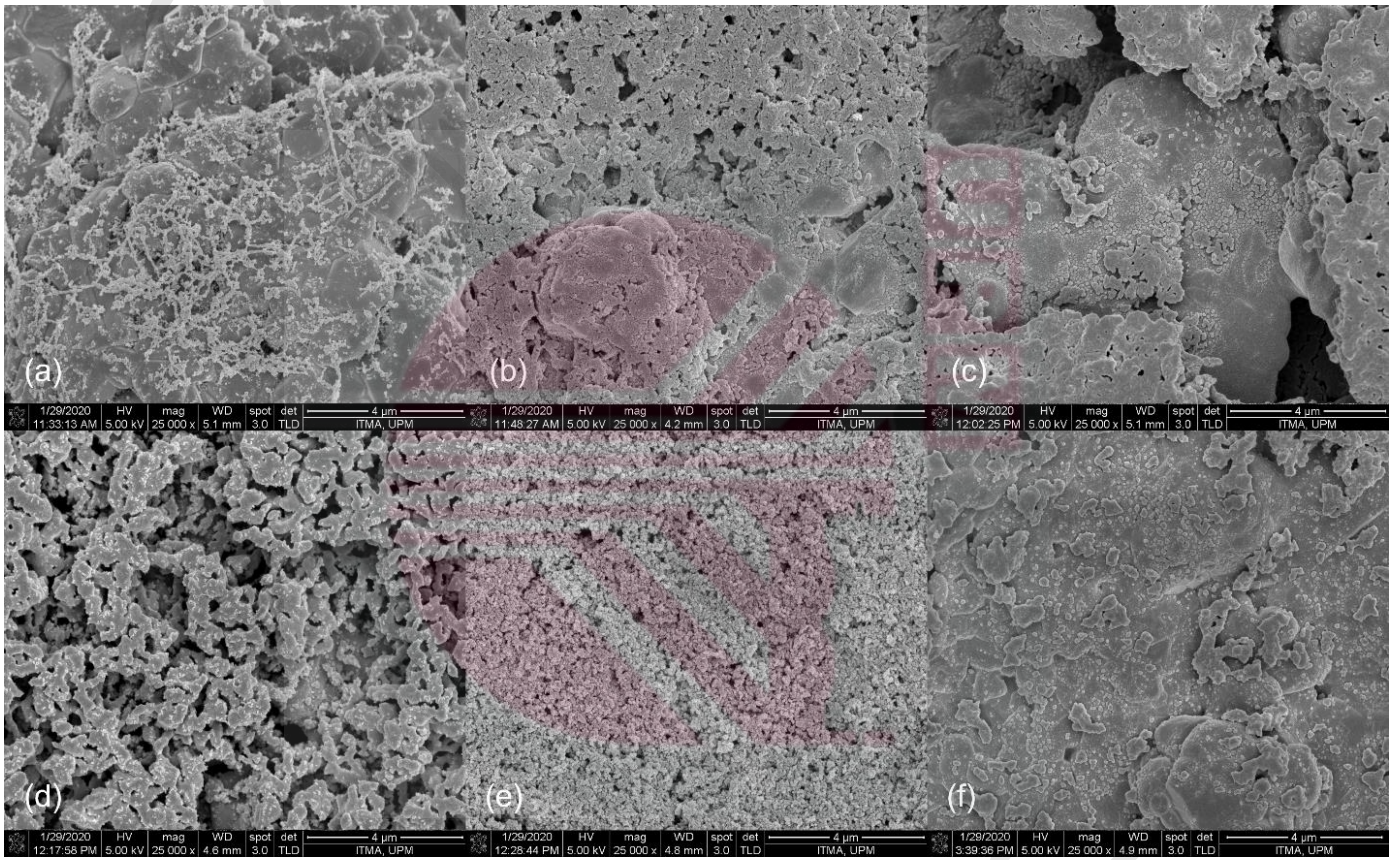

Figure 4.26 : Micrograph image spent catalyst of CO_2 methanation reaction (a) 1 wt.% Ni; (b) 10 wt.% Ni; (c) 25 wt.% Ni; (d) 1/10 wt.% Fe/Ni, (e) 1/10 wt.% Co/Ni and (f) 10 wt.% Ni after stability test using FESEM at 25 000 magnification

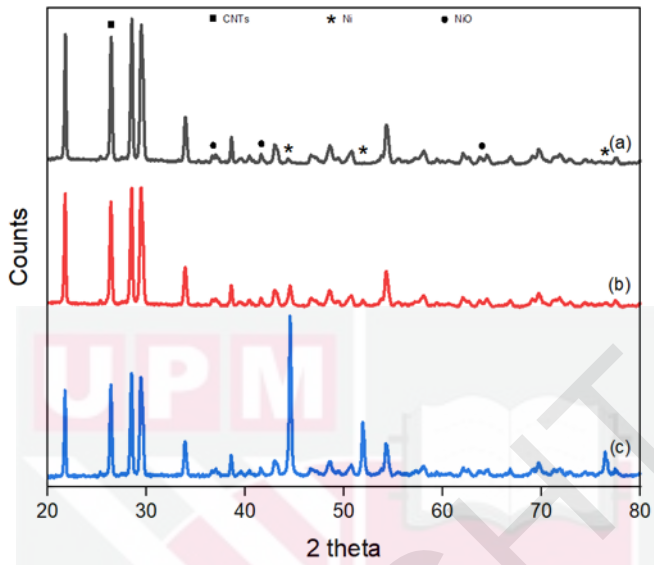

Figure 4.27 : XRD spectrum of (a) spent 1 wt.% Ni CNTs monolith; (b) spent 10 wt.% Ni CNTs monoliths and (c) spent 25 wt.% Ni CNTs monolith

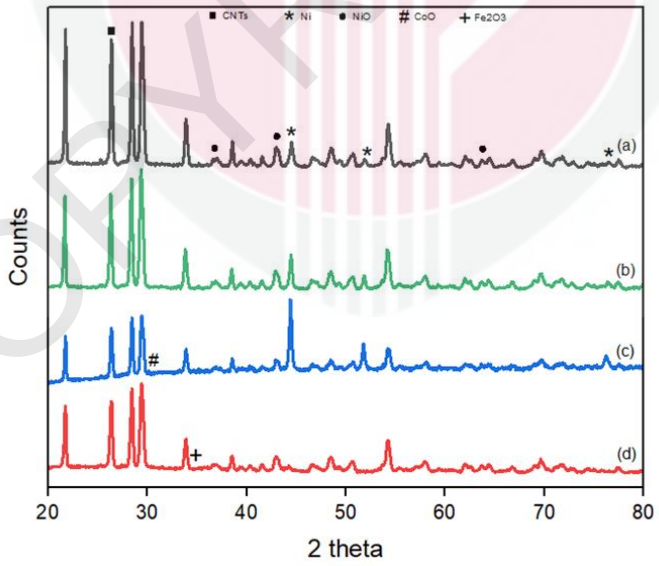

Figure 4.28 : XRD spectrum of (a) spent 10 wt.% Ni CNTs monolith; (b) spent 10 wt.% Ni CNTs monoliths catalyst after stability test (210 hours reaction); (c) spent 1/10 wt.% Co/Ni CNTs monolith catalyst and (d) spent 1/10 wt.% Fe/Ni CNTs monolith

4.4.5 Performance of catalytic activity at optimum condition

The catalytic performances were conducted at optimum conditions using a monometallic catalyst (Ni-CNT monolith), bimetallic catalysts (M/Ni-CNT monolith; M=Co or Fe), CNT monolith and cordierite monolith. Based on the results shown in Figure 4.29, both bimetallic CNT monolith catalysts show the highest CO_2 conversion, at 91.93% and 90.17% for Co/Ni CNT monolith catalyst and Fe/Ni CNT monolith catalyst, respectively. The increase in Ni loading by 25 wt.% Ni, followed by 10 wt.% Ni and 1 wt.% Ni CNT monolith catalysts show the highest performance for monometallic CNT monolith catalysts with 86.62%, 78.60%, and 77.49% respectively. Meanwhile, CNT monolith and bare monolith show 45.44% and 59.46% CO_2 conversion, respectively. Therefore, the results showed that the second metal catalyst could assist the Ni metal catalyst to disperse better, which improved the catalytic reaction. The results were consistent with the findings of Rahmani et al. (2016) who reported that a second metal to nickel catalyst had a dramatic effect on CO_2 methanation at low temperatures when compared to a monometallic catalyst due to the formation of dioxycarbonate species to increase the CO_2 conversion.

As shown in Figure 4.30, the highest performance of CH_4 selectivity is exhibited by 25 wt.% Ni CNT monolith (98.36%), followed by 1/10 wt.% Co/Ni-CNT monolith (94.64%), 10 wt.% Ni CNT monolith (93.03%), 1/10 wt.% Fe/Ni-CNT monolith (92.61%), 1 wt.% Ni CNT monolith (76.63%), CNT monolith (43.10%), and bare monolith (9.23%). The results show that monometallic and bimetallic catalysts exhibit more than 90% CH_4 selectivity, except for 1wt.% Ni CNT monolith. The results agree with (Xu et al., 2018) who reported that Co and Ni bimetallic catalysts demonstrated a synergetic effect between both metals and greatly enhanced catalytic activity at low temperature by coordinating the activation of H_2 and CO_2, obviously decreasing the activation energy towards CO_2 methanation. Moreover, Zhu et al. (2012) also stated that the Co-Ru catalyst surface was found to be highly active and selective in the CO_2 methanation reaction, as alloying Co with Ru enhanced the catalytic performance by correlating surface chemistry during the reaction.

The CNT monolith acts as catalyst support and could also perform the production of CH_4 with less than 50% selectivity even without the presence of a metal catalyst on the surface. This might be contributed by the Ni catalyst that exists inside the carbon nanotubes, as explained in section 4.3.4, where the growth is correlated with the CNT tip-growth mechanism. The efficient performance of the metal catalyst on the CNT monolith is equivalent to the CO selectivity, as the presence of a good catalyst could achieve a lower CO selectivity in the reaction. The CO selectivity shows less than 10% for 10 wt.%, 25 wt.%, 1/10 wt.% Fe/Ni, and 1/10 wt.% Co/Ni, except for 1 wt.% Ni which shows 23.37%, CNT monolith (56.90%), and bare monolith (90.77%) as illustrated in Figure 4.31.

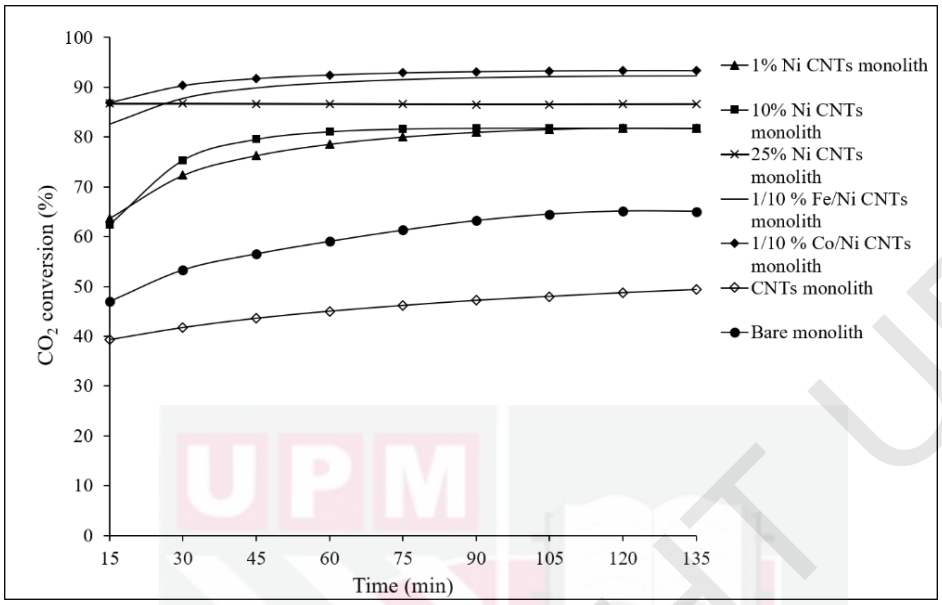

Figure 4.29 : CO_2 conversion for different types of catalyst

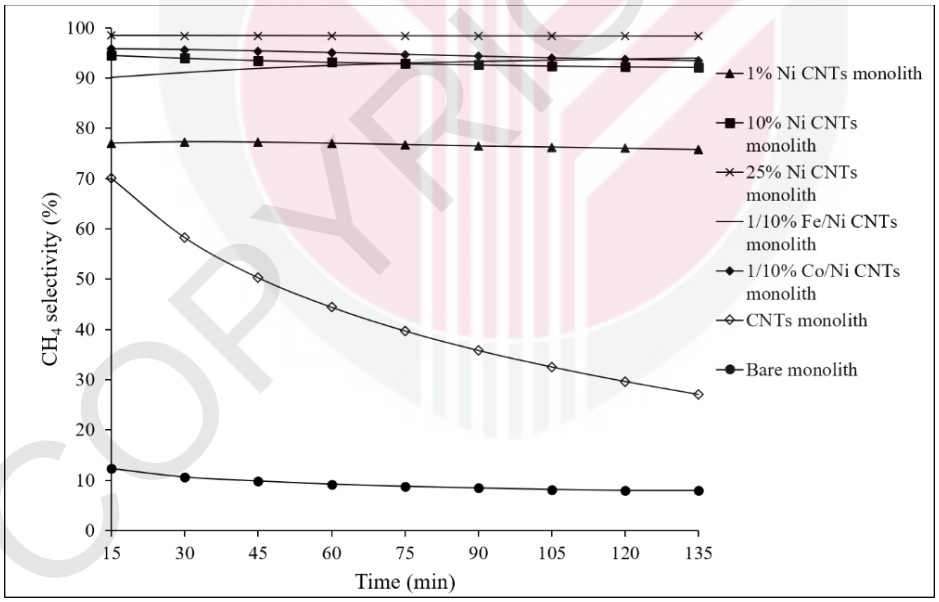

Figure 4.30 : CH_4 selectivity for different types of catalyst

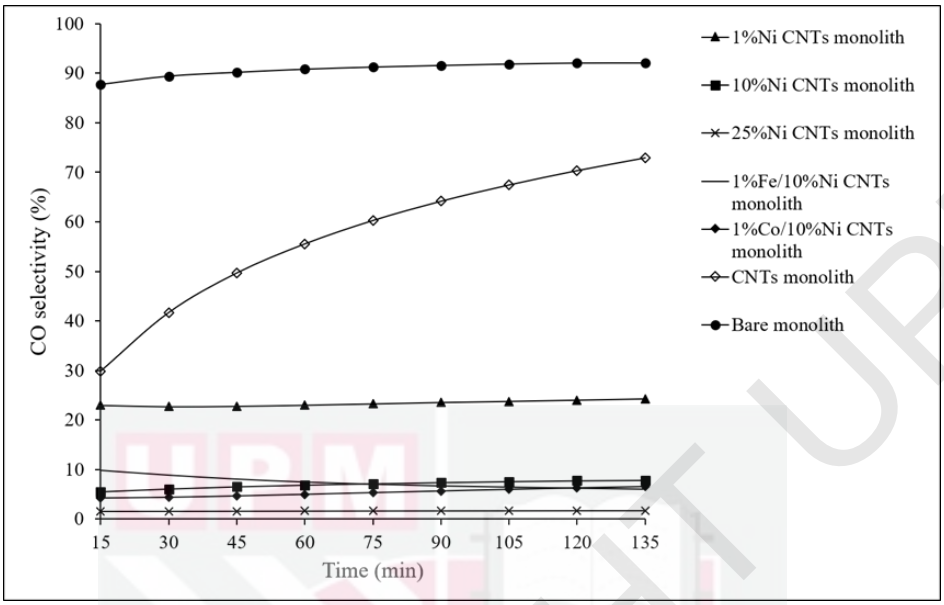

Figure 4.31 : CO selectivity for different types of catalyst

4.5 Catalyst stability

A catalytic test was carried out to evaluate the stability of the catalysts over time. The 10% Ni CNT monolith catalyst was chosen because it showed a good performances and less amount catalyst needed in the catalytic activity. The CO_2 methanation reaction was conducted at optimum condition that suggested by Taguchi method design which. The catalyst was performed in 210 hours in CO_2 methanation reaction as depicted in Figure 4.32 dan some example of data sheet attached in Appendix B. The results were observed in average of 74%, 84% and 16% of CO_2 conversion, CH_4 selectivity and CO selectivity respectively. The results showed that the CNT monolith catalyst provides a good potential in the CO_2 methanation reaction. However, the catalyst need more investigation due to typical lifespan of catalyst in an industrial methanation catalyst is 5 to 10 years, however some manufacturers claim a longer duration of up to 24 years (Miguel et al., 2018). According to this, the synthesized catalyst is still far away from the industrial performance, but it could be a good potential catalyst for the reaction.

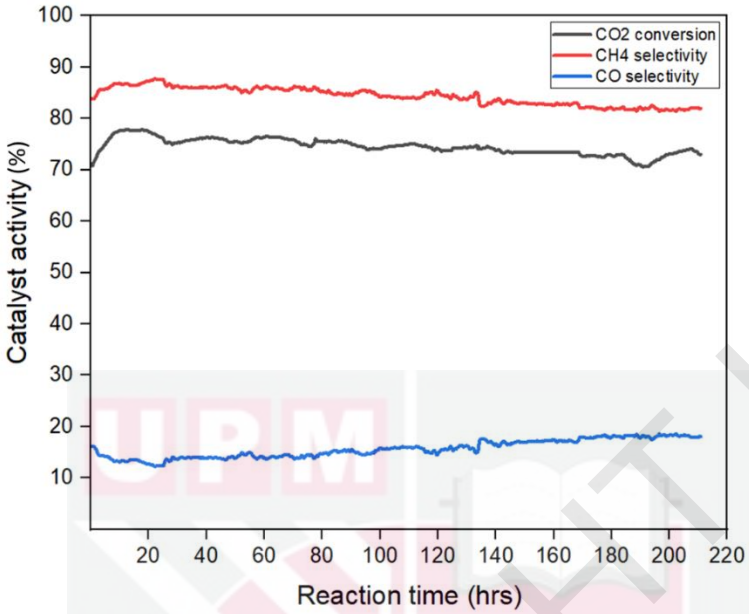

Figure 4.32 : The stability performance of monometallic CNTs monolith catalyst (10% Ni CNTs monolith catalyst).

4.6 Summary

This chapter summarises the result of research activity on CNT monolith and CNT monolith catalysts including the catalytic activity.

i) The immersion method is the most suitable preparation techniques of CNTs monolith structure.

ii) The CNT monolith was synthesised at optimum conditions of 1:1 Ni:CA (A); 5 mL/h injection rate of carbon source (B); 30 min reaction time (C); 700 ^{o}C operating temperature and (D); conducted using the Taguchi design method.

iii) Initially, the discussion concentrates on the result of CNTs' growth onto monolith via some preparation techniques before proceeding with direct liquid injection CVD. The preparation method is important to maintain the strength of cordierite monolith wall after the growth of CNTs. The Taguchi design was applied to determine the optimum condition for CNT growth on monoliths. Then, the CNT monolith was characterised and has been used in producing the CNT monolith catalyst. The catalyst activity was performed on CO_2 methanation in a fixed-bed reactor. The optimum conditions of the catalytic activity were also designed by the Taguchi method. The spent catalyst with the best catalytic performance was characterised and the stability test was performed.

CHAPTER 5

KINETIC STUDY AND MODEL FITTING OF CARBON DIOXIDE (CO_2) METHANATION CATALYST

5.1 Introduction

In this chapter, the details of the kinetic study, the catalytic reaction mechanism and the kinetic model are discussed. The kinetic study is conducted using 10 wt.% Ni and 1/10 wt.% Co/Ni CNT monolith catalyst. The model fittings of the catalyst at steady state and the catalytic reaction kinetics are presented.

5.2 The attachment between metal and CNTs monolith

The possible active sites could be present on the CNT monolith support due to the presence of carboxylic acid groups at the rims and wall defects that can be functionalized. Moreover, the carbon vacancies and doping activity with some heteroatoms to replace carbon atoms in the wall create other possible defects. The nanoparticles can also attach on to the CNTs support to become the active sites in the reaction. Figure 5.1 illustrates all the possible sites present in CNTs that can perform catalytic activity (Garcia, 2014). CNTs without presence of any metal can also act as catalysts for the oxidative dehydrogenation of hydrocarbons. Typically, these CNTs correspond to oxygenated functional groups like carboxylic acids, quinone-like carbonyl groups, and hydroxyl groups, as shown in Figure 5.2 (Liu et al., 2008; Qi et al., 2013).

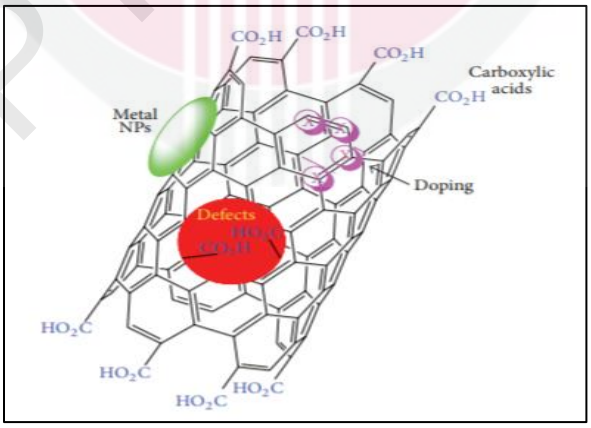

Figure 5.1 : The possible active sites occurs on CNTs surface (Garcia, 2014).

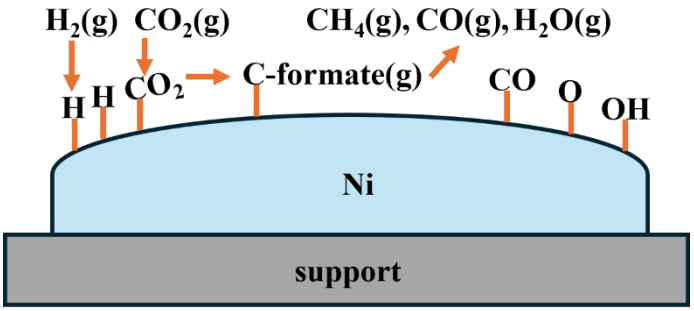

Figure 5.2 : The CNTs to mask selectively oxygenated functional groups to assess the nature of the active sites (Liu et al., 2008).

5.3 Reaction mechanism

The reaction mechanism of CO_2 methanation on nickel catalysts has been discussed by Weatherbee and Bartholomew (1982). The basis of mechanism proposed for CO_2 methanation generally falls into two categories: (i) conversion of CO_2 to CO via RWGS followed by CO methanation, and (ii) direct hydrogenation of CO_2 to CH_4 by a similar mechanism route as CO methanation. Previous literature has considered the mechanism of CO_2 methanation proceeds by transformation of CO_2 to CO, followed by CO methanation or a series of elementary steps, which are summarised in Table 5.1.

The development of rate laws from heterogeneous catalytic data includes the measurement of the concentrations of reactants and products over time, which can be used to calculate reaction rates and selectivity could postulate catalytic mechanism and derive rate laws for various mechanisms. The type of a mechanism indicates an adsorption step, a surface reaction step, and a desorption step which is one of the steps that is rate limiting, as tabulated in Appendix C1.

Table 5.1 : Proposed sequence of elementary steps in CO_2 methanation (Weatherbee & Bartholomew, 1982)

Reaction				Equation
Dissociation of H_2 to hydrogen atoms	H_2 (g) + 2 S^*	$\overset{k_1}{\underset{k_{-1}}{\rightleftharpoons}}$	2H-S^*	5.1
Dissociation of CO_2 to CO and oxygen atoms	CO_2 (g) + 2 S^*	$\overset{k_2}{\underset{k_{-2}}{\rightleftharpoons}}$	CO-S^* + O-S^*	5.2
Adsorption/desorption of CO can dissociate to carbon and oxygen atom	CO-S^*	$\overset{k_3}{\underset{k_{-3}}{\rightleftharpoons}}$	CO (g) + S^*	5.3
	CO-S^* + S^*	$\overset{k_4}{\underset{k_{-4}}{\rightleftharpoons}}$	C-S^* + O- S^*	5.4
Hydrogenation of adsorbed carbon and carbene intermediates to CH_4	C-S^* + H-S^*	$\overset{k_5}{\underset{k_{-5}}{\rightleftharpoons}}$	CH-S^* + S^*	5.5
	CH-S^* + H-S^*	$\overset{k_6}{\underset{k_{-6}}{\rightleftharpoons}}$	CH_2-S^* + S^*	5.6
	CH_2-S^* + H-S^*	$\overset{k_7}{\underset{k_{-7}}{\rightleftharpoons}}$	CH_3-S^* + S^*	5.7
	CH_3-S^* + H-S^*	$\overset{k_8}{\underset{k_{-8}}{\rightleftharpoons}}$	CH_4-S^* + S^*	5.8
	CH_4-S^*	$\overset{k_9}{\underset{k_{-9}}{\rightleftharpoons}}$	CH_4 (g) + S^*	5.9
Hydrogenation of adsorbed oxygen to H_2O	O-S^* + H-S^*	$\overset{k_{10}}{\underset{k_{-10}}{\rightleftharpoons}}$	OH-S^* + S^*	5.10
	OH-S^* + H-S^*	$\overset{k_{11}}{\underset{k_{-11}}{\rightleftharpoons}}$	H_2O-S^* + S^*	5.11
	H_2O-S^*	$\overset{k_{12}}{\underset{k_{-12}}{\rightleftharpoons}}$	H_2O (g) + S^*	5.12

* Refers to a surface site

5.4 Kinetic and model fittings of the catalytic reaction at steady state

The kinetic studies of hydrogenation of CO_2 to methane over 10 wt.% Ni CNTs and 1/10 wt.% Co/Ni CNT monolith catalysts are presented in detail for discussion. As a function of temperature, the range of reaction temperatures is considered at 300 °C, 350 °C, 400 °C and 450 °C. The kinetic behaviours of

CO_2 methanation were investigated over a catalyst using CO_2 and H_2 as reactants and CH_4 as products. The catalytic reaction rate from the experimental rate measurement fits with the Langmuir-Hinshelwood (L-H) rate expression due to the consideration of adsorption or desorption process occurring on the catalyst surface as well as the surface reaction, which can directly extrapolate the L-H rate expression to obtain the best fitted model to the reaction data.

The reversible reaction of hydrogenation of CO_2 are highly exothermic as ΔH_r is -165 kJ/mol as described in the section 2.3. The equilibrium constant for CO_2 methanation reaction is obtained from the experimental data that collected at the steady state to calculate the K_{P2} theoretical via Equation 3.13. The K_{P2} theoretical values as tabulated in Table 5.2 and Table 5.3 for both catalyst at temperature function dependence is presented using Arrhenius plot (ln K_{p2} vs 1/T(K)) as shown in Figure 5.4. The graph is illustrated the linear form of Equation 3.12. Therefore, the experimental equilibrium constant namely $K_{P1\ Ni\ CNTs\ monolith\ exp}$ and $K_{P1\ Co/Ni\ CNTs\ monolith\ exp}$ tabulated in Table 5.4 and Table 5.5 can be described using Equation 5.13 and Equation 5.14 respectively. The kinetic parameters of both Ni CNTs and Co/Ni-CNTs monolith catalyst tabulated in Table 5.6. The detail calculation is attached on Appendix C.

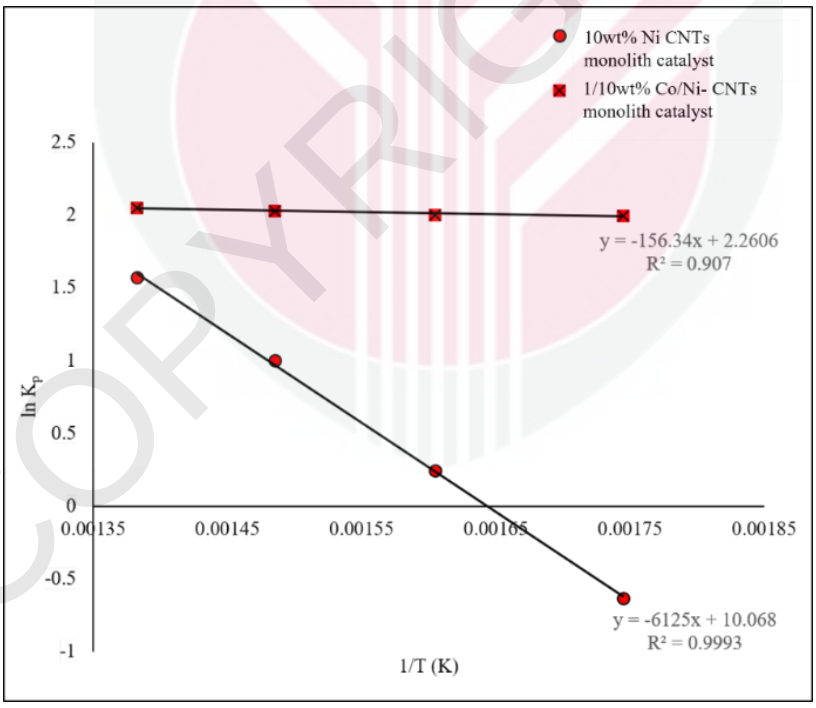

Figure 5.3 : Arrhenius plot of CO_2 methanation reaction predicted by Equation 5.18.

Table 5.2 : K_{P2} theoritical values of 10 wt.% Ni CNTs monolith catalyst at temperature function dependance

Temperature (K)	1/T(K)	CO_2 (mol/L)	H_2 (mol/L)	CH_4 (mol/L)	CO (mol/L)	Overall	Yield CH_4	Yield CO	Yield CO_2	Yield H_2	K_{p2} Eq. 3.13	ln Kp_2
573.15	0.00175	0.52	247.70	0.28	0.02	248.50	0.00113	0.00008	0.00211	0.99676	0.53170	-0.63167
623.15	0.00161	2.13	206.91	2.79	0.21	211.82	0.01315	0.00100	0.01005	0.97680	1.27802	0.24531
673.15	0.00149	1.36	137.62	3.83	0.17	142.80	0.02679	0.00120	0.00950	0.96371	2.71833	1.00002
723.15	0.00138	0.66	117.43	3.30	0.12	121.40	0.02718	0.00102	0.00545	0.96736	4.82102	1.57299

Table 5.3 : K_{P2} theoritical values of 1/10 wt.% Co/Ni CNTs monolith catalyst at temperature function dependence

Temperature (K)	1/T(K)	CO_2 (mol/L)	H_2 (mol/L)	CH_4 (mol/L)	CO (mol/L)	Overall	Yield CH_4	Yield CO	Yield CO_2	Yield H_2	K_{p2} Eq. 3.13	ln Kp_2
573.15	0.00175	0.55	127.86	4.17	0.00	132.57	0.03146	0.00000	0.00413	0.96441	7.34860	1.99451
623.15	0.00161	0.53	136.00	4.02	0.02	140.54	0.02860	0.00020	0.00374	0.96765	7.39413	2.00069
673.15	0.00149	0.52	135.99	4.04	0.30	140.54	0.02875	0.00210	0.00367	0.96758	7.57115	2.02435
723.15	0.00138	0.46	81.70	3.76	0.05	85.92	0.04380	0.00060	0.00536	0.95085	7.77396	2.05078

Table 5.4 : K_{P1} theoritical values of 10 wt.% Ni CNTs monolith catalyst at temperature function dependance

Temperature (K)	1/T(K)	lnK_{p2} (theo)	Reaction rate, r (mol/s.g_{cat})	K_{p1} (Eq. 5.13)
573.15	0.00175	-0.63167	26.06146	7.29965
623.15	0.00161	0.24531	53.56169	7.46118
673.15	0.00149	1.00002	51.43244	7.60152
723.15	0.00138	1.57298	64.05534	7.72458

Table 5.5 : K_{P1} theoritical values of 1/10 wt.% Co/Ni CNTs monolith catalyst at temperature function dependance

Temperature (K)	1/T(K)	lnKp_2 (theo)	Reaction rate, r (mol/s.g_{cat})	Kp_1 (Eq. 5.14)
573.15	0.00175	1.99451	25.33077	0.53872
623.15	0.00161	2.00069	54.17383	1.26986
673.15	0.00149	2.02435	50.34475	2.63528
723.15	0.00138	2.05078	62.34720	4.94369

$$K_{p_{1NiCNTs\ monolith}} = \exp(10.068 - \frac{6125}{T}) \quad (5.13)$$

$$K_{p_{1Co/Ni\ CNTs\ monolith}} = \exp(2.2606 - \frac{156.34}{T}) \quad (5.14)$$

Table 5.6 : Kinetic parameters evaluated from the Arrhenius plot using 10 wt.% Ni and bimetallic 1/10 wt.% Co/Ni-CNT monolith catalysts

Catalyst	Activation energy, E_a (kJ/mol)	Arrhenius factor (A)	R^2
Ni CNTs monolith	50.92	2.36 x 10^4	0.9993
Co/Ni-CNTs monolith	1.3	9.59	0.9070

5.5 Model fitting

The obtained data from the kinetic measurement was fitted with three models as described in the Section 2.10.2 in order to investigate the mechanical aspects of the hydrogenation of CO_2 to CH_4 over monometallic 10 wt.% Ni and bimetallic 1/10 wt.% Co/Ni-CNT monolith catalysts. The evaluation of kinetic parameters from the Levenberge Marquardt algorithm was employed using Polymath software version 6.1 based on the three models and fittings illustrated in Figure 5.4 and Figure 5.5 for 10 wt.% Ni and 1/10 wt.% Co/Ni-CNT monolith catalysts respectively. The rate constant, k of 1 wt.% Ni CNTs monolith exp and 1/10 wt.% Co/Ni CNTs monolith for the three models were determined from Polymath programme (Polymath Report in Appendix C) and tabulated in Table 5.7 and Table 5.8.

Table 5.7 : Model parameter guessed by Polymath programme for 10 wt.% Ni CNT monolith

Model 1: Single Site
$r = (k*PCO_2*PH_2)/(1+(KCO_2*PCO_2)+(KH_2*PH_2)+(KH_2O*PH_2O)+(KCH_4*PCH_4))$
Model 2: Dual Site
$r=(k*PCO_2*PH_2)/(1+(KCO_2*PCO_2)+(KH_2*PH_2)+(KH_2O*PH_2O)+(KCH_4*PCH_4))^{\wedge 2}$
Model 3: Only Reactant
$r=(k*PCO_2*PH_2)/(1+(KCO_2*PCO_2)+(KH_2*PH_2))^{\wedge 2}$

Temperature (K)	1/T(K)	PCO_2	PH_2	PCH_4	PCO	Model 1: Single Site		Model 2: Dual Site		Model 3: Only Reactant	
						k (Polymath)	ln k	k (Polymath)	ln k	k (Polymath)	ln k
573.15	0.00175	26.51370	9.18871	4.44877	0.00037	0.54322	-0.61023	3.569439	1.272408	1.32807	0.283727
623.15	0.0016	22.50339	5.33430	27.15335	0.00688	10.47155	2.34866	101.9997	4.624973	101.9986	4.624959
673.15	0.0015	74.93002	15.31820	43.34369	0.05905	0.85643	-0.15498	32.53605	3.482349	51.19495	3.935641
723.15	0.0013	41.05718	5.35426	30.38073	0.03132	6.75631	1.91048	101.9987	4.62496	101.9997	4.624973

Table 5.8 : Model parameter guessed by Polymath programme for 1/10 wt.% Co/Ni CNT monolith

Temperature (K)	1/T(K)	PCO_2	PH_2	PCH_4	PCO	Model 1: Single Site		Model 2: Dual Site		Model 3: Only Reactant	
						k (Polymath)	ln k	k (Polymath)	ln k	k (Polymath)	ln k
573.15	0.001745	28.83395	4.39203	18.25131	0.01025	1.21914	0.19814	25.57605	3.24166	101.9998	4.62497
623.15	0.001605	34.33891	5.13106	23.87254	0.02545	1.50157	0.40651	2.73383	1.00570	0.01339	-4.31346
673.15	0.001486	27.40206	4.28130	37.20789	0.07341	3.00180	1.09921	101.999	4.62496	101.9989	4.62496
723.15	0.001383	46.16279	4.49997	16.82110	0.03727	7.46122	2.00972	48.38939	3.87928	0.21784	-1.52398

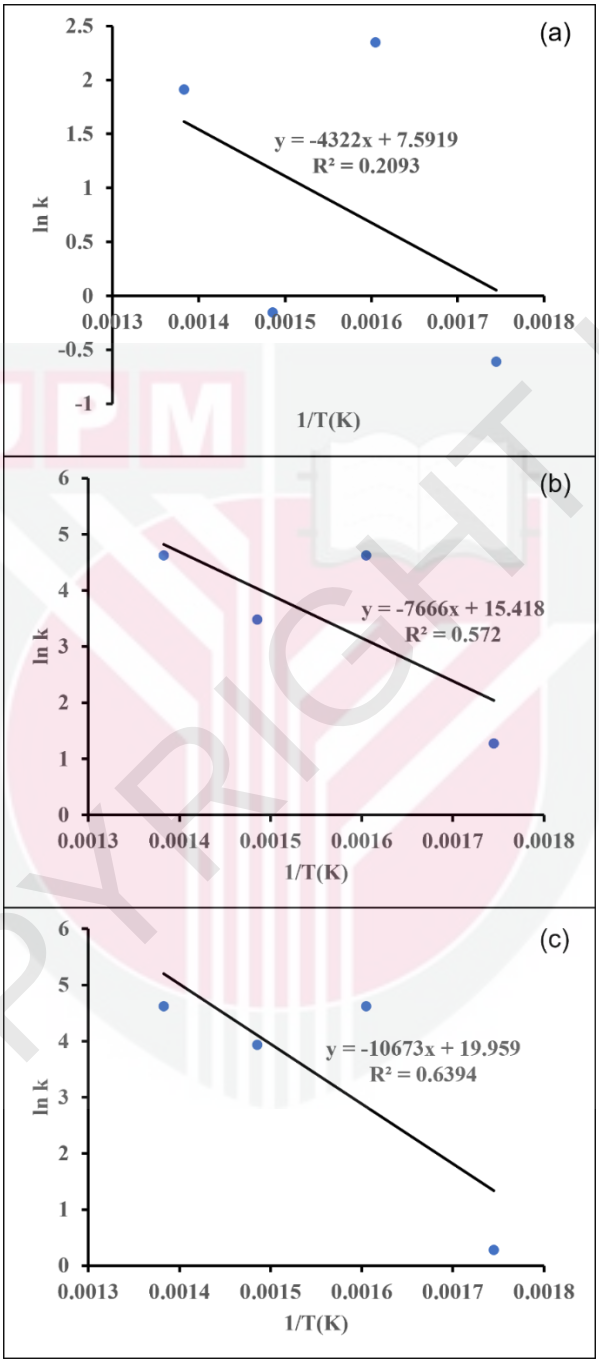

Figure 5.4 : Arrhenius plot for (a) model 1; (b) model 2; and (c) model 3 over 10 wt.% Ni CNTs monolith catalyst

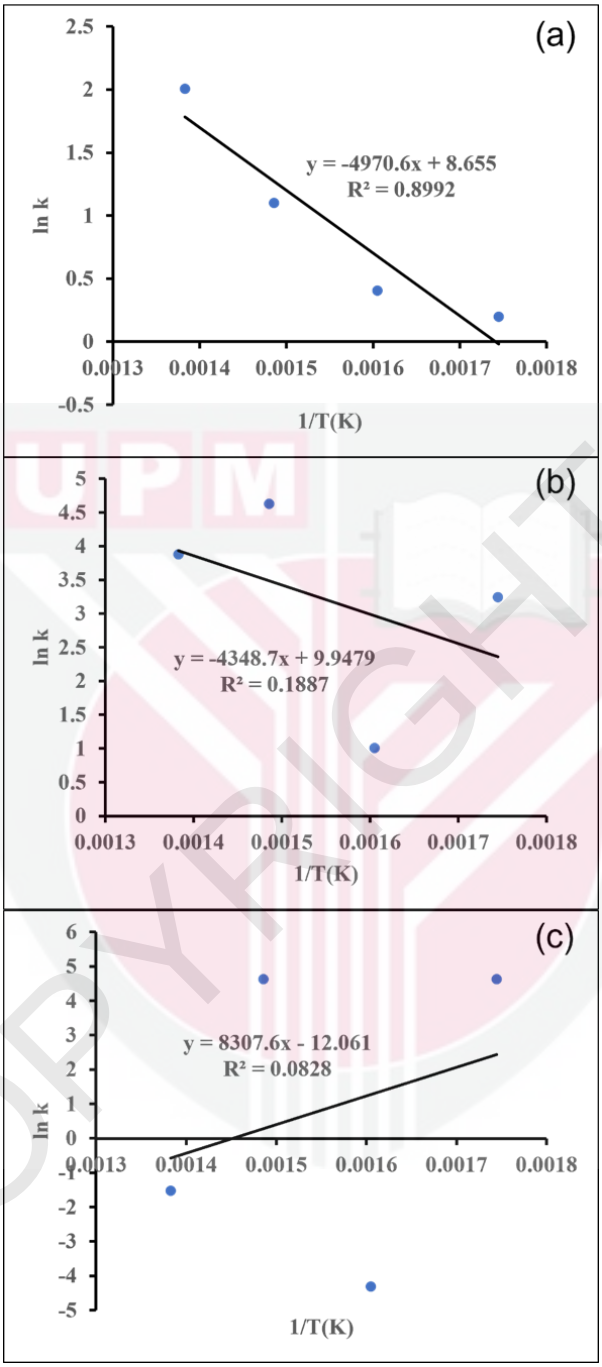

Figure 5.5 : Arrhenius plot for (a) model 1; (b) model 2; and (c) model 3 over 1/10 wt.% Co/Ni-CNTs monolith catalyst

Determination of the kinetic parameters as the activation energy (E_a) and correlation factor (R^2) represents the validity of the data fit into the L-H rate models. Therefore, the non-linear regression in Polymath can be used to evaluate the R^2. The obtained activation energy from each of the L-H rate models at the different reaction temperatures for the monometallic 10 wt.% Ni and bimetallic 1/10 wt.% Co/Ni-CNT monolith catalysts as shown in Table 5.9 and Table 5.10.

Table 5.9 : Kinetic parameters evaluated from the fitting rate data using 10 wt.% Ni CNTs monolith catalyst

Model	Activation energy (E_a), kJ/mol	Arrhenius factor (A)	R^2
1	35.93	1.98×10^3	0.2093
2	63.74	4.97×10^6	0.5720
3	88.74	4.66×10^8	0.6394

Table 5.10 : Kinetic parameters evaluated from the fitting rate data using 1/10 wt.% Co/Ni CNTs monolith catalyst

Model	Activation energy (E_a), kJ/mol	Arrhenius factor (A)	R^2
1	41.33	5.74×10^3	0.8992
2	36.16	2.09×10^4	0.1887
3	-69.07	5.78×10^6	0.0828

From Table 5.9 model 3 has the best fit for the 10 wt.% Ni CNT monolith catalyst based on R^2 of 0.6394 and the E_a of 88.74 kJ/mol. Although the results of the fitting are not good enough, it can still predict the best among the other two models. Therefore, based on model 3, the mechanism of the CO_2 methanation over 10 wt.% Ni CNT monolith catalyst is based on only reactant being adsorbed with dual-site mechanism as follows:

$$r_{CH_4} = \frac{\mathbf{1.33}(P_{CO_2} P_{H_2})}{(\mathbf{1 - 0.24}P_{CO_2} + \mathbf{0.11}P_{H_2})} \quad (5.15)$$

Table 5.10 showed that model 1 has the best model fit on the data of CO_2 methanation over the bimetallic 1/1 wt.% Co/Ni-CNTs monolith catalyst based

on R^2 of 0.8992. The value of E_a of of bimetallic catalyst is slightly higher than monometaliic catalyst which are 41.33 kJ/mol and 88.74 kJ/mol respectively. Model 3 does not fit the data of bimetallic catalyst. Therefore, the mechanism of the CO_2 methanation over 10 wt.% Ni CNT monolith catalyst from model 1 is based on all reactants and products are adsorbed with single-site mechansim as follows:

$$r_{CH_4} = \frac{\mathbf{1.22} P_{CO_2} P_{H_2}}{(\mathbf{1} + \mathbf{0.6} P_{CO_2} + \mathbf{1.08} P_{H_2} - \mathbf{19.32} P_{CH_4} - \mathbf{0.03} P_{H_2O})} \quad (5.16)$$

5.6 Summary

The kinetic studies have been evaluated by implementing three types of models that can express the reaction mechanism. The kinetic parameters are considered when one model fits the data in a perfect manner. As a conclusion of these studies, the monometallic 10 wt.% Ni CNTs monolith catalyst is based on only reactant being adsorbed with dual-site mechanism while the bimetallic of 1/10 wt.% Co/Ni-CNTs monolith catalyst is based on all reactants and products being adsorbed with single-site mechanism.

CHAPTER 6

CONCLUSION AND RECOMMENDATIONS

6.1 Conclusion

This research was conducted to achieve the following objectives: to investigate the optimum conditions of CNTs' growth in the application of design of experiment (DOE) by the Taguchi method and synthesise the CNTs growth onto monolith support using chemical vapour deposition (CVD) at optimum conditions, to characterise the CNT monolith and CNT monolith catalysts labelled as Ni-CNT and M/Ni-CNT respectively, where M is Fe or Co as the second metal, to study the catalytic activity of Ni/CNTs and M/Ni-CNTs on CO_2 methanation reaction towards CO_2 conversion and CH_4 selectivity and investigate the optimum condition of methanation reaction by Taguchi method in design of experiment (DOE), to evaluate the stability and reusability of the CNTs monolith catalyst in CO_2 methanation reaction, to establish the kinetic studies (mechanism studies) of CNTs monolith catalyst in CO_2 methanation reaction. Therefore, the brief conclusions from the findings of the studies are as follows:

To achieve the objectives of formulation, the optimal conditions of CNTs growth are a 1:1 ratio of Ni to acid, 5 ml of carbon source, and 30 minutes of chemical reaction at 700^{o}C via the CVD process. The CNTs growth supported onto monolith has been characterised.

To analyse the physical and chemical properties of CNT monolith and CNT monolith catalysts determined by various characterisation techniques. This characterisation could explain the catalytic activity of the Ni/CNTs and M/Ni-CNTs on CO_2 methanation reaction towards CO_2 conversion and CH_4 selectivity, as well as investigate the optimum conditions of the methanation reaction.

To evaluate the performance, the catalyst was tested in a fixed-bed reactor at operating conditions at a temperature dependence of 400°C with mixed gases supplied at 10% CO_2:40% H_2:55% N_2 in the heating process at a flowrate of 30 ml/min as suggested by the Taguchi method. The catalyst was performed in 210 hours in CO_2 methanation reaction, and the results were observed at an average of 74%, 84% and 16% of CO_2 conversion, CH_4 selectivity, and CO selectivity, respectively.

To present the catalyst behaviour in CO_2 methanation, the suitable kinetics model was fitted with the experimental data to investigate the reaction mechanism of the reaction. The monometallic of 10 wt.% Ni CNT monolith

catalyst comply with the model based on only reactants are adsorbed with dual-site mechanism while the bimetallic of 1/10 wt.% Co/Ni-CNT monolith catalyst is based on all reactants and products being adsorbed with single-site mechanism.

6.2 Recommendation

Based on the findings, the following recommendation should be considered for the future works:

1. Reactivating the catalyst after complete deactivation for subsequent reuse in the CO2 methanation reaction.

2. Comparison of the synthesised catalyst with the commercial catalyst under the same operating conditions to gain more information about the capability of the CNT monolith catalyst.

3. Investigation of the carbon source with a different OH number in the structure when synthesising the CNTs onto monolith support for better growth.

REFERENCES

Abate, S., Barbera, K., Giglio, E., Deorsola, F., Bensaid, S., Perathoner, S., Pirone, R., & Centi, G. (2016). Synthesis, characterization, and activity pattern of Ni-Al hydrotalcite catalysts in CO_2 methanation. *Industrial & Engineering Chemistry Research*, *55*(30), 8299-8308.

Abelló, S., Berrueco, C., & Montané, D. (2013). High-loaded nickel-alumina catalyst for direct CO_2 hydrogenation into synthetic natural gas (SNG). *Fuel*, *113*, 598-609.

Ahmad, W., Younis, M. N., Shawabkeh, R., & Ahmed, S. (2017). Synthesis of lanthanide series (La, Ce, Pr, Eu & Gd) promoted Ni/γ-Al_2O_3 catalysts for methanation of CO_2 at low temperature under atmospheric pressure. *Catalysis Communications*, *100*, 121-126.

Ahsan, M., Ahsan, P. M., Islam, M., & Asif, F. (2019). Structural and electrical properties of copper doped lanthanum manganite NPs. *Results in physics*, *15*, 102600.

Akbari, E., & Buntat, Z. (2017). Benefits of using carbon nanotubes in fuel cells: a review. *International Journal of Energy Research*, *41*(1), 92-102.

Al-Fatesh, A. S., Kaydouh, M.-N., Ahmed, H., Ibrahim, A. A., Alotibi, M. F., Osman, A. I., & El Hassan, N. (2023). Sr Promoted Ni/W–Zr Catalysts for Highly Efficient CO2 Methanation: Unveiling the Role of Surface Basicity. *Langmuir*, *39*(49), 17723-17732.

Allaedini, G., Aminayi, P., & Tasirin, S. M. (2015). The effect of alumina and magnesia supported germanium nanoparticles on the growth of carbon nanotubes in the chemical vapor deposition method. *Journal of Nanomaterials*, *2015.*

Anjalin, F. (2014). Synthesis and characterization of MWCNTs/PVDF nanocomposite and its electrical studies. *Der. Pharma. Chemica*, *6*, 354-359.

Astié, V., Millon, C., Decams, J. M., & Bartasyte, A. (2018). Direct liquid injection chemical vapor deposition. Chemical vapor deposition for nanotechnology. *Intech Open*, 1, 29-51.

Atieh, M. A., Bakather, O. Y., Al-Tawbini, B., Bukhari, A. A., Abuilaiwi, F. A., & Fettouhi, M. B. (2010). Effect of carboxylic functional group functionalized on carbon nanotubes surface on the removal of lead from water. *Bioinorganic Chemistry and Applications*, *2010*, 603978.

Atzori, L., Cutrufello, M. G., Meloni, D., Onida, B., Gazzoli, D., Ardu, A., Monaci, R., Sini, M. F., & Rombi, E. (2021). Characterization and catalytic activity of soft-templated NiO-CeO_2 mixed oxides for CO and CO_2 co-

methanation. *Frontiers of Chemical Science and Engineering*, *15*(2), 251-268.

Avotina, L., Goldmane, A. E., Zaslavskis, A., Romanova, M., Vanags, E., Sorokins, H., Kizane, G., & Dekhtyar, Y. (2023). Estimation of Thermal Stability of Si-SiO2-W Nanolayered Structures with Infrared Spectrometry. *Materials*, *17*(1), 7.

Awasthi, K., Srivastava, A., & Srivastava, O. (2005). Synthesis of carbon nanotubes. *Journal of Nanoscience and Nanotechnology*, *5*(10), 1616-1636.

Aziz, M., Jalil, A., Triwahyono, S., & Ahmad, A. (2015). CO_2 methanation over heterogeneous catalysts: recent progress and future prospects. *Green Chemistry*, *17*(5), 2647-2663.

Aziz, M., Jalil, A., Triwahyono, S., & Saad, M. (2015). CO_2 methanation over Ni-promoted mesostructured silica nanoparticles: Influence of Ni loading and water vapor on activity and response surface methodology studies. *Chemical Engineering Journal*, *260*, 757-764.

Aziz, M., Jalil, A., Triwahyono, S., & Sidik, S. (2014). Methanation of carbon dioxide on metal-promoted mesostructured silica nanoparticles. *Applied Catalysis A: General*, *486*, 115-122.

Azri, F. A., Sukor, R., Hajian, R., Yusof, N. A., Bakar, F. A., & Selamat, J. (2017). Modification strategy of screen-printed carbon electrode with functionalized multi-walled carbon nanotube and chitosan matrix for biosensor development. *Asian Journal of Chemistry*, *29*(1), 31.

Baddour, C. E., & Briens, C. (2005). Carbon nanotube synthesis: a review. *International Journal of Chemical Reactor Engineering*, *3*(1).

Baddour, C. E., Fadlallah, F., Nasuhoglu, D., Mitra, R., Vandsburger, L., & Meunier, J. L. (2009). A simple thermal CVD method for carbon nanotube synthesis on stainless steel 304 without the addition of an external catalyst. *Carbon*, *47*(1), 313-318.

Baharudin, L., & Watson, M. J. (2018). Monolithic substrate support catalyst design considerations for steam methane reforming operation. *Reviews in Chemical Engineering*, *34*(4), 481-501.

Baldauf-Sommerbauer, G., Lux, S., Aniser, W., Bitschnau, B., Letofsky-Papst, I., & Siebenhofer, M. (2018). Steady-state and controlled heating rate methanation of CO_2 on Ni/MgO in a bench-scale fixed bed tubular reactor. *Journal of CO_2 Utilization*, *23*, 1-9.

Baraj, E., Vagaský, S., Hlinčik, T., Ciahotný, K., & Tekáč, V. (2016). Reaction mechanisms of carbon dioxide methanation. *Chemical Papers*, *70*(4), 395-403.

Barrios, V. A. E., Méndez, J. R. R., Aguilar, N. V. P., Espinosa, G. A., & Rodríguez, J. L. D. (2012). FTIR: An essential characterization technique for polymeric materials. *Infrared Spectroscopy Materials Science, Engineering and Technology*, 195-214.

Baykal, A., Senel, M., Unal, B., Karaoğlu, E., Sözeri, H., & Toprak, M. S. (2013). Acid functionalized multiwall carbon nanotube/magnetite (MWCNT)-COOH/Fe_3O_4 hybrid: synthesis, characterization and conductivity evaluation. *Journal of Inorganic and Organometallic Polymers and Materials*, *23*(3), 726-735.

Bian, Z., Chan, Y. M., Yu, Y., & Kawi, S. (2020). Morphology dependence of catalytic properties of Ni/CeO_2 for CO_2 methanation: A kinetic and mechanism study. *Catalysis Today*, *347*, 31-38.

Birch, M. E., Ruda-Eberenz, T. A., Chai, M., Andrews, R., & Hatfield, R. L. (2013). Properties that influence the specific surface areas of carbon nanotubes and nanofibers. *Annals of Occupational Hygiene*, *57*(9), 1148-1166.

Bodiba, V., Igbokwe, E., Mahangani, N., Aberefa, O., Daramola, M. O., & Iyuke, S. E. (2018). Production of CNT yarns for use as filaments in incandescent bulb: effect of carbon source and state of catalyst on production of CNT. *IOP Conference Series: Materials Science and Engineering*. 413, 012027.

Boger, T., Heibel, A. K., & Sorensen, C. M. (2004). Monolithic catalysts for the chemical industry. *Industrial & Engineering Chemistry Research*, *43*(16), 4602-4611.

Bondi, S., Lackey, W., Johnson, R., Wang, X., & Wang, Z. (2006). Laser assisted chemical vapor deposition synthesis of carbon nanotubes and their characterization. *Carbon*, *44*(8), 1393-1403.

Boot-Handford, M. E., Abanades, J. C., Anthony, E. J., Blunt, M. J., Brandani, S., Mac Dowell, N., Fernández, J. R., Ferrari, M. C., Gross, R., & Hallett, J. P. (2014). Carbon capture and storage update. *Energy & Environmental Science*, *7*(1), 130-189.

Bukhari, S., Chong, C., Setiabudi, H., Ainirazali, N., Aziz, M., Jalil, A., & Chin, S. (2019). Optimal Ni loading towards efficient CH_4 production from H_2 and CO_2 over Ni supported onto fibrous SBA-15. *International Journal of Hydrogen Energy*, *44*(14), 7228-7240.

Calo, J., Cazorla-Amorós, D., Linares-Solano, A., Roman-Martinez, M., & De Lecea, C. S. M. (1997). The effects of hydrogen on thermal desorption of oxygen surface complexes. *Carbon*, *35*(4), 543-554.

Centi, G., & Perathoner, S. (2009). Opportunities and prospects in the chemical recycling of carbon dioxide to fuels. *Catalysis Today*, *148*(3-4), 191-205.

Cepollaro, E. M., Cimino, S., Lisi, L., Biesuz, M., Santhosh, B., & Sorarù, G. D. (2022). Ru/Al_2O_3 on polymer-derived SiC foams as structured catalysts for CO_2 methanation. *Catalysts*, *12*(9), 956.

Chagas, F., da Silva, E. F. M., Barbosa, C. M., & Almeida, L. C. (2023). Structured catalyst used in gas chromatography for carbon oxides methanation. *Chemical Engineering and Processing-Process Intensification*, *185*, 109312.

Champon, I., Bengaouer, A., Chaise, A., Thomas, S., & Roger, A. C. (2019). Carbon dioxide methanation kinetic model on a commercial Ni/Al_2O_3 catalyst. *Journal of CO_2 Utilization*, *34*, 256-265.

Champon, I., Bengaouer, A., Chaise, A., Thomas, S., & Roger, A. C. (2020). Modelling the sintering of nickel particles supported on γ-alumina under hydrothermal conditions. *Catalysts*, *10*(12), 1477.

Chen, C. M., Dai, Y. M., Huang, J. G., & Jehng, J. M. (2006). Intermetallic catalyst for carbon nanotubes (CNTs) growth by thermal chemical vapor deposition method. *Carbon*, *44*(9), 1808-1820.

Chen, P. L., Chang, J. K., Kuo, C. T., & Pan, F. M. (2004). Anodic aluminum oxide template assisted growth of vertically aligned carbon nanotube arrays by ECR-CVD. *Diamond and Related Materials*, *13*(11-12), 1949-1953.

Chiang, J. H., & Hopper, J. R. (1983). Kinetics of the hydrogenation of carbon dioxide over supported nickel. *Industrial & Engineering Chemistry Product Research and Development*, *22*(2), 225-228.

Dahmen, K. H. (2003). Chemical vapor deposition. *Academic Press*, 787-808.

Daroughegi, R., Meshkani, F., & Rezaei, M. (2017). Enhanced activity of CO_2 methanation over mesoporous nanocrystalline $Ni\text{-}Al_2O_3$ catalysts prepared by ultrasound-assisted co-precipitation method. *International Journal of Hydrogen Energy*, *42*(22), 15115-15125.

Daroughegi, R., Meshkani, F., & Rezaei, M. (2017). Enhanced activity of CO2 methanation over mesoporous nanocrystalline Ni–Al2O3 catalysts prepared by ultrasound-assisted co-precipitation method. *International Journal of Hydrogen Energy*, *42*(22), 15115-15125.

Daturi, M., Binet, C., Lavalley, J., & Blanchard, G. (2000). Surface FTIR investigations on $Ce_xZr_{1-x}O_2$ system. *Surface and Interface Analysis: An International Journal devoted to the development and application of techniques for the analysis of surfaces, interfaces and thin films*, *30*(1), 273-277.

Davydov, A. A. (1995). Basic sites on the surface of oxide catalysts responsible for oxidative methane coupling. *Chemical Engineering & Technology*, *18*(1), 7-11.

De Masi, D., Asensio, J. M., Fazzini, P. F., Lacroix, L. M., & Chaudret, B. (2020). Engineering iron-nickel nanoparticles for magnetically induced CO_2 methanation in continuous flow. *Angewandte Chemie International Edition*, *59*(15), 6187-6191.

Di, L., Yang, H., Xian, T., & Chen, X. (2018). Construction of Z-scheme g-C_3N_4/CNT/$Bi_2Fe_4O_9$ composites with improved simulated-sunlight photocatalytic activity for the dye degradation. *Micromachines*, *9*(12), 613.

Dias, Y. R., & Perez-Lopez, O. W. (2021). CO_2 conversion to methane using Ni/SiO_2 catalysts promoted by Fe, Co and Zn. Journal of Environmental Chemical Engineering, 9(1), 104629.

Dubey, P., Muthukumaran, D., Dash, S., Mukhopadhyay, R., & Sarkar, S. (2005). Synthesis and characterization of water-soluble carbon nanotubes from mustard soot. *Pramana*, *65*(4), 681-697.

Duc Vu Quyen, N., Quang Khieu, D., Tuyen, T. N., Xuan Tin, D., & Thi Hoang Diem, B. (2019). Carbon nanotubes: Synthesis via chemical vapour deposition without hydrogen, surface modification, and application. *Journal of Chemistry*, *2019*, 4260153.

Dündar-Tekkaya, E., & Karatepe, N. (2015). Investigation of the effect of reaction time, weight ratio, and type of catalyst on the yield of multi-wall carbon nanotubes via chemical vapor deposition of acetylene. *Fullerenes, Nanotubes and Carbon Nanostructures*, *23*(10), 853-859.

Esquenazi, G., Brinson, B., & Barron, A. (2018). Catalytic growth of carbon nanotubes by direct liquid injection CVD using the nanocluster $[H_xPMo_{12}O_{40} \subset H_4Mo_{72}Fe_{30}(O_2CMe)_{15}O_{254}(H_2O)_{98-y}(EtOH)_y]$. *C*, *4*(1), 17.

Ewald, S., Kolbeck, M., Kratky, T., Wolf, M., & Hinrichsen, O. (2019). On the deactivation of Ni-Al catalysts in CO_2 methanation. *Applied Catalysis A: General*, *570*, 376-386.

Feng, F., Song, G., Xiao, J., Shen, L., & Pisupati, S. V. (2019). Carbon deposition on Ni-based catalyst with TiO_2 as additive during the syngas methanation process in a fluidized bed reactor. *Fuel*, *235*, 85-91.

Feng, L., Li, K. Z., Lu, J. H., & Qi, L. H. (2017). Effect of growth temperature on carbon nanotube grafting morphology and mechanical behavior of carbon fibers and carbon/carbon composites. *Journal of Materials Science & Technology*, *33*(1), 65-70.

Feng, Y., Yang, W., & Chu, W. (2015). A study of CO_2 methanation over Ni-based catalysts supported by CNTs with various textural characteristics. *International Journal of Chemical Engineering*, *2015*, 795386.

Firdaus, R., Afandi, N. S., Khavarian, M., & Mohamed, A. R. (2019). Effect of reaction time and catalyst feed rate towards carbon nanotubes yields and purity by using rotary reactor. *Sains Malaysiana*, *48*(6), 1187-1194.

Fogler, H. S. (2010). *Essentials of Chemical Reaction Engineering: Essenti Chemica Reactio Engi*. Pearson Education 3rd Edition. 33-49.

Frontera, P., Macario, A., Ferraro, M., & Antonucci, P. (2017). Supported catalysts for CO_2 methanation: a review. *Catalysts*, *7*(2), 59.

Fukuhara, C., Hayakawa, K., Suzuki, Y., Kawasaki, W., & Watanabe, R. (2017). A novel nickel-based structured catalyst for CO_2 methanation: A honeycomb-type Ni/CeO_2 catalyst to transform greenhouse gas into useful resources. *Applied Catalysis A: General*, *532*, 12-18.

Futko, S., Shulitskii, B., Labunov, V., & Ermolaeva, E. (2015). Simulation of the kinetics of growth of iron nanoparticles in the process of chemical vapor deposition of hydrocarbons with injection of ferrocene for the synthesis of carbon-nanotube arrays. *Journal of Engineering Physics and Thermophysics*, *88*(6), 1432-1441.

Garbarino, G., Bellotti, D., Riani, P., Magistri, L., & Busca, G. (2015). Methanation of carbon dioxide on Ru/Al_2O_3 and Ni/Al_2O_3 catalysts at atmospheric pressure: catalysts activation, behaviour and stability. *International Journal of Hydrogen Energy*, *40*(30), 9171-9182.

García-Bordejé, E., Kapteijn, F., & Moulijn, J. (2002). Preparation and characterisation of carbon-coated monoliths for catalyst supports. *Carbon*, *40*(7), 1079-1088.

Garcia, H. (2014). Allotropic carbon nanoforms as advanced metal-free catalysts or as supports. *Advances in Chemistry*, *2014, 906781*.

Ge, Y., He, T., Han, D., Li, G., Zhao, R., & Wu, J. (2019). Plasma-assisted CO_2 methanation: effects on the low-temperature activity of an Ni-Ce catalyst and reaction performance. *Royal Society Open Science*, *6*(10), 190750.

Ghaib, K., & Ben-Fares, F.-Z. (2018). Power-to-Methane: A state-of-the-art review. *Renewable and Sustainable Energy Reviews*, *81*, 433-446.

Gnanakumar, E. S., Chandran, N., Kozhevnikov, I. V., Grau-Atienza, A., Fernández, E. V. R., Sepulveda-Escribano, A., & Shiju, N. R. (2019). Highly efficient nickel-niobia composite catalysts for hydrogenation of CO_2 to methane. *Chemical Engineering Science*, *194*, 2-9.

Groppi, G., & Tronconi, E. (2005). Honeycomb supports with high thermal conductivity for gas/solid chemical processes. *Catalysis Today*, *105*(3-4), 297-304.

Guczi, L., Boskovic, G., & Kiss, E. (2010). Bimetallic cobalt based catalysts. *Catalysis Reviews: Science and Engineering*, *52*(2), 133-203.

Guilera, J., del Valle, J., Alarcón, A., Díaz, J. A., & Andreu, T. (2019). Metal-oxide promoted Ni/Al_2O_3 as CO_2 methanation micro-size catalysts. *Journal of CO_2 Utilization*, *30*, 11-17.

Guillén Hurtado, N., Rico Pérez, V., Garcia-Garcia, A., Lozano-Castello, D., & Bueno López, A. (2012). Three-way catalysts: past, present and future. *Dyna*, Edition special, 79, 114-121.

Guo, X., Traitangwong, A., Hu, M., Zuo, C., Meeyoo, V., Peng, Z., & Li, C. (2018). Carbon dioxide methanation over nickel-based catalysts supported on various mesoporous material. *Energy & Fuels*, *32*(3), 3681-3689.

Gupta, V., & Saleh, T. A. (2011). Syntheses of carbon nanotube-metal oxides composites; adsorption and photo-degradation. *Carbon Nanotubes-From Research to Applications*, *17*, 295-312.

Hamzaçebi, C., Li, P., Pereira, P., & Navas, H. (2020). Taguchi method as a robust design tool. *Quality Control-Intelligent Manufacturing, Robust Design and Charts*, 1-19.

Haniyeh, F., Abdollah, A., & Abolghasem, D. (2013). Controlled growth of well-Aligned carbon nanotubes, electrochemical modification and electrodeposition of multiple shapes of gold nanostructures. *Materials Sciences and Applications*, 4 (11).

Harutyunyan, A. R., Tokune, T., Mora, E., Yoo, J.-W., & Epstein, A. J. (2006). Evolution of catalyst particle size during carbon single walled nanotube growth and its effect on the tube characteristics. *Journal of Applied Physics*, *100*(4).

Hayes, R., Thomas, W., & Hayes, K. (1985). A study of the nickel-catalyzed methanation reaction. *Journal of Catalysis*, *92*(2), 312-326.

He, C., Zhao, N., Du, X., Shi, C., Li, J., & He, F. (2008). Characterization of bamboo-shaped CNTs prepared using deposition-precipitation catalyst. *Materials Science and Engineering: A*, *479*(1-2), 248-252.

Hong Phuong, P., Cam Anh, H., Tri, N., Phung Anh, N., & Cam Loc, L. (2022). Effect of support on stability and coke resistance of ni-based catalyst in combined steam and CO_2 reforming of CH_4. *ACS Omega*, *7*(23), 20092-20103.

Hosseini, S., Moghaddas, H., Soltani, S. M., & Kheawhom, S. (2020). Technological applications of honeycomb monoliths in environmental processes: a review. *Process Safety and Environmental Protection*, *133*, 286-300.

Hu, F., Chen, X., Tu, Z., Lu, Z.-H., Feng, G., & Zhang, R. (2021). Graphene aerogel supported Ni for CO_2 hydrogenation to methane. *Industrial & Engineering Chemistry Research*, *60*(33), 12235-12243.

Hu, F., Tong, S., Lu, K., Chen, C. M., Su, F. Y., Zhou, J., Lu, Z. H., Wang, X., Feng, G., & Zhang, R. (2019). Reduced graphene oxide supported Ni-Ce catalysts for CO_2 methanation: The support and ceria promotion effects. *Journal of CO_2 Utilization*, *34*, 676-687.

Hu, X. F., Yang, W., Wang, N., Luo, S. Z., & Chu, W. (2014). Catalytic properties of Ni/CNTs and Ca-promoted Ni/CNTs for methanation reaction of carbon dioxide. *Advanced Materials Research*, 924, 217-226.

Hussain, M. M., Rahman, M. M., & Asiri, A. M. (2017). Ultra sensitive and selective 4-aminophenol chemical sensor development based on nickel oxide nanoparticles decorated carbon nanotube nanocomposites for green environment. *Journal of Environmental Sciences*, *53*, 27-38.

Huynh, H. L., Tucho, W. M., Yu, X., & Yu, Z. (2020). Synthetic natural gas production from CO_2 and renewable H_2: Towards large-scale production of Ni-Fe alloy catalysts for commercialization. *Journal of Cleaner Production*, *264*, 121720.

Huynh, T. M., Nguyen, S., Nguyen, N. T. K., Nguyen, H. M., Do, N. U. P., Nguyen, D. C., Nguyen, L. H., & Nguyen, C. V. (2021). Effects of catalyst pretreatment on carbon nanotube synthesis from methane using thin stainless-steel foil as catalyst by chemical vapor deposition method. *Nanomaterials*, *11*(1), 50.

Iijima, S. (1991). Synthesis of carbon nanotubes. *Nature*, *354*(6348), 56-58.
Ilnicka, A., & Lukaszewicz, J. P. (2019). Alternative synthesis method for carbon nanotubes. *Small*, *15*(51), 1904132.

Iroegbu, A. O., & Hlangothi, S. P. (2019). Furfuryl alcohol a versatile, eco-sustainable compound in perspective. *Chemistry Africa*, 1-17.

Jaffar, M. M., Nahil, M. A., & Williams, P. T. (2019). Parametric study of CO_2 methanation for synthetic natural gas production. *Energy Technology*, *7*(11), 1900795.

Jašek, O., Synek, P., Zajíčková, L., Eliáš, M., & Kudrle, V. (2010). Synthesis of carbon nanostructures by plasma enhanced chemical vapour deposition at atmospheric pressure. *Journal of Electrical Engineering*, *61*(5), 311-313.

Jurca, B., Bucur, C., Primo, A., Concepción, P., Parvulescu, V. I., & García, H. (2019). N-doped defective graphene from biomass as catalyst for CO_2 hydrogenation to methane. *ChemCatChem*, *11*(3), 985-990.

Kamalakar, G., Hwang, D. W., & Hwang, L. P. (2002). Synthesis and characterization of multiwalled carbon nanotubes produced using zeolite Co-beta. *Journal of Materials Chemistry*, *12*(6), 1819-1823.

Kang, D. Y., & Moon, J. H. (2014). Carbon nanotube balls and their application in supercapacitors. *ACS Applied Materials & Interfaces*, *6*(1), 706-711.

Kattel, S., Yan, B., Chen, J. G., & Liu, P. (2016). CO_2 hydrogenation on Pt, Pt/SiO_2 and Pt/TiO_2: Importance of synergy between Pt and oxide support. *Journal of Catalysis*, *343*, 115-126.

Kim, A. (2016). Nanostructured Ru/TiO_2 catalysts for CO_2 methanation. PhD Thesis.

Kirchner, J., Anolleck, J. K., Lösch, H., & Kureti, S. (2018). Methanation of CO_2 on iron-based catalysts. *Applied Catalysis B: Environmental*, *223*, 47-59.

Koji, H., Furuta, H., Sekiya, K., Nitta, N., Harigai, T., & Hatta, A. (2013). Increased CNT growth density with an additional thin Ni layer on the Fe/Al catalyst film. *Diamond and Related Materials*, *36*, 1-7.

Koschany, F., Schlereth, D., & Hinrichsen, O. (2016). On the kinetics of the methanation of carbon dioxide on coprecipitated $NiAl(O)_x$. *Applied Catalysis B: Environmental*, *181*, 504-516.

Krawczyk, K., Młotek, M., Ulejczyk, B., & Schmidt-Szałowski, K. (2014). Methane conversion with carbon dioxide in plasma-catalytic system. *Fuel*, *117*, 608-617.

Kumar, M., & Ando, Y. (2010). Chemical vapor deposition of carbon nanotubes: a review on growth mechanism and mass production. *Journal of Nanoscience and Nanotechnology*, *10*(6), 3739-3758.

Kumar, M., & Ando, Y. (2011). Carbon nanotube synthesis and growth mechanism. *Carbon Nanotubes-Synthesis, Characterization, Applications*, 147-170.

Kumar, U., & Yadav, B. (2019). Synthesis of carbon nanotubes by direct liquid injection chemical vapor deposition method and its relevance for developing an ultra-sensitive room temperature based CO_2 sensor. *Journal of the Taiwan Institute of Chemical Engineers*, *96*, 652-663.

Kuznecova, I., & Gusca, J. (2017). Property based ranking of CO and CO_2 methanation catalysts. *Energy Procedia*, *128*, 255-260.

Kwak, J. H., Kovarik, L., & Szanyi, J. (2013). Heterogeneous catalysis on atomically dispersed supported metals: CO_2 reduction on multifunctional Pd catalysts. *ACS Catalysis*, *3*(9), 2094-2100.

Lalinde, J. A. H., Roongruangsree, P., Ilsemann, J., Baeumer, M., & Kopyscinski, J. (2020). CO_2 methanation and reverse water gas shift reaction. Kinetic study based on in situ spatially-resolved measurements. *Chemical Engineering Journal*, *390*, 124629.

Lamme, W. S., Zečević, J., & de Jong, K. P. (2018). Influence of metal deposition and activation method on the structure and performance of carbon nanotube supported palladium catalysts. *ChemCatChem*, *10*(7), 1552-1555.

Lechkar, A., Bogeat, A. B., Blanco, G., Pintado, J. M., & el Begrani, M. S. (2018). Methanation of carbon dioxide over ceria-praseodymia promoted Ni-alumina catalysts. Influence of metal loading, promoter composition and alumina modifier. *Fuel*, *234*, 1401-1413.

Lee, C. J., Park, J., & Jeong, A. Y. (2002). Catalyst effect on carbon nanotubes synthesized by thermal chemical vapor deposition. *Chemical Physics Letters*, *360*(3-4), 250-255.

Lee, M. W., Haniff, M. A. S. M., Teh, A. S., Bien, D. C., & Chen, S. K. (2015). Effect of Co and Ni nanoparticles formation on carbon nanotubes growth via PECVD. *Journal of Experimental Nanoscience*, *10*(16), 1232-1241.

Lee, S. Y., Kim, S. J., Lee, W. J., & Lee, Y. K. (2021). Boosting activity and durability of an electrodeposited Ni (OH) 2 catalyst using carbon nanotube-grafted substrates for the alkaline oxygen evolution reaction. *ACS Applied Nano Materials*, *4*(10), 10267-10274.

Li, J., Zhou, Y., Xiao, X., Wang, W., Wang, N., Qian, W., & Chu, W. (2018). Regulation of Ni-CNT interaction on Mn-promoted nickel nanocatalysts supported on oxygenated CNTs for CO_2 selective hydrogenation. *ACS Applied Materials & Interfaces*, *10*(48), 41224-41236.

Li, L., Zeng, W., Song, M., Wu, X., Li, G., & Hu, C. (2022). Research progress and reaction mechanism of CO_2 methanation over Ni-based catalysts at low temperature: a review. *Catalysts*, *12*(2), 244.

Li, M., Li, Z., Lin, Q., Cao, J., Liu, F., & Kawi, S. (2022). Synthesis strategies of carbon nanotube supported and confined catalysts for thermal catalysis. *Chemical engineering journal*, *431*, 133970.

Li, P., Deng, G., Guo, X., Liu, H., Jiang, W., & Li, F. (2016). Preparation of nickel and Ni_3Sn nanoparticles via extension of conventional citric acid and ethylene diamine tetraacetic acid mediated solgel method. *Journal of Alloys and Compounds*, *668*, 159-168.

Li, Q., Yan, H., Zhang, J., & Liu, Z. (2004). Effect of hydrocarbons precursors on the formation of carbon nanotubes in chemical vapor deposition. *Carbon*, *42*(4), 829-835.

Liang, J., Wu, Z., Lei, H., Xi, X., Li, T., & Du, G. (2017). The reaction between furfuryl alcohol and model compound of protein. *Polymers*, *9*(12), 711.

Lin, J., Yang, Y., Zhang, H., Li, F., Huang, G., & Wang, J. (2020). Effect of catalyst on carbon nanotubes synthesis on titanium diboride via chemical vapor deposition. *Journal of the American Ceramic Society*, *103*(8), 4691-4699.

Lin, J., Yang, Y., Zhang, H., Lin, Q., & Zhu, B. (2018). Synthesis and characterization of in-situ CNTs reinforced TiB_2-based composite by CVD using Ni catalysts. *Ceramics International*, *44*(2), 2042-2047.

Liu, X., Su, D. S., & Schlögl, R. (2008). Oxidative dehydrogenation of 1-butene to butadiene over carbon nanotube catalysts. *Carbon*, *46*, 547-549.

Liu, Y., Ba, H., Nguyen, D.-L., Ersen, O., Romero, T., Zafeiratos, S., Begin, D., Janowska, I., & Pham-Huu, C. (2013). Synthesis of porous carbon nanotubes foam composites with a high accessible surface area and tunable porosity. *Journal of Materials Chemistry A*, *1*(33), 9508-9516.

Liu, Y., Yang, Y., Sun, Q., Wang, Z., Huang, B., Dai, Y., Qin, X., & Zhang, X. (2013). Chemical adsorption enhanced CO_2 capture and photoreduction over a copper porphyrin based metal organic framework. *ACS Applied Materials & Interfaces*, *5*(15), 7654-7658.

Long, N. V. D., Lee, J., Koo, K. K., Luis, P., & Lee, M. (2017). Recent progress and novel applications in enzymatic conversion of carbon dioxide. *Energies*, *10*(4), 473.

Lv, C., Xu, L., Chen, M., Cui, Y., Wen, X., Li, Y., Wu, C.-e., Yang, B., Miao, Z., & Hu, X. (2020). Recent progresses in constructing the highly efficient Ni based catalysts with advanced low-temperature activity toward CO2 methanation. *Frontiers in Chemistry*, *8*, 269.

Ma, Y., Lu, N., Lu, Y., Guan, J., Qu, J., Liu, H., Cong, Q., & Yuan, X. (2016). Comparative study of carbon materials synthesized “greenly” for 2-CP removal. *Scientific Reports*, *6*, 29167.

Mai, P. P. T., Tien, N. T., Le Minh, T., & Van Driessche, I. (2015). The application of high surface area cordierite synthesized from kaolin as a substrate for auto exhaust catalysts. *Journal of the Chinese Chemical Society*, *62*(6), 536-546.

Malekbala, M. R., Soltani, S., Rashid, S. A., Abdullah, L. C., & Choong, T. S. Y. (2019). Study the effect of various wash-coated metal oxides over synthesized carbon nanofibers coated monolith substrates. *PloS one*, *14*(7).

Mansor, N. A., Tessonnier, J.-P., Rinaldi, A., Reiche, S., & Kutty, M. (2012). Chemically modified multi-walled carbon nanotubes (MWCNTs) with anchored acidic groups. *Sains Malays*, *41*(5), 603-609.

Marchand, P., Hassan, I. A., Parkin, I. P., & Carmalt, C. J. (2013). Aerosol-assisted delivery of precursors for chemical vapour deposition: expanding the scope of CVD for materials fabrication. *Dalton Transactions*, *42*(26), 9406-9422.

Markewitz, P., Kuckshinrichs, W., Leitner, W., Linssen, J., Zapp, P., Bongartz, R., Schreiber, A., & Müller, T. E. (2012). Worldwide innovations in the development of carbon capture technologies and the utilization of CO_2. *Energy & Environmental Science*, *5*(6), 7281-7305.

Marocco, P., Morosanu, E. A., Giglio, E., Ferrero, D., Mebrahtu, C., Lanzini, A., Abate, S., Bensaid, S., Perathoner, S., & Santarelli, M. (2018). CO_2 methanation over Ni/Al hydrotalcite-derived catalyst: Experimental characterization and kinetic study. *Fuel*, *225*, 230-242.

Martínez, J., Hernández, E., Alfaro, S., López Medina, R., Valverde Aguilar, G., Albiter, E., & Valenzuela, M. A. (2018). High selectivity and stability of nickel catalysts for CO_2 methanation: support effects. *Catalysts*, *9*(1), 24.

Maruyama, S., Kojima, R., Miyauchi, Y., Chiashi, S., & Kohno, M. (2002). Low-temperature synthesis of high-purity single-walled carbon nanotubes from alcohol. *Chemical Physics Letters*, *360*(3-4), 229-234.

Meloni, E., Martino, M., & Palma, V. (2020). A short review on Ni based catalysts and related engineering issues for methane steam reforming. *Catalysts*, *10*(3), 352.

Mierczynski, P., Shtyka, O., Kozanecki, M., Filipczak, P., Maniukiewicz, W., Gromov, D. G., Dubkov, S. V., Sysa, A. V., Trifonov, A. Y., & Czylkowska, A. (2020). Effect of the AACVD based synthesis atmosphere on the structural properties of multi-walled carbon nanotubes. *Arabian Journal of Chemistry*, *13*(1), 835-850.

Miguel, C. V., Mendes, A., & Madeira, L. M. (2018). Intrinsic kinetics of CO_2 methanation over an industrial nickel-based catalyst. *Journal of CO_2 Utilization*, *25*, 128-136.

Minett, D. R., O'Byrne, J. P., Jones, M. D., Ting, V. P., Mays, T. J., & Mattia, D. (2013). One-step production of monolith-supported long carbon nanotube arrays. *Carbon*, *51*, 327-334.

Ming, H., Peiling, D., Yunlong, Z., Jing, G., & Xiaoxue, R. (2016). Effect of reaction temperature on carbon yield and morphology of CNTs on copper loaded nickel nanoparticles. *Journal of Nanomaterials*, *2016*.

Mittal, G., & Rhee, K. Y. (2018a). Chemical vapor deposition-based grafting of CNTs onto basalt fabric and their reinforcement in epoxy-based composites. *Composites Science and Technology*, *165*, 84-94.

Mittal, G., & Rhee, K. Y. (2018b). Hierarchical structures of CNT@ basalt fabric for tribological and electrical applications: impact of growth temperature and time during synthesis. *Composites Part A: Applied Science and Manufacturing*, *115*, 8-21.

Mohamed, A. R., Abdullah, A. Z., & Chai, S. P. (2010). Role of reaction and factors of carbon nanotubes growth in chemical vapour decomposition process using Methane: a highlight. *Journal of Nanomaterials*, *11, 1-11.*

Mohamed Saheed, M. S., Mohamed, N. M., & Burhanudin, Z. A. (2014). Effect of different catalyst deposition technique on aligned multiwalled carbon nanotubes grown by thermal chemical vapor deposition. *Journal of Nanomaterials*, *2014*, 707301.

Mohd Ridzuan, N. D., Shaharun, M. S., Anawar, M. A., & Ud-Din, I. (2022). Ni-based catalyst for carbon dioxide methanation: A review on performance and progress. *Catalysts*, *12*(5), 469.

Mohd Ridzuan, N. D., Shaharun, M. S., Lee, K. M., Ud Din, I., & Puspitasari, P. (2020). Influence of nickel loading on reduced graphene oxide-based nickel catalysts for the hydrogenation of carbon dioxide to methane. *Catalysts*, *10*(5), 471.

Moioli, E., & Züttel, A. (2020). A model-based comparison of Ru and Ni catalysts for the Sabatier reaction. *Sustainable Energy & Fuels*, *4*(3), 1396-1408.

Moonngam, S., Tunjina, P., Deesom, D., & Banjongprasert, C. (2016). Fe-Cr/CNTs nanocomposite feedstock powders produced by chemical vapor deposition for thermal spray coatings. *Surface and Coatings Technology*, *306*, 323-327.

Moreno-Castilla, C., & Pérez-Cadenas, A. F. (2010). Carbon-based honeycomb monoliths for environmental gas-phase applications. *Materials*, *3*(2), 1203-1227.

Müller, K., Fleige, M., Rachow, F., & Schmeißer, D. (2013). Sabatier based CO_2 methanation of flue gas emitted by conventional power plants. *Energy Procedia*, *40*, 240-248.

Munajad, A., & Subroto, C. (2018). Fourier transform infrared (FTIR) spectroscopy analysis of transformer paper in mineral oil-paper composite insulation under accelerated thermal aging. *Energies*, *11*(2), 364.

Muroyama, H., Tsuda, Y., Asakoshi, T., Masitah, H., Okanishi, T., Matsui, T., & Eguchi, K. (2016). Carbon dioxide methanation over Ni catalysts supported on various metal oxides. *Journal of Catalysis*, *343*, 178-184.

Mutz, B., Gänzler, A. M., Nachtegaal, M., Müller, O., Frahm, R., Kleist, W., & Grunwaldt, J. D. (2017). Surface oxidation of supported Ni particles and its impact on the catalytic performance during dynamically operated methanation of CO_2. *Catalysts*, *7*(9), 279.

Nagaraju, N., Fonseca, A., Konya, Z., & Nagy, J. B. (2002). Alumina and silica supported metal catalysts for the production of carbon nanotubes. *Journal of Molecular Catalysis A: Chemical*, *181*(1-2), 57-62.

Nanaji, K., Jyothirmayi, A., Varadaraju, U., Rao, T. N., & Anandan, S. (2017). Facile synthesis of mesoporous carbon from furfuryl alcohol-butanol system by EISA process for supercapacitors with enhanced rate capability. *Journal of Alloys and Compounds*, *723*, 488-497.

Navas, H., Picher, M., Andrieux-Ledier, A., Fossard, F. d. r., Michel, T., Kozawa, A., Maruyama, T., Anglaret, E., Loiseau, A., & Jourdain, V. (2017). Unveiling the evolutions of nanotube diameter distribution during

the growth of single-walled carbon nanotubes. *ACS Nano*, *11*(3), 3081-3088.

Nguyen, V. H., Nguyen, T. D., Bach, L. G., Hoang, T., Bui, Q. T. P., Tran, L. D., Nguyen, C. V., Vo, D. V. N., & Do, S. T. (2018). Effective photocatalytic activity of mixed Ni/Fe-base metal-organic framework under a compact fluorescent daylight lamp. *Catalysts*, *8*(11), 487.

Neupane, S. (2014). Synthesis and electron emission properties of aligned carbon nanotube arrays. PhD Thesis.

Nie, W., Zou, X., Chen, C., Wang, X., Ding, W., & Lu, X. (2017). Methanation of carbon dioxide over Ni-Ce-Zr oxides prepared by one-pot hydrolysis of metal nitrates with ammonium carbonate. *Catalysts*, *7*(4), 104.

Nijhuis, T. A., Beers, A. E., Vergunst, T., Hoek, I., Kapteijn, F., & Moulijn, J. A. (2001). Preparation of monolithic catalysts. *Catalysis Reviews*, *43*(4), 345-380.

Ocampo, F., Louis, B., & Roger, A.-C. (2009). Methanation of carbon dioxide over nickel-based $CeO_{72}ZrO_{28}O_2$ mixed oxide catalysts prepared by sol-gel method. *Applied Catalysis A: General*, *369*(1-2), 90-96.

Ogura, K. (2013). Electrochemical reduction of carbon dioxide to ethylene: mechanistic approach. *Journal of CO_2 Utilization*, *1*, 43-49.

Olivares, A. C. V., Gomez, M. F., Barroso, M. N., & Abello, M. C. (2018). Ni-supported catalysts for ethanol steam reforming: effect of the solvent and metallic precursor in catalyst preparation. *International Journal of Industrial Chemistry*, *9*, 61-73.

Onrubia-Calvo, J. A., Quindimil, A., Davó-Quiñonero, A., Bermejo-López, A., Bailón-García, E., Pereda-Ayo, B. a., Lozano-Castelló, D., González-Marcos, J. A., Bueno-López, A., & González-Velasco, J. R. (2022). Kinetics, model discrimination, and parameters estimation of CO_2 methanation on highly active Ni/CeO_2 Catalyst. *Industrial & Engineering Chemistry Research*, *61*(29), 10419-10435.

Osman, A. I., Farrell, C., Ala'a, H., Harrison, J., & Rooney, D. W. (2020). the production and application of carbon nanomaterials from high alkali silicate herbaceous biomass. *Scientific Reports*, *10*(1), 1-13.

Ouhaddouch, H., Cheikh, A., Idrissi, M., Draoui, M., & Bouatia, M. (2019). FTIR spectroscopy applied for identification of a mineral drug substance in drug products: application to bentonite. *Journal of Spectroscopy*, *2019*.

Ozdemir, A., & Ark, M. (2009). Rho Kinase and Apoptosis. *Mersin University J Health Sci*, *2*, 1-9.

Pan, Q., Peng, J., Sun, T., Wang, S., & Wang, S. (2014). Insight into the reaction route of CO_2 methanation: Promotion effect of medium basic sites. *Catalysis Communications*, *45*, 74-78.

Park, J. N., & McFarland, E. W. (2009). A highly dispersed Pd-Mg/SiO_2 catalyst active for methanation of CO_2. *Journal of Catalysis*, *266*(1), 92-97.

Park, J. B., Jeong, M. S., & Jeong, S. H. (2009). Rapid growth of carbon nanotubes using laser-induced chemical vapor deposition. *In International Laser Safety Conference*, *AIP Publishing*, 1367-1370.

Pastor-Pérez, L., Patel, V., Le Saché, E., & Reina, T. (2020). CO_2 methanation in the presence of methane: catalysts design and effect of methane concentration in the reaction mixture. *Journal of the Energy Institute*, *93*(1), 415-424.

Pham, Q. N., Larkin, L. S., Lisboa, C. C., Saltonstall, C. B., Qiu, L., Schuler, J. D., Rupert, T. J., & Norris, P. M. (2017). Effect of growth temperature on the synthesis of carbon nanotube arrays and amorphous carbon for thermal applications. *Physica Status Solidi (a)*, *214*(7), 1600852.

Ping, D., Wang, C., Dong, X., & Dong, Y. (2016). Co-production of hydrogen and carbon nanotubes on nickel foam via methane catalytic decomposition. *Applied Surface Science*, *369*, 299-307.

Porta, A., Falbo, L., Visconti, C. G., Lietti, L., Bassano, C., & Deiana, P. (2020). Synthesis of Ru-based catalysts for CO_2 methanation and experimental assessment of intraporous transport limitations. *Catalysis Today*, *343*, 38-47.

Primo, A., He, J., Jurca, B., Cojocaru, B., Bucur, C., Parvulescu, V. I., & Garcia, H. (2019). CO_2 methanation catalyzed by oriented MoS2 nanoplatelets supported on few layers graphene. *Applied Catalysis B: Environmental*, *245*, 351-359.

Purohit, R., Purohit, K., Rana, S., Rana, R., & Patel, V. (2014). Carbon nanotubes and their growth methods. *Procedia Materials Science*, *6*, 716-728.

Qi, W., Liu, W., Zhang, B., Gu, X., Guo, X., & Su, D. (2013). Oxidative dehydrogenation on nanocarbon: identification and quantification of active sites by chemical titration. *Angewandte Chemie International Edition*, *52*(52), 14224-14228.

Rahmani, S., Meshkani, F., & Rezaei, M. (2019). Preparation of Ni-M (M: La, Co, Ce, and Fe) catalysts supported on mesoporous nanocrystalline γ-Al_2O_3 for CO_2 methanation. *Environmental Progress & Sustainable Energy*, *38*(1), 118-126.

Rahmani, S., Rezaei, M., & Meshkani, F. (2014). Preparation of highly active nickel catalysts supported on mesoporous nanocrystalline γ-Al_2O_3 for CO_2 methanation. *Journal of Industrial and Engineering Chemistry*, *20*(4), 1346-1352.

Rahmani, S., Rezaei, M., & Meshkani, F. (2016). A comparative study on the kinetics of carbon dioxide methanation over bimetallic and monometallic catalysts. *Iranian Journal of Hydrogen & Fuel Cell*, *3*(1), 59-71.

Rakić, V. M., Dondur, V. T., & Hercigonja, R. V. (2003). FTIR study of carbon monoxide adsorption on ion-exchanged X, Y and mordenite type zeolites. *Journal of the Serbian Chemical Society*, *68*(4-5), 409-416.

Ramírez Rodríguez, F., López, B. L., & Giraldo, L. F. (2018). Single wall carbon nanotubes synthesis through methane chemical vapor deposition over MCM-41-Co catalysts: variables optimization. *C Journal of Carbon Research*, *4*(2), 37.

Ren, J., Qin, X., Yang, J. Z., Qin, Z. F., Guo, H. L., Lin, J. Y., & Li, Z. (2015). Methanation of carbon dioxide over Ni-M/ZrO_2 (M= Fe, Co, Cu) catalysts: Effect of addition of a second metal. *Fuel Processing Technology*, *137*, 204-211.

Ren, Y., Ma, Y. Y., Mo, W. L., Guo, J., Liu, Q., Fan, X., & Zhang, S. P. (2023). Research Progress of Carbon Deposition on Ni-Based Catalyst for CO_2-CH_4 Reforming. *Catalysts*, *13*(4), 647.

Rocha, R. P., Pereira, M. F. R., & Figueiredo, J. L. (2023). Characterisation of the surface chemistry of carbon materials by temperature-programmed desorption: An assessment. *Catalysis Today*, 418, 114136.

Rodrigues, T. S., da Silva, A. G., & Camargo, P. H. (2019). Nanocatalysis by noble metal nanoparticles: controlled synthesis for the optimization and understanding of activities. *Journal of Materials Chemistry A*, *7*(11), 5857-5874.

Romero-Sáez, M., Dongil, A., Benito, N., Espinoza-González, R., Escalona, N., & Gracia, F. (2018). CO_2 methanation over nickel-ZrO_2 catalyst supported on carbon nanotubes: A comparison between two impregnation strategies. *Applied Catalysis B: Environmental*, *237*, 817-825.

Ross, M. B., De Luna, P., Li, Y., Dinh, C. T., Kim, D., Yang, P., & Sargent, E. H. (2019). Designing materials for electrochemical carbon dioxide recycling. *Nature Catalysis*, *2*(8), 648-658.

Ross, P. J. (1996). Taguchi techniques for quality engineering: loss function, orthogonal experiments, parameter and tolerance design, 2nd edition McGraw-Hill Professional: New York, 208-212.

Roy, S., Bauer, T., Al-Dahhan, M., Lehner, P., & Turek, T. (2004). Monoliths as multiphase reactors: a review. *AIChE Journal*, *50*(11), 2918-2938.

Sagu, J. S., Upul Wijayantha, K. G., Bohm, M., Bohm, S., & Rout, T. K. (2016). Aerosol-assisted chemical vapor deposition of multi-walled carbon nanotubes on steel substrates for application in supercapacitors. *Advanced Engineering Materials*, *18*(6), 1059-1065.

Saravanakkumar, D., Karthika, R., Ganasaravanan, S., Sivaranjani, S., Pandiarajan, S., Ravikumar, B., & Ayeshamariam, A. (2018). Synthesis of NiO doped ZnO/MWCNT nanocomposite and its charecterization for photocatalytic & antimicrobial applications. *IOSR Journal of Applied Physics*, *10*(3), 73-83.

Schaaf, T., Grünig, J., Schuster, M. R., Rothenfluh, T., & Orth, A. (2014). Methanation of CO_2 storage of renewable energy in a gas distribution system. *Energy, Sustainability and Society*, *4*(1), 1-14.

Schmider, D., Maier, L., & Deutschmann, O. (2021). Reaction kinetics of CO and CO_2 methanation over nickel. *Industrial & Engineering Chemistry Research*, *60*(16), 5792-5805.

Schneider, S. H. (1989). The greenhouse effect: science and policy. *Science*, *243*(4892), 771-781.

Sehested, J., Gelten, J. A., Remediakis, I. N., Bengaard, H., & Nørskov, J. K. (2004). Sintering of nickel steam-reforming catalysts: effects of temperature and steam and hydrogen pressures. *Journal of Catalysis*, *223*(2), 432-443.

Sentek, J., Krawczyk, K., Młotek, M., Kalczewska, M., Kroker, T., Kolb, T., Schenk, A., Gericke, K. H., & Schmidt-Szałowski, K. (2010). Plasma-catalytic methane conversion with carbon dioxide in dielectric barrier discharges. *Applied Catalysis B: Environmental*, *94*(1-2), 19-26.

Serp, P., Kalck, P., & Feurer, R. (2002). Chemical vapor deposition methods for the controlled preparation of supported catalytic materials. *Chemical reviews*, *102*(9), 3085-3128.

Shah, K. A., Najar, F. A., Sharda, T., & Sreenivas, K. (2018). Synthesis of multi-walled carbon nanotubes by thermal CVD technique on Pt-W-MgO catalyst. *Journal of Taibah University for Science*, *12*(2), 230-234.

Shahriary, L., & Athawale, A. A. (2014). Graphene oxide synthesized by using modified hummers approach. *International Journal of Renewable Energy and Environmental Engineering*, *2*(1), 58-63.

Shanmugam, V., Neuberg, S., Zapf, R., Pennemann, H., & Kolb, G. (2020). Effect of support and chelating ligand on the synthesis of Ni catalysts with high activity and stability for CO_2 methanation. *Catalysts*, *10*(5), 493.

Shi, J., Jiang, Y., Jiang, Z., Wang, X., Wang, X., Zhang, S., Han, P., & Yang, C. (2015). Enzymatic conversion of carbon dioxide. *Chemical Society Reviews*, *44*(17), 5981-6000.

Shukrullah, S., Mohamed, N., Khan, Y., Naz, M., Ghaffar, A., & Ahmad, I. (2017). Effect of gas flowrate on nucleation mechanism of MWCNTs for a compound catalyst. *Journal of Nanomaterials*, 2017.

Shukrullah, S., Naz, M., Mohamed, N., Ibrahim, K., Ghaffar, A., & Abdel-Salam, N. (2019). Production of bundled CNTs by floating a compound catalyst in an atmospheric pressure horizontal CVD reactor. *Results in Physics*, *12*, 1163-1171.

Singh, B., Strømman, A. H., & Hertwich, E. (2011). Life cycle assessment of natural gas combined cycle power plant with post-combustion carbon capture, transport and storage. *International Journal of Greenhouse Gas Control*, *5*(3), 457-466.

Slater, T. J., Macedo, A., Schroeder, S. L., Burke, M. G., O'Brien, P., Camargo, P. H., & Haigh, S. J. (2014). Correlating catalytic activity of Ag-Au nanoparticles with 3D compositional variations. *Nano letters*, *14*(4), 1921-1926.

Soghrati, E., Kazemeini, M., Rashidi, A., & Jozani, K. J. (2014). Development of a structured monolithic support with a CNT washcoat for the naphtha HDS process. *Journal of the Taiwan Institute of Chemical Engineers*, *45*(3), 887-895.

Sollier, B. M., Gómez, L. E., Boix, A. V., & Miró, E. E. (2018). Oxidative coupling of methane on cordierite monoliths coated with Sr/La_2O_3 catalysts. Influence of honeycomb structure and catalyst-cordierite chemical interactions on the catalytic behavior. *Applied Catalysis A: General*, *550*, 113-121.

Songolzadeh, M., Ravanchi, M. T., & Soleimani, M. (2012). Carbon dioxide capture and storage: a general review on adsorbents. *International Journal of Chemical and Molecular Engineering*, 6(10).

Stangeland, K., Kalai, D., Li, H., & Yu, Z. (2017). CO_2 methanation: the effect of catalysts and reaction conditions. *Energy Procedia*, *105*, 2022-2027.

Su, R. (2015). Multi-field physics for the synthesis of carbon nanotube yarn and sheet. PhD Thesis.

Szulczewski, M. L., MacMinn, C. W., Herzog, H. J., & Juanes, R. (2012). Lifetime of carbon capture and storage as a climate-change mitigation technology. *Proceedings of the National Academy of Sciences*, *109*(14), 5185-5189.

Tada, S., Shimizu, T., Kameyama, H., Haneda, T., & Kikuchi, R. (2012). Ni/CeO_2 catalysts with high CO_2 methanation activity and high CH_4 selectivity at low temperatures. *International Journal of Hydrogen Energy*, *37*(7), 5527-5531.

Takenaka, S., Shimizu, T., & Otsuka, K. (2004). Complete removal of carbon monoxide in hydrogen-rich gas stream through methanation over supported metal catalysts. *International Journal of Hydrogen Energy*, *29*(10), 1065-1073.

Taleshi, F. (2012). Evaluation of new processes to achieve a high yield of carbon nanotubes by CVD method. *International Nano Letters*, *2*(1), 23.

Tan, C. H., Nomanbhay, S., Shamsuddin, A. H., Park, Y.-K., Hernández-Cocoletzi, H., & Show, P. L. (2022). Current developments in catalytic methanation of carbon dioxide: a review. *Frontiers in Energy Research*, *9*, 795423.

Tang, Y., Cao, S., Chen, Y., Bao, J., & Lu, T. (2007). Effect of structure of carbon nanotubes on electrocatalytic performance of carbon nanotubes supported Pt catalysts. *Chemical Journal of Chinese Universities*, *28*, 936-939.

Tee, J. C., Aziz, M., & Ismail, A. F. (2009). Effect of reaction temperature and flow rate of precursor on formation of multi-walled carbon nanotubes. *AIP Conference Proceedings*, *1136*(1).

Thambiliyagodage, C. J., Ulrich, S., Araujo, P., & Bakker, M. G. (2018). Catalytic graphitization in nanocast carbon monoliths by iron, cobalt and nickel nanoparticles. *Carbon*, *134*, 452-463.

Thommes, M., Kaneko, K., Neimark, A. V., Olivier, J. P., Rodriguez-Reinoso, F., Rouquerol, J., & Sing, K. S. (2015). Physisorption of gases, with special reference to the evaluation of surface area and pore size distribution (IUPAC Technical Report). *Pure and Applied Chemistry*, *87*(9-10), 1051-1069.

Tian, Z., Liu, C., Li, Q., Hou, J., Li, Y., & Ai, S. (2015). Nitrogen and oxygen-functionalized carbon nanotubes supported Pt-based catalyst for the selective hydrogenation of cinnamaldehyde. *Applied Catalysis A: General*, *506*, 134-142.

Toemen, S., Bakar, W. A. W. A., & Ali, R. (2014). Investigation of Ru/Mn/Ce/Al_2O_3 catalyst for carbon dioxide methanation: catalytic optimization, physicochemical studies and RSM. *Journal of the Taiwan Institute of Chemical Engineers*, *45*(5), 2370-2378.

Tondi, G., Link, M., Oo, C. W., & Petutschnigg, A. (2015). A simple approach to distinguish classic and formaldehyde-free tannin based rigid foams by ATR FT-IR. *Journal of Spectroscopy*, *2015*, 902340.

Toyir, J., de la Piscina, P. R. r., Fierro, J. L. G., & Homs, N. s. (2001). Highly effective conversion of CO_2 to methanol over supported and promoted copper-based catalysts: influence of support and promoter. *Applied Catalysis B: Environmental*, *29*(3), 207-215.

Tripathi, N., Mishra, P., Joshi, B., & Islam, S. (2014). Catalyst free, excellent quality and narrow diameter of CNT growth on Al_2O_3 by a thermal CVD technique. *Physica E: Low-dimensional Systems and Nanostructures*, *62*, 43-47.

Tsiotsias, A. I., Charisiou, N. D., Yentekakis, I. V., & Goula, M. A. (2020). Bimetallic Ni-based catalysts for CO_2 methanation: a review. *Nanomaterials*, *11*(1), 28.

Tu, J., Wu, H., Qian, Q., Han, S., Chu, M., Jia, S., Feng, R., Zhai, J., He, M., & Han, B. (2021). Low temperature methanation of CO_2 over an amorphous cobalt-based catalyst. *Chemical Science*, *12*(11), 3937-3943.

Tuckett, R. (2018). Greenhouse gases. *Reference Module in Chemistry, Molecular Sciences and Chemical Engineering*, 4, 362-372.

Ţucureanu, V., Matei, A., & Avram, A. M. (2016). FTIR spectroscopy for carbon family study. *Critical Reviews in Analytical Chemistry*, *46*(6), 502-520.

Upham, D. C., Derk, A. R., Sharma, S., Metiu, H., & McFarland, E. W. (2015). CO_2 methanation by Ru-doped ceria: the role of the oxidation state of the surface. *Catalysis Science & Technology*, *5*(3), 1783-1791.

Vasudev, M. C., Anderson, K. D., Bunning, T. J., Tsukruk, V. V., & Naik, R. R. (2013). Exploration of plasma-enhanced chemical vapor deposition as a method for thin-film fabrication with biological applications. *ACS Applied Materials & Interfaces*, *5*(10), 3983-3994.

Venkatesan, S., Visvalingam, B., Mannathusamy, G., Viswanathan, V., & Rao, A. G. (2018). Effect of chemical vapor deposition parameters on the diameter of multi-walled carbon nanotubes. *International Nano Letters*, *8*(4), 297-308.

Vergunst, T., Kapteijn, F., & Moulijn, J. (2002). Preparation of carbon-coated monolithic supports. *Carbon*, *40*(11), 1891-1902.

Verma, B., Sewani, H., & Balomajumder, C. (2020). Synthesis of carbon nanotubes via chemical vapor deposition: an advanced application in the management of electroplating effluent. *Environmental Science and Pollution Research*, 1-12.

Vidhya, M. S., Ravi, G., Yuvakkumar, R., Velauthapillai, D., Thambidurai, M., Dang, C., & Saravanakumar, B. (2020). Nickel–cobalt hydroxide: A positive electrode for supercapacitor applications. *Rsc Advances*, *10*(33), 19410-19418.

von der Assen, N., Jung, J., & Bardow, A. (2013). Life-cycle assessment of carbon dioxide capture and utilization: avoiding the pitfalls. *Energy & Environmental Science*, *6*(9), 2721-2734.

Vrijburg, W. L., Moioli, E., Chen, W., Zhang, M., Terlingen, B. J., Zijlstra, B., Filot, I. A., Zuttel, A., Pidko, E. A., & Hensen, E. J. (2019). Efficient base-metal $NiMn/TiO_2$ catalyst for CO_2 methanation. *ACS Catalysis*, *9*(9), 7823-7839.

Wang, F., Zhang, Y., Wang, Y., Luo, Y., Chen, Y., & Zhu, H. (2018). Co-P nanoparticles supported on dandelion-like CNTs-Ni foam composite carrier as a novel catalyst for hydrogen generation from $NaBH_4$ methanolysis. *International Journal of Hydrogen Energy*, *43*(18), 8805-8814.

Wang, K., Men, Y., Liu, S., Wang, J., Li, Y., Tang, Y., Li, Z., An, W., Pan, X., & Li, L. (2021). Decoupling the size and support/metal loadings effect of Ni/SiO_2 catalysts for CO_2 methanation. *Fuel*, *304*, 121388.

Wang, L., Liu, H., Ye, H., Hu, R., Yang, S., Tang, G., Li, K., & Yang, Y. (2018). Vacuum thermal treated $Ni\text{-}CeO_2$/SBA-15 catalyst for CO_2 Methanation. *Nanomaterials*, *8*(10), 759.

Wang, S., Lu, G., & Millar, G. J. (1996). Carbon dioxide reforming of methane to produce synthesis gas over metal-supported catalysts: state of the art. *Energy & Fuels*, *10*(4), 896-904.

Wang, W. N., Widiyastuti, W., Lenggoro, I. W., Kim, T. O., & Okuyama, K. (2007). Photoluminescence optimization of luminescent nanocomposites fabricated by spray pyrolysis of a colloid-solution precursor. *Journal of the Electrochemical Society*, *154*(4), J121.

Wang, W., Chu, W., Wang, N., Yang, W., & Jiang, C. (2016). Mesoporous nickel catalyst supported on multi-walled carbon nanotubes for carbon dioxide methanation. *International Journal of Hydrogen Energy*, *41*(2), 967-975.

Wang, W., Duong-Viet, C., Ba, H., Baaziz, W., Tuci, G., Caporali, S., Nguyen-Dinh, L., Ersen, O., Giambastiani, G., & Pham-Huu, C. (2018). Nickel nanoparticles decorated nitrogen-doped carbon nanotubes (Ni/N-CNT); a robust catalyst for the efficient and selective CO_2 methanation. *ACS Applied Energy Materials*, *2*(2), 1111-1120.

Wang, X., Li, Q., Pan, H., Lin, Y., Ke, Y., Sheng, H., Swihart, M. T., & Wu, G. (2015). Size-controlled large-diameter and few-walled carbon nanotube catalysts for oxygen reduction. *Nanoscale*, *7*(47), 20290-20298.

Ward, J., Wei, B., & Ajayan, P. (2003). Substrate effects on the growth of carbon nanotubes by thermal decomposition of methane. *Chemical Physics Letters*, *376*(5-6), 717-725.

Weatherbee, G. D., & Bartholomew, C. H. (1982). Hydrogenation of CO_2 on group VIII metals: II. Kinetics and mechanism of CO_2 hydrogenation on nickel. *Journal of Catalysis*, *77*(2), 460-472.

Weissker, U., Hampel, S., Leonhardt, A., & Büchner, B. (2010). Carbon nanotubes filled with ferromagnetic materials. *Materials*, *3*(8), 4387-4427.

Westermann, A., Azambre, B., Bacariza, M., Graça, I., Ribeiro, M., Lopes, J., & Henriques, C. (2015). Insight into CO_2 methanation mechanism over

NiUSY zeolites: an operando IR study. *Applied Catalysis B: Environmental*, *174*, 120-125.

Xiao, S., Sun, W., Du, J., & Li, G. (2014). Application of CFD, Taguchi method, and ANOVA technique to optimize combustion and emissions in a light duty diesel engine. *Mathematical Problems in Engineering*, *2014*, 502902.

Xie, D., Zheng, H., Li, Z., Tang, J., & Wei, Z. (2021). In-situ FTIR study of CO_2 adsorption and methanation mechanism over bimetallic catalyst at low temperature. *Catalysis Letters*, *151*(10), 2894-2905.

Xu, J., Lin, Q., Su, X., Duan, H., Geng, H., & Huang, Y. (2016). CO_2 methanation over TiO_2-Al_2O_3 binary oxides supported Ru catalysts. *Chinese Journal of Chemical Engineering*, *24*(1), 140-145.

Xu, L., Lian, X., Chen, M., Cui, Y., Wang, F., Li, W., & Huang, B. (2018). CO_2 methanation over CoNi bimetal-doped ordered mesoporous Al_2O_3 catalysts with enhanced low-temperature activities. *International Journal of Hydrogen Energy*, *43*(36), 17172-17184.

Yadav, M. D., Joshi, H. M., Sawant, S. V., Dasgupta, K., Patwardhan, A. W., & Joshi, J. B. (2023). Advances in the application of carbon nanotubes as catalyst support for hydrogenation reactions. *Chemical Engineering Science*, *272*, 118586.

Yahyazadeh, A., & Khoshandam, B. (2017). Carbon nanotube synthesis via the catalytic chemical vapor deposition of methane in the presence of iron, molybdenum, and iron-molybdenum alloy thin layer catalysts. *Results in physics*, *7*, 3826-3837.

Yang, Z. Z., He, L. N., Gao, J., Liu, A. H., & Yu, B. (2012). Carbon dioxide utilization with C-N bond formation: carbon dioxide capture and subsequent conversion. *Energy & Environmental Science*, *5*(5), 6602-6639.

Youn, J. R., Kim, M. J., Lee, S. J., Ryu, I. S., Yoon, H. C., Jeong, S. K., Lee, K., & Jeon, S. G. (2021). The influence of CNTs addition on Mn-Ce/TiO_2 catalyst for low-temperature NH_3-SCR of NO. *Catalysis Communications*, *152*, 106282.

Yu, Y., Chan, Y. M., Bian, Z., Song, F., Wang, J., Zhong, Q., & Kawi, S. (2018). Enhanced performance and selectivity of CO_2 methanation over g-C_3N_4 assisted synthesis of $NiCeO_2$ catalyst: Kinetics and DRIFTS studies. *International Journal of Hydrogen Energy*, *43*(32), 15191-15204.

Yuvaraj, S., Fan-Yuan, L., Tsong-Huei, C., & Chuin-Tih, Y. (2003). Thermal decomposition of metal nitrates in air and hydrogen environments. *The Journal of Physical Chemistry B*, *107*(4), 1044-1047.

Zahir, M. H., Rahman, M. M., Irshad, K., & Rahman, M. M. (2019). Shape-stabilized phase change materials for solar energy storage: MgO and Mg $(OH)_2$ mixed with polyethylene glycol. *Nanomaterials*, *9*(12), 1773.

Zamaniyan, A., Mortazavi, Y., Khodadadi, A. A., & Manafi, H. (2010). Tube fitted bulk monolithic catalyst as novel structured reactor for gas-solid reactions. *Applied Catalysis A: General*, *385*(1-2), 214-223.

Zhan, S., Tian, Y., Cui, Y., Wu, H., Wang, Y., Ye, S., & Chen, Y. (2007). Effect of process conditions on the synthesis of carbon nanotubes by catalytic decomposition of methane. *China Particuology*, *5*(3), 213-219.

Zhang, M., & Baughman, R. (2011). Assembly of carbon nanotube sheets. *Electronic Properties of Carbon Nanotubes*, 1-19.

Zhang, Z., Tian, Y., Zhang, L., Hu, S., Xiang, J., Wang, Y., Xu, L., Liu, Q., Zhang, S., & Hu, X. (2019). Impacts of nickel loading on properties, catalytic behaviors of Ni/γ–Al_2O_3 catalysts and the reaction intermediates formed in methanation of CO_2. *International Journal of Hydrogen Energy*, *44*(18), 9291-9306.

Zhang, Z., Verykios, X. E., MacDonald, S. M., & Affrossman, S. (1996). Comparative study of carbon dioxide reforming of methane to synthesis gas over Ni/La_2O_3 and conventional nickel-based catalysts. *The Journal of Physical Chemistry*, *100*(2), 744-754.

Zhao, T. T., Feng, G. H., Chen, W., Song, Y. F., Dong, X., Li, G. H., Zhang, H. J., & Wei, W. (2019). Artificial bioconversion of carbon dioxide. *Chinese Journal of Catalysis*, *40*(10), 1421-1437.

Zhao, Y., Girelli, V., Ersen, O., & Debecker, D. P. (2023). CO_2 methanation with high-loading mesoporous Ni/SiO_2 catalysts: toward high specific activity and new mechanistic insights. *Journal of Catalysis*, *426*, 283-293.

Zhao, Z., Zhang, L., Tan, Q., Yang, F., Faria, J., & Resasco, D. (2019). Synergistic bimetallic Ru-Pt catalysts for the low-temperature aqueous phase reforming of ethanol. *AIChE Journal*, *65*(1), 151-160.

Zhen, W., Li, B., Lu, G., & Ma, J. (2015). Enhancing catalytic activity and stability for CO_2 methanation on Ni@ MOF-5 via control of active species dispersion. *Chemical Communications*, *51*(9), 1728-1731.

Zhou, G., Liu, H., Cui, K., Jia, A., Hu, G., Jiao, Z., Liu, Y., & Zhang, X. (2016). Role of surface Ni and Ce species of Ni/CeO_2 catalyst in CO_2 methanation. *Applied Surface Science*, *383*, 248-252.

Zhou, L., Wang, Q., Ma, L., Chen, J., Ma, J., & Zi, Z. (2015). CeO_2 promoted mesoporous Ni/γ-Al_2O_3 catalyst and its reaction conditions for CO_2 methanation. *Catalysis Letters*, *145*(2), 612-619.

Zhu, M., Ge, Q., & Zhu, X. (2020). Catalytic reduction of CO_2 to co via reverse water gas shift reaction: recent advances in the design of active and selective supported metal catalysts. *Transactions of Tianjin University*, 1-16.

Zhu, M., Wang, J., Outlaw, R. A., Hou, K., Manos, D. M., & Holloway, B. C. (2007). Synthesis of carbon nanosheets and carbon nanotubes by radio frequency plasma enhanced chemical vapor deposition. *Diamond and Related Materials*, *16*(2), 196-201.

Zhu Y., Zhang, S., Ye, Y., Zhang, X., Wang, L., Zhu, W., Cheng, F., & Tao, F. (2012). Catalytic conversion of carbon dioxide to methane on ruthenium–cobalt bimetallic nanocatalysts and correlation between surface chemistry of catalysts under reaction conditions and catalytic performances. *ACS catalysis*, *2*(11), 2403-2408.

APPENDICES

Appendix A

A.1 Sample calculation for the mass ratio of Ni:CA for the synthesis of monometallic and bimetallic CNTs catalysts

Preparation for the impregnation process

Mass ratio of 10 wt.% Ni:

Mass of cordierite monolith = 0.3300 g

Mass of Ni = 10/100 x 0.3300 g
= 0.0330 g

Mass of Ni salt ($Ni(NO_3)_26H_2O$) = 0.0330 g Ni x (molar mass Ni salt/molar mass Ni)
= 0.0330 g Ni x (290.81 g/mol Ni salt/58.6934 g/mol Ni)
= 0.1635 g Ni salt ($Ni(NO_3)_26H_2O$)

Mole ratio Ni:CA = 1:1 (based on 10 wt.% Ni):

Mol of Ni salt ($Ni(NO_3)_26H_2O$) = mass of Ni salt / molar mass of Ni salt
= 0.1635 g / 290.81 g/mol
= 5.622×10^{-4} mol

Therefore, mass of citric acid based on 1:1 mole ratio is:

Mass of citric acid = mol of citric acid x molar mass citric acid
= 5.622×10^{-4} mol x 192.12 g/mol
= 0.1080 g citric acid

A.2 Sample of calculation for Taguchi method analysis

Parameters					*Carbon Yield (CNTs Growth)				Response
Run	A	B	C	D	Yield 1	Yield 2	Average Yield	Standard error	**S/N ratio
		mL/h	min	°C	%	%	%		dB
1	1:1	1	30	600	2.005	1.617	1.811	0.194	5.158

S/N value calculation:

$S/N_{larger-is-better}$ = - 10log $\left[\frac{1}{n}\sum_{i=1}^{r}\frac{1}{y_i^2}\right]$

$$= -10\log\left[\frac{1}{2}\times\left(\frac{1}{2.005^2}+\frac{1}{1.617^2}\right)\right] = -10\log(0.305)$$

$$= 5.158$$

Standard error calculation:

$$\sigma = \sqrt{\frac{\sum(x_i-\mu)^2}{N}}$$

σ= population standard deviation N= the size of the population
x_i= each value from the population μ= the population mean

$$\sigma = \sqrt{\frac{(2.005-1.811)^2+(1.617-1.811)^2}{2}} = 0.194$$

Ranking of parameters for a response calculation: (**Table 3.3**)

	Mass Ratio of Ni:CA	Injection Rate of Carbon	Reaction Time	Operating Temperature
Level	A	B	C	D
1	5.457	3.791	5.419	6.814
2	5.374	6.597	5.617	8.505
3	5.493	5.935	5.287	1.004
Delta	0.119	2.806	0.329	7.501
Rank	4	2	3	1

Average of S/N value for mass ratio Ni:CA;

Average S/N (1:1) $= (S/N_{1\text{-}1} + S/N_{1\text{-}2} + S/N_{1\text{-}3})/3$
$= (5.158 + 9.852 + 1.360)/3$
$= 5.457$

Average S/N (1:3) $= (S/N_{2\text{-}1} + S/N_{2\text{-}2} + S/N_{2\text{-}3})/3$
$= (-0.538 + 7.749 + 8.910)/3$
$= 5.374$

Average S/N (1:5) $= (S/N_{3\text{-}1} + S/N_{3\text{-}2} + S/N_{3\text{-}3})/3$
$= (6.753 + 2.189 + 7.536)/3$
$= 5.493$

Delta S/N value = The highest average S/N value – The lowest average S/N value

$= 3.5794 – 2.5674 = 1.012$

Then calculate the delta value for the injection rate of carbon, the reaction time and the operating temperature. The rank is arranged from the lowest value of delta to the highest.

Appendix B

B.1 Gas calibration curve

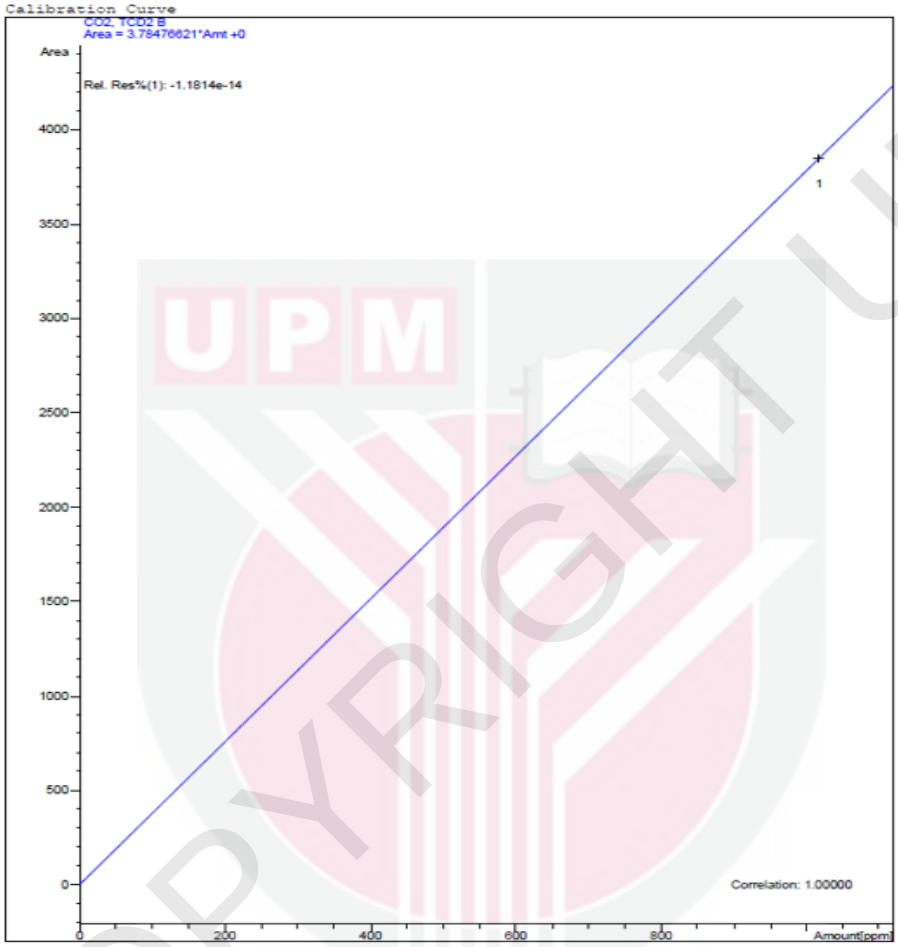

Figure B.1: Calibration curves for CO_2

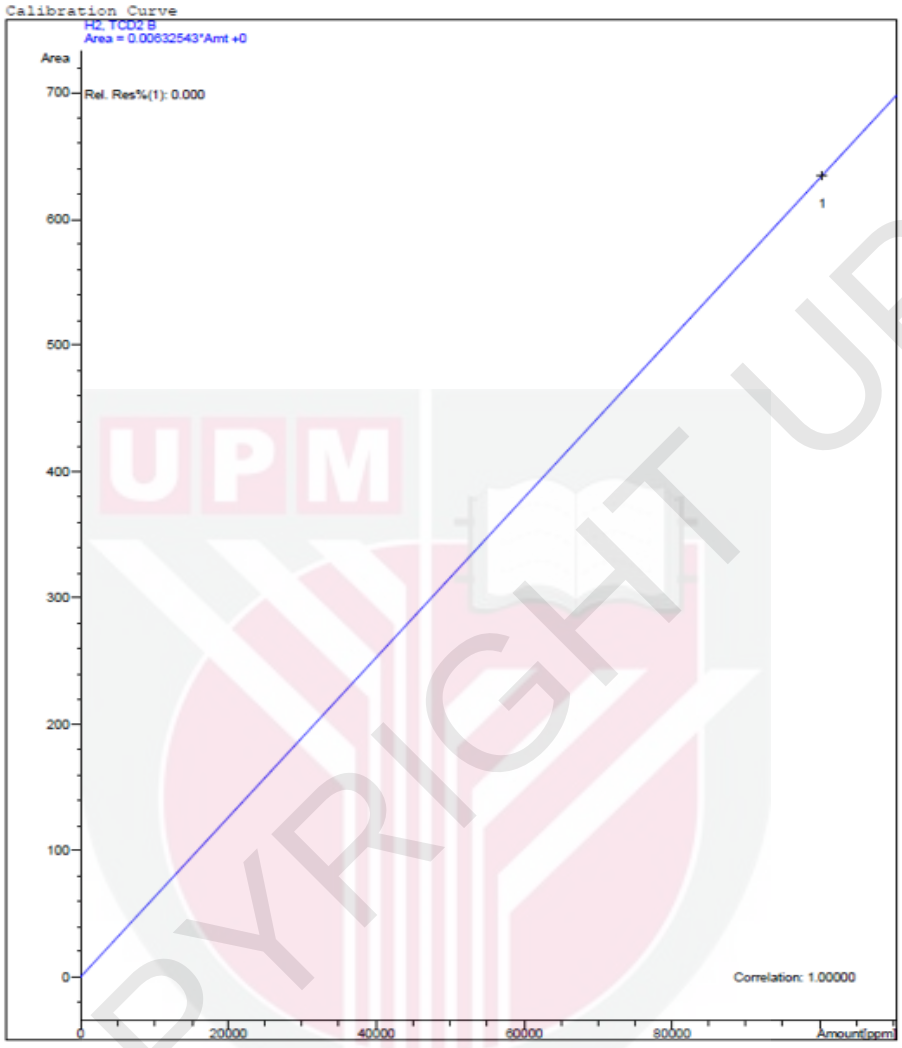

Figure B.2: Calibration curves for H_2

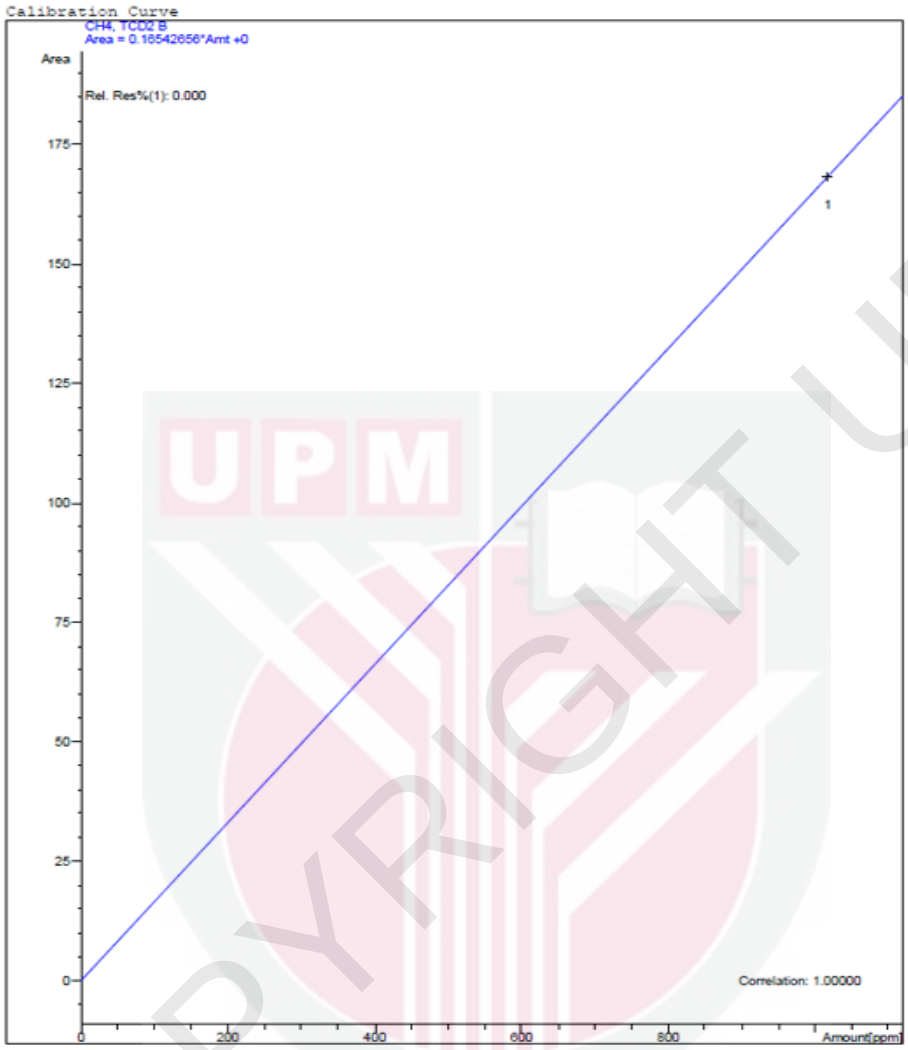

Figure B.3: Calibration curves for CH_4

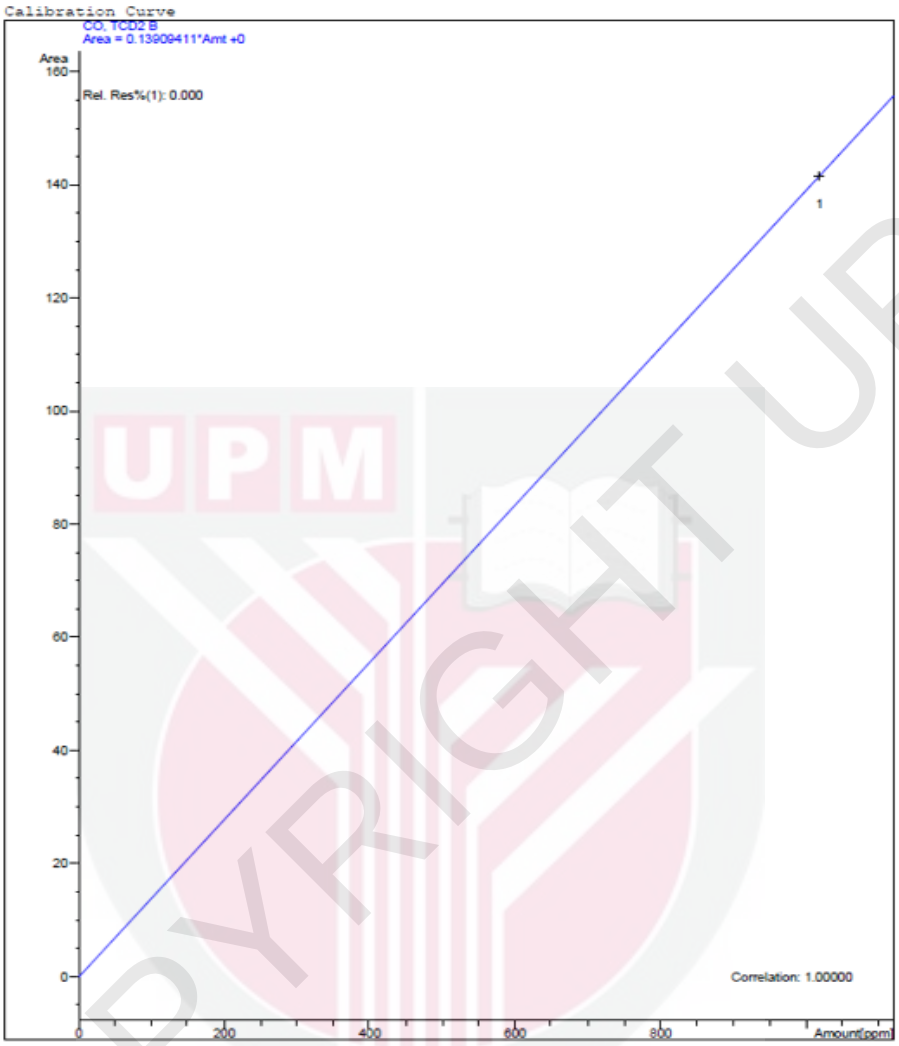

Figure B.4: Calibration curves for CO

B2: Information of gases from GC

The common equation for the measurement of CO_2 conversion, CH_4 selectivity and CO selectivity:

$$CO_2\ conversion \quad = \frac{[CO_2]_{in} - [CO_2]_{out}}{[CO_2]_{in}} \times 100$$

$$CH_4\ selectivity = \frac{[CH_4]_{out}}{[CO_2]_{in} - [CO_2]_{out}} \times 100$$

$$CO\ selectivity = \frac{[CO]_{out}}{[CO_2]_{in} - [CO_2]_{out}} \times 100$$

Condition of the reaction without catalyst:

Temperature = room temperature

Gas flowrate = 30 ml/min

Gas use as reactant = mixed gas 10% CO_2; 40% H_2, 50% N_2

Pressure = 1 atm

Gas	Area from GC peak	Calibration factor	Amount (ppm)	Amount (mol/L)
CO_2	354101.21	3.78476621	93559.6	2.1258
H_2	3683.58	0.00632543	582345.0	291.1725
CH_4	0	0.16542656	0	0
CO	0	0.13909411	0	0

Therefore:

The CO_2 conversion = (2.1258-1.3730) / 2.1258 x 100 = 35.41%

CH_4 selectivity = 3.3070 / (2.1258-1.3730) x 100 = 407.7 %

CO selectivity = 0.1484 / (2.1258-1.3730) x 100 = 19.7 %

Due to the initial amount of CO_2 lower than amount of CH_4 after the CO_2 methanation, the data analysis proceeds with the analysis using the equation from Vrijburg et al., 2019.

Condition of the reaction with catalyst:

Temperature = 400 °C

Gas flowrate = 30 ml/min

Gas use as reactant = mixed gas 10% CO_2; 40% H_2, 50% N_2

Pressure = 1 atm

Gas	Area from GC peak	Calibration factor	Amount (ppm)	Amount (mol/L)
CO_2	228704.02	3.78476621	60427.515	1.3730
H_2	1788.22	0.00632543	282702.57	140.2378
CH_4	8758.40	0.16542656	52944.32	3.3070
CO	578.17	0.13909411	4156.69	0.1484

Calculation:

1. Amount of gas CO_2 in ppm = 228704.02 / 3.78476621 = 60427.515 ppm

2. Amount of gas CO_2 in mol/L = 60427.515 / 1000 x 1/44.01 = 1.3730 mol/L

3. CO_2 conversion = (3.3070 + 0.1484)/(3.3070 + 0.1484+1.3730) x 100 = 71.56%

4. CH4 selectivity = 3.3070 / (3.3070 + 0.1484) x 100 = 95.7 %

5. CO selectivity = 0.1484 / (3.3070 + 0.1484) x 100 = 4.3 %

B3: Data sheet of catalyst stability studies

Time		CO_2		H_2		CH_4		CO		CO_2 conversion	CH_4 selectivity	CO selectivity
min	hrs	ppm	mol/L	ppm	mol/L	ppm	mol/L	ppm	mol/L			
17.00	0.28	61289.30	1.39	400666.18	198.75	43237.59	2.70	14612.20	0.52	69.82	83.81	16.19
34.00	0.57	61306.75	1.39	401175.98	199.01	45362.56	2.83	15340.04	0.55	70.82	83.80	16.20
51.00	0.85	61126.13	1.39	400523.74	198.68	46409.04	2.90	15631.30	0.56	71.34	83.86	16.14
68.00	1.13	61028.69	1.39	397644.08	197.26	47007.32	2.94	15787.58	0.56	71.62	83.89	16.11
85.00	1.42	61033.77	1.39	396273.64	196.58	47828.47	2.99	15823.83	0.56	71.92	84.10	15.90
102.00	1.70	60547.79	1.38	394777.05	195.83	48408.03	3.02	15753.68	0.56	72.27	84.32	15.68
119.00	1.98	60496.48	1.37	391448.32	194.18	49356.77	3.08	15745.58	0.56	72.62	84.58	15.42
136.00	2.27	60348.26	1.37	387388.16	192.17	50351.98	3.15	15602.03	0.56	72.97	84.95	15.05
153.00	2.55	60027.04	1.36	386998.53	191.97	51313.76	3.21	15450.09	0.55	73.36	85.32	14.68
170.00	2.83	59900.33	1.36	387387.00	192.17	52075.08	3.25	15364.69	0.55	73.63	85.57	14.43
187.00	3.12	59685.05	1.36	389201.27	193.07	52392.03	3.27	15352.25	0.55	73.80	85.65	14.35
204.00	3.40	59329.45	1.35	389046.79	192.99	52399.05	3.27	15407.82	0.55	73.93	85.61	14.39
221.00	3.68	58887.89	1.34	389935.45	193.43	52496.88	3.28	15384.43	0.55	74.10	85.65	14.35
238.00	3.97	58288.77	1.32	389341.85	193.14	52452.76	3.28	15406.92	0.55	74.29	85.62	14.38
255.00	4.25	57628.43	1.31	386877.39	191.91	52327.18	3.27	15315.73	0.55	74.45	85.67	14.33
272.00	4.53	57052.48	1.30	387230.80	192.09	52358.78	3.27	15291.66	0.55	74.64	85.69	14.31
289.00	4.82	56431.93	1.28	387915.95	192.43	52492.95	3.28	15261.45	0.54	74.89	85.75	14.25
306.00	5.10	55965.47	1.27	388780.56	192.86	52744.05	3.29	15297.28	0.55	75.13	85.78	14.22
323.00	5.38	55536.34	1.26	388238.44	192.59	52884.94	3.30	15334.53	0.55	75.32	85.78	14.22
340.00	5.67	55095.76	1.25	386875.00	191.91	53070.42	3.31	15358.82	0.55	75.53	85.81	14.19
357.00	5.95	54637.31	1.24	387907.76	192.43	53347.90	3.33	15326.08	0.55	75.76	85.90	14.10
374.00	6.23	54035.35	1.23	388086.88	192.51	53367.41	3.33	15271.63	0.55	75.96	85.94	14.06
391.00	6.52	53556.27	1.22	387132.48	192.04	53754.68	3.36	15133.01	0.54	76.21	86.14	13.86
408.00	6.80	53400.77	1.21	386587.94	191.77	54180.17	3.38	15131.71	0.54	76.38	86.23	13.77
425.00	7.08	52873.12	1.20	387184.32	192.07	54195.24	3.39	15063.26	0.54	76.55	86.29	13.71
442.00	7.37	52653.46	1.20	383625.32	190.30	54510.62	3.40	15024.07	0.54	76.71	86.39	13.61
459.00	7.65	52394.21	1.19	383567.73	190.27	55073.17	3.44	14875.79	0.53	76.93	86.63	13.37
476.00	7.93	52177.81	1.19	385120.44	191.04	55396.31	3.46	14811.32	0.53	77.09	86.74	13.26
493.00	8.22	51797.59	1.18	385026.70	191.00	55381.12	3.46	14803.79	0.53	77.21	86.75	13.25
510.00	8.50	51644.69	1.17	385863.15	191.41	55426.55	3.46	14821.49	0.53	77.28	86.74	13.26
527.00	8.78	51562.92	1.17	384464.35	190.72	55474.77	3.47	14875.65	0.53	77.33	86.71	13.29
544.00	9.07	51450.25	1.17	385182.57	191.07	55496.56	3.47	14892.17	0.53	77.37	86.70	13.30
12580.00	209.67	57179.55	1.30	406241.76	201.52	47179.21	2.95	17964.48	0.64	72.42	82.13	17.87
12597.00	209.95	57668.73	1.31	402974.26	199.90	47011.21	2.94	18047.99	0.64	72.21	82.01	17.99
12614.00	210.23	57921.37	1.32	404317.50	200.57	46860.65	2.93	17993.86	0.64	72.06	82.00	18.00
12631.00	210.52	57814.31	1.31	405458.89	201.13	46419.41	2.90	17985.58	0.64	72.94	81.87	18.13
12648.00	210.80	57823.84	1.31	401192.34	199.02	46553.98	2.91	17990.24	0.64	72.99	81.91	18.09
12580.00	209.67	57179.55	1.30	406241.76	201.52	47179.21	2.95	17964.48	0.64	73.42	82.13	17.87

Appendix C

C1: Types of mechanism steps

Mechanism steps	Reaction		Type of equation
Adsorption	$CO + S \underset{k_{-A}}{\overset{k_A}{\rightleftharpoons}} CO\text{-}S$	$rate\ of\ attachment = k_A P_{CO} C_S$ $rate\ of\ detachment = k_{-A} P_{CO-S}$ $r_{AD} = k_A(P_{CO}C_S - \frac{C_{CO-S}}{K_A})$ $\frac{r_{AD}}{k_A} = 0;\ C_{CO-S} = K_A C_S P_{CO}$ $C_t = C_S + C_{CO-S};\ C_s = C_t - C_{CO-S}$ $C_{CO-S} = \frac{K_A P_{CO} C_t}{1 + K_A P_{CO}}$	Langmuir isotherm
	$CO + 2S \underset{k_{-A}}{\overset{k_A}{\rightleftharpoons}} C\text{-}S + O\text{-}S$	$rate\ of\ attachment = k_A P_{CO} C_S^2$ $rate\ of\ detachment = k_{-A} C_{C-S} C_{O-S}$ $r_{AD} = k_A(P_{CO}C_S^2 - \frac{C_{C-S}C_{O-S}}{K_A})$ $\frac{r_{AD}}{k_A} = 0;\ k_A P_{CO} C_S^2 = \frac{C_{C-S}C_{O-S}}{K_A}$ $(K_A P_{CO})^{\frac{1}{2}} C_S = C_{O-S}$ $C_{C-S} = C_{O-S}$ $C_t = C_S + C_{CO-S}$ $C_s = C_t - C_{C-S} - C_{O-S}$ $C_s = C_t - 2C_{O-S}$ $C_{CO-S} = \frac{(K_A P_{CO})^{1/2} C_t}{1 + 2(K_A P_{CO})^{1/2}}$ multipying with $(P_{CO})^{1/2}$;	

		$\frac{P_{CO}{}^{1/2}}{C_{O-S}} = \frac{1}{C_t(K_A)^{1/2}} + \frac{2(P_{CO})^{1/2}}{C_t}$ $C_{CO-S} = \frac{K_A P_{CO} C_t}{1 + K_A P_A + K_B P_B}$	
Surface reaction		*Single site mechanism*	Langmuir-Hinshelwood kinetics
	A + S ⇌ A-S	$r_{AD} = k_A(P_A C_S - \frac{C_{A-S}}{K_A})$	
		Dual site mechanism	
	A -S ⇌ B-S	$r_S = k_S(C_{A-S} - \frac{C_{B-S}}{K_S})$	
	A -S + S ⇌ B-S + S	$r_S = k_S(C_{A-S}C_S - \frac{C_{B-S}C_S}{K_S})$	
	A-S + B-S ⇌ C-S + D-S	$r_S = k_S(C_{A-S}C_{B-S} - \frac{C_{C-S}C_{D-S}}{K_S})$	
		Third mechanism	Eley-Rideal mechanism
	A-S + B(g) ⇌ C-S + D(g)	$r_S = k_S(C_{A-S}P_B - \frac{C_{C-S}P_D}{K_S})$	
Desorption	C-S ⇌ C + S	$r_D = k_D(C_{C-S} - \frac{P_C C_S}{K_{DC}})$	

C.2 Sample of calculation

The activation energy of the CO_2 methanation reaction corresponds to Equation 5.13 in order to calculate the rate of the CO_2 methanation over 10 wt.% Ni and 1/10 wt.% Co/Ni-CNTs monolith catalysts at operating temperatures from 300 °C to 450 °C.

F = 22.3 mol/s

X = 0.3643

W = 0.312 g

$$r = \frac{\left(22.3\,\frac{mol}{s}\right)(0.3643)}{0.312\ g}$$

$$r = 26.0615\ \mathrm{mol/s.gcat}$$

The K_p value of 10 wt.% Ni and 1/10 wt.% Fe/Ni CNTs monolith catalysts at operating temperatures from 300 °C to 450 °C estimated using Equations 5.23 and 5.24. For instance calculation at T = 300 °C.

$$K_{p_{1\ Ni-CNTs\ monolith}} = \exp(\,2.2606 - \frac{156.34}{573.15}) = 7.2297$$

The values of r and Kp of each experimental data for P_{CO2}, P_{H2}, P_{CH4} and P_{H2O} and the k value, are determined using the Polymath program. According to Figure 5.4, the linear Arrhenius plot (lnK vs 1/T) gives the information of:

y = mx + C

y = -156.34x + 2.2606

$$\frac{-Ea}{R} = -156.34$$

R = 8.314 kJ/mol

$$\therefore E_a = -156.34\ \times 8.314\frac{J}{mol}.K$$

$$E_a = -1299.81\frac{J}{mol}.K = 1.3\frac{kJ}{mol}.K$$

The K_p value of 10 wt.% Ni and 1/10 wt.% Fe/Ni CNTs monolith catalysts at operating temperatures from 300 °C to 450 °C estimated using Equations 5.23 and 5.24. For instance, calculation at T = 300 °C.

$$K_{p_{1\ co/Ni-CNTs\ monolith}} = \exp(\ 10.068 - \frac{6125}{573.15}) = 0.5387$$

The values of r and K_p of each experimental data for P_{CO2}, P_{H2}, P_{CH4} and P_{H2O} and the k value, are determined using the Polymath program. According to Figure 5.4, the linear Arrhenius plot (lnK vs 1/T) gives the information of:

y = mx + C

y = -6125x + 10.068

$$\frac{-Ea}{R} = -6125$$

R = 8.314 kJ/mol

$$\therefore E_a = -6125\ \times 8.314 \frac{J}{mol}.K$$

$$E_a = -50923.25 \frac{J}{mol}.K = 50.923 \frac{kJ}{mol}.K$$

Model 3: Only reactant is adsorbed with dual site mechanism

POLYMATH Report
Nonlinear Regression (L-M)

Model: r = (k*PCO2*PH2)/(1+(KCO2*PCO2)+(KH2*PH2))^2

Variable	Initial guess	Value	95% confidence
k	1.	1.32807	0.781626
KCO2	1.	-0.2389217	0.0655298
KH2	1.	0.1135789	0.0623212

NOTE: Calculations exceeded the maximum number of iterations.

Nonlinear regression settings
Max # iterations = 64

Precision

R^2	0.9887997
R^2adj	0.9850663
Rmsd	0.1190039
Variance	0.191186

General

Sample size	9
Model vars	3
Indep vars	2
Iterations	64

Source data points and calculated data points

	PCO2	PH2	r	r calc	Delta r
1	27.75284834	9.972872342	17.82362277	18.16771	-0.3440906
2	25.8415564	10.48819676	22.86749146	22.69071	0.1767836
3	24.42950785	10.48651569	26.26645721	25.59805	0.6684119
4	23.40179336	10.3188033	27.71321577	27.43159	0.2816266
5	22.85771316	10.22538363	28.45728384	28.50716	-0.0498762
6	22.8189993	10.2822902	29.10755128	28.89175	0.2157967
7	23.44722875	10.59298555	28.34929251	28.55295	-0.203659
8	24.73366238	11.19096483	27.17577746	27.76948	-0.5936995
9	26.82977491	12.12436842	26.39046843	26.55889	-0.1684193

Model 1: All reactants and products are adsorbed with single-site mechanism.

POLYMATH Report
Nonlinear Regression (L-M)

Model: r = (k*PCO2*PH2)/(1+(KCO2*PCO2)+(KH2*PH2)+(KH2O*PH2O)+(KCH4*PCH4))

Variable	Initial guess	Value	95% confidence
k	1.	1.219137	0.5223666
KCO2	1.	0.6001336	0.0303998
KH2	1.	1.077851	0.4142902
KH2O	1.	-19.31722	0.9011184
KCH4	1.	-0.0327427	0.0277133

NOTE: Calculations exceeded the maximum number of iterations.

Nonlinear regression settings
Max # iterations = 64

Precision

R^2	0.982666
R^2adj	0.9727609
Rmsd	0.1570839
Variance	0.5076072

General

Sample size	12
Model vars	5
Indep vars	4
Iterations	64

Source data points and calculated data points

	PCO2	PH2	PH2O	PCH4	r	r calc	Delta r
1	30.42560576	0.503172709	1	1.046607296	41.53094849	41.44929	0.0816567
2	30.33006625	1.164663308	1	2.239551944	40.45574861	40.36549	0.0902603
3	29.95110455	2.321696294	1	4.754304473	41.33306553	42.29847	-0.965407
4	29.56137216	3.249555592	1	7.9164786	43.6362877	43.91333	-0.2770385
5	29.20227619	3.932251329	1	11.50540436	45.87418284	45.60499	0.269192
6	28.82248731	4.605794267	1	15.85480194	47.68475506	47.24789	0.4368689
7	28.50589294	5.197921221	1	20.31558318	48.99726694	48.46141	0.5358534
8	28.18053286	5.668575194	1	24.47445827	49.96237028	49.89233	0.0700432
9	28.04340221	6.111151386	1	28.42553809	50.64662181	50.11871	0.5279079
10	27.77315281	6.398059706	1	31.52124134	51.15768745	51.40258	-0.2448926
11	27.78458214	6.720162655	1	34.52223859	51.517849	50.92211	0.5957371
12	27.42697972	6.83140435	1	36.43946854	51.83300651	52.96471	-1.131702

LIST OF PUBLICATIONS

Journals

Qistina, O., Salmiaton, A., Choong, T. S., Taufiq-Yap, Y. H., & Izhar, S. (2020). Optimization of carbon nanotube-coated monolith by direct liquid injection chemical vapor deposition based on taguchi method. *Catalysts*, *10*(1), 67.

Omar Qistina, Ali Salmiaton, Thomas S.Y. Choong, Shamsul Izhar, and Yun Hin Taufiq-Yap. Characterization of carbon nanotubes coated monolith synthesized via chemical vapor deposition. Status: Accepted for publication. *Journal of Applied Science and Engineering*, Accepted to published.

Conferences and Proceedings

1. 31st Symposium of Malaysian Chemical Engineers (SOMChE), 2018
2. 2nd International Conference on Innovation in Chemical Engineering and Technology (ICICET), 2023